DISSERTATION

PUT FORWARD BY

THOMAS KIRCHNER

BORN IN GERA

REAL-TIME BLOOD OXYGENATION TOMOGRAPHY WITH MULTISPECTRAL PHOTOACOUSTICS

AN APPROACH TO INTERVENTIONAL IMAGING

REFEREES

PROF. DR. PETER BACHERT
PROF. DR. JOAO SECO

SUPERVISORS

PROF. DR. PETER BACHERT
PROF. DR. LENA MAIER-HEIN

ABSTRACT

Multispectral photoacoustics is an emerging biomedical imaging modality which combines the penetration depth and resolution of high-frequency medical ultrasonography with an optical absorption contrast. This enables tomographic imaging of blood oxygen saturation, a functional biomarker with wide applications. Already, photoacoustic imaging (PAI) is widely applied for small animal imaging in preclinical research. While PAI is a multiscale modality, its translation to clinical research and interventional use remains challenging. The objective of this thesis was to investigate the usefulness of multispectral PAI as a technique for interventional tomographic imaging of blood oxygenation. This thesis presents open challenges alongside research contributions to address them. These contributions are, (1) The design and implementation of an interventional PAI system, (2) Methods for real-time photoacoustic (PA) image processing and quantification of tissue absorption and blood oxygenation, and finally (3) the application of multispectral PAI to translational neurosurgical research – performing the first high spatiotemporal resolution tomography of spreading depolarization, and at the same time the first interventional PAI on any gyrencephalic (folded) brain. Such interventional imaging in neurology is one of many promising fields of application for PAI.

ZUSAMMENFASSUNG

Multispektrale Photoakustik ist eine aufstrebende biomedizinische Bildgebungsmodalität, die die Bildgebungstiefe und Auflösung von hochfrequentem medizinischen Ultraschall mit optischem Absorbtionskontrast verbindet. Diese Kombination ermöglicht eine tomographische Messung von Sauerstoffsättigung im Blut – ein funktioneller Biomarker mit einer Vielzahl von Anwendungen. Photoakustik wird bereits umfassend in der präklinischen Forschung verwendet und hat sich dort bewährt; doch obwohl Photoakustische Bildgebung prinzipiell weit skalierbar ist, bleiben Hürden bei der Translation der Modalität in die klinische Forschung und interventionelle Nutzung. Das Ziel dieser Arbeit war die Untersuchung der interventionellen Anwendbarkeit multispektraler photoakustischer Tomographie als Bildgebungsmethode zur Messung von Sauerstoffsättigung. In dieser Arbeit werden spezifische Herausforderungen aufgezeigen, und Forschungsbeiträge präsentiert um diese anzugehen. Diese Beiträge umfassen (1) das Realisieren eines entsprechenden interventionellen Photoakustiksystems, (2) Methoden zur Bildverarbeitung und Quantifizierung und (3) neuartige Anwendungen von Photoakustik in der translationalen neurochirurgischen Forschung. Letzteres umfasst die erstmalige räumlich und zeitlich hochauflösende Tomographie von Streudepolarisation, sowie gleichzeitig die erste interventionelle Anwendung photoakustischer Bildgebung im gyrencephalen (gefalteten) Gehirn. Solch interventionelle Bildgebung in der Neurologie ist nur eines der vielversprechenden Anwendungsfelder für die Photoakustik.

Ach wenn es doch ein Mittel gäbe
den Menschen durchsichtig zu machen wie eine Qualle

— Philander, Elektra. Stuttgart 1892

Für Jutta und Gitte.

ACKNOWLEDGMENTS

CONTENTS

LIST OF FIGURES

ACRONYMS

AR   acoustic resolution

BOLD blood oxygen level dependent

BVF   blood volume fraction

DAQ   data acquisition

fMRI functional magnetic resonance imaging

Hb   hemoglobin

HbO   oxygenated hemoglobin

LED   light emitting diode

MITK medical imaging interaction toolkit

MRI   magnetic resonance imaging

MSE   maximum safe exposure

MSOT multispectral optoacoustic tomography

NIR   near infrared

NIRS near infrared spectroscopy

OPO   optical parametric oscillator

OR   optical resolution

PA   photoacoustic

PACT photoacoustic computed tomography

PAI   photoacoustic imaging

PAM   photoacoustic microscopy

PAT   photoacoustic tomography

qPAI   quantitative photoacoustic imaging

RSOM   raster-scan optoacoustic mesoscopy

SD   spreading depolarization

SNR   signal-to-noise ratio

sO_2 blood oxygen saturation

US   ultrasound

UV   ultraviolet

VIS   visible

Part I

INTRODUCTION

1

MOTIVATION

Blood oxygenation or blood oxygen saturation (sO_2) is an important biomarker, sometimes even referred to as the fifth vital sign when it is estimated *in vivo* using pulse oximetry [1] or measured *ex vivo* from an arterial blood sample. Spatially resolved functional information on hemodynamic biomarkers like sO_2 can yield valuable information on diagnosis or staging of various diseases. Tumor hallmarks like angiogenesis or hypoxia in a tumor core can be imaged directly with an endogenous contrast. Limited perfusion of an organ due to an infarction could be monitored as well as reperfusion of an organ after surgery or transplantation. And most relevant for the work in this thesis, sO_2 can also be an indicator of tissue metabolism. Given the central role of sO_2 in both tissue function as well as its potential diagnostic and interventional use, imaging of sO_2 in depth could be a valuable tool for clinicians.

In principle, imaging a correlate to sO_2 in depth is possible with functional magnetic resonance imaging (fMRI) techniques [2] using a blood oxygen level dependent (BOLD) contrast [3]. Such techniques as well as intraoperative magnetic resonance imaging (MRI) applications continue to make progress [4]. However, fMRI remains much too cumbersome and expensive for many applications [5], with real-time interventional imaging being impossible.

With the abundance of possible applications of sO_2 imaging, the main objective of this thesis was to investigate if the principle of multispectral photoacoustic imaging (PAI) can be clinically translated as a technique for real-time interventional tomographic imaging of blood oxygenation in depth. More specifically PAI's application to brain imaging was investigated. This principle application is presented in the final two manuscripts of this thesis (C3 & J4). Functional brain imaging was described with photoacoustic (PA) tomography in small animals as early as 2003 [6]. Given this early success, one would imagine that the translation of photoacoustics to the clinic went smoothly during these last 20 years.

It did not.

Rather, it stalled due to a number of challenges that are outlined in Chapter 5. To fully grasp these challenges we first have to start with some principles of tissue optics and photoacoustics.

To begin with, photoacoustics is a technique which combines the contrast of optical absorption with the penetration depth of ultrasound (US). Multispectral PAI is a spectroscopic technique which is not lim-

ited to the imaging of hemodynamics – there is a range of endogenous chromophores and exogenous contrast agents which can be imaged with photoacoustics. It is used in different spectral regimes from ultraviolet (UV) light [7] to microwaves, but most translational photoacoustics research focuses on near infrared (NIR) light that can penetrate deeper into tissue through the so-called optical window. This and the optical properties of biological tissue in general is subject of Chapter 2.

Generally speaking, NIR light is diffused in tissue after less than a millimeter path and thereby loses the spatial information necessary to perform classical optical imaging. Monitoring macroscopic parameters remains possible with diffuse light as part of the diffused light reaches the structures of interest and is absorbed there. Classical optical monitoring methods, the most well-known of which are pulse oximetry and near infrared spectroscopy (NIRS), use the relative overall absorption over a range of wavelengths to estimate tissue parameters like sO_2 or blood volume fraction (BVF). In multispectral photoacoustics, tissue is illuminated with nanoseconds-short light pulses of different wavelengths to cause thermoelastic expansion in any absorber. The sudden local pressure rise, which is proportional to the absorbed energy, manifests in an acoustic response which can be detected on the tissue surface by US transducer arrays or hydrophones. This so-called photoacoustic effect is explained in Section 3.1.

Ultrasonic waves are able to transmit spatial information from absorber to surface, because they are scattered around two orders of magnitude less in tissue than light. Acoustic signals can be recorded as time series – due to the relatively small speed of sound – and then reconstructed into a PA image. In an ideal case, a PA image resulting from one light pulse is a spatial map of the locally absorbed energy. Section 3.3 outlines why this quantitative ideal image is mostly beyond reach. Section 3.2 illustrates the physical principle and feasibility of PAI.

The PAI principle can yield molecular functional imaging contrast deeper in tissue than any optical contrast modality. PAI has been applied to small animals, detecting a range of functional information and disease markers. By now, PAI covers a range of specific techniques ranging from microscopy resolutions and millimeter imaging depth to macroscopic applications which are comparable in depth penetration and resolution to high frequency clinical US. PAI techniques are often tailored to specific applications. Chapter 4 gives a brief overview over prominent state-of-the-art PAI techniques and PAI technology.

While the next three chapters give short introductions to the principles and techniques of PAI, Chapter 5 will address the challenges in clinical translation of PAI and Chapter 6 will outline the related contributions of this thesis.

2

OPTICAL PROPERTIES OF TISSUE AND WHY THEY ARE OF INTEREST

Optical methods are well suited to measure the abundance of a molecule as the energy of photons needed to excite molecules to higher vibrational and electronic energy levels are in the visible (VIS) to infrared range. Even slight changes in the structure of complex molecules change these levels.

Light-tissue interaction is photon-molecule interaction. In the VIS to NIR spectrum, photons interact with molecules in two principal ways – absorption and scattering.

At its core, the measurement of sO_2 is a measurement of the relative abundances A for two molecules, namely hemoglobin (Hb) and oxygenated hemoglobin (HbO).

Wanting to measure the relative abundance simplifies our problem immensely, as we only need to measure two local values which are proportional to these two abundances with the same proportionality coefficient. Blood oxygen saturation then is

$$sO_2 = \frac{A_{HbO}}{A_{HbO} + A_{Hb}}. \tag{1}$$

The abundance of a molecule can be obtained by probing the spectral distribution of absorption given by the absorption coefficient $\mu_a(\lambda)$ – λ being the wavelength of light. For material in this thesis both absorption coefficient μ_a and scattering coefficient μ_s are stated in units of cm^{-1}, the reciprocal value to the mean free path length of a photon until a corresponding event. With known absorption spectra $\mu_a(\lambda)$ for Hb and HbO and all other relevant absorbers in the probed location, molecular abundances can be obtained by linear spectral unmixing – solving a set of linear equations of the form

$$\mu_a^m(\lambda) = \langle [\mu_a^{HbO}(\lambda), \mu_a^{Hb}(\lambda), \dots]^T, [A_{HbO}, A_{Hb}, \dots]^T \rangle \tag{2}$$

with a measured spectrum $\mu_a^m(\lambda)$ for several wavelengths λ.

Other photon-molecule interactions like ionization or photochemical processes are only relevant for higher energies starting with ultraviolet light and for special molecules not found in human tissue e.g. chlorophyll. Scattering can be elastic scattering or inelastic Raman scattering. While photon energy remains unchanged in elastic scattering, inelastic
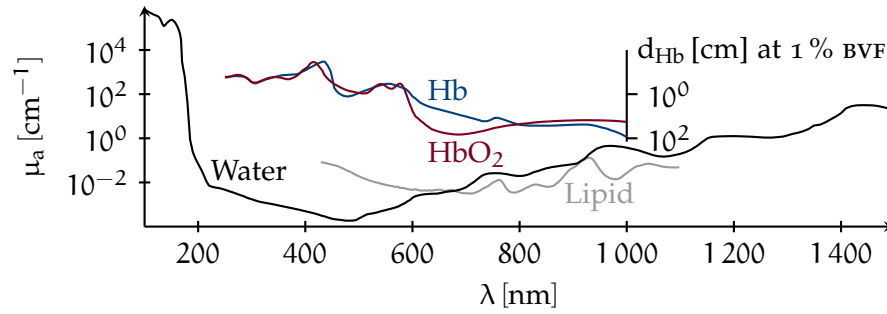
Figure 1: Absorption spectra $\mu_a(\lambda)$ of dominant bulk absorbers in tissue. The Hemoglobin (Hb) and oxygenated hemoglobin (HbO) spectra assume whole blood with a concentration of $150\,g\,l^{-1}$ – an average in humans. Additionally the photon mean free path in tissue d_{Hb} due to a realistic average blood volume fraction (BVF) of $1\,\%$ is plotted for hemoglobin. Absorbtion spectra from omlc.org/spectra compiled by Scott Prahl

scattering changes photon wavelength and is used for spectroscopic purposes. Inelastic scattering does not occur in the VIS to NIR range most relevant for macroscopic PAI.

ABSORPTION

Human tissue is composed of few bulk chromophores with relevant absorption spectra. In Figure 1 the absorption spectra $\mu_a(\lambda)$ of dominant chromophores [9] in human tissue are shown: Hb, HbO, water and lipid. In some organs additional chromophores are of high abundance, like melanin in the skin and bilirubin in the gallbladder. While there are further molecules with a high absorbance – e.g. proteins like cytochrome c [10] – these have a negligible abundance when compared to the dominant chromophores and have little to no contribution to tissue absorption. There are, however, chromophores that can play a role in some pathologies like e. g. β-carotene in neonatal jaundice.

From the bulk absorber spectra in Figure 1, three important facts are immediately noticeable: (1) whole blood dominates other optical absorber in tissue by one to four orders of magnitude, (2) Hb and HbO are distinguishable with high contrast for various sets of wavelengths, and (3) the mean free path length with a realistic blood volume fraction of $1\,\%$ is up to tens of centimeters in a window between $700\,nm$ and $900\,nm$. This range of wavelengths is commonly called the optical window of tissue. Within this window, endogenous chromophores like Hb and HbO can serve as contrast for functional imaging. Exogenous contrast agents with favorable absorption peaks can also be utilized.

But, soft! What light through yonder window breaks?
— Shakespeare
Romeo and Juliet

SCATTERING

Light scattering in the VIS to NIR spectral range is dominated by elastic scattering and is complicated by both the molecular composition and the layout of macro-molecules, like collagen fibres, or even organelles. A mean free path for an isotropic photon scattering event is about 100 µm and tissue is therefore considered a highly scattering medium or turbid medium. Optical scattering originates from photon interaction with biological structures which are comparable in size to the photon wavelengths and have a different refractive index as the surrounding material. Such scattering can be modelled very accurately by Mie theory which assumes scattering on isotropic spheres and simplifies to Rayleigh theory when scatterers get small against the scattered lights wavelength. A detailed introduction and derivation of Mie and Rayleigh theory for a single scatterer can be found in [11] (Chapter 2). Because bulk biological tissue is very heterogeneous on sub-micrometer scales, empiric values for tissue scattering are much more useful in practice.

Scattering severely limits classical ballistic optical imaging depth in tissue to about one millimeter depth. This is called the *diffusion limit* – which is formally defined as the transport mean free path, the inverse of which is the reduced scattering coefficient μ_s' with

$$\mu_s' = \mu_s \cdot (1 - g) \tag{3}$$

where g is the anisotropy of the scattering. In most tissue g takes values around 0.9 [12]. The diffusion limit is therefore the depth after which a photon can be assumed to perform a random walk.

Using PAI, scattering still attenuates the light that reaches the region of interest by scattering it out of the imaging volume, which limits optical fluence in very deep tissue.

We see the light but see not whence it comes.

— T. S. Eliot, The Rock.

PRINCIPLES OF PHOTOACOUSTIC IMAGING

We have seen that beyond the diffusion limit, photons are so highly scattered that precise spatial information is lost when classical optical imaging is performed by capturing the photons. However, the absorption of such photons in any absorber we may want to image still occurs at a specific location. This local absorption can give rise to the photoacoustic effect.

3.1 THE PHOTOACOUSTIC EFFECT

Photoacoustics is basically a light in - sound out approach. When Alexander Graham Bell first described this photoacoustic effect in 1880, he stated: *When a beam of sunlight falls upon this mass, the particles of lamp-black are heated and consequently expand.*[13] The photoacoustic effect occurs when light is absorbed in a short time interval and the resulting thermoelastic expansion causes a sudden pressure rise and corresponding acoustic wave.

There are three prerequisites for the PA effect to occur:

1. Absorption must actually heat the absorber – molecules must be excited by absorption and then undergo nonradiative relaxation, not fluorescence or phosphorescence. During the internal conversion from an excited vibrational state to a less excited state, photon energy is converted to kinetic energy. This only takes picoseconds and involves collisions with other molecules. In general, this process is dominant for VIS to NIR photons in tissue.

2. The illumination pulse duration τ_p must be small against the stress relaxation time τ_s. This ensures stress confinement within the structure of interest meaning stress propagation is negligible during the light pulse. The stress relaxation time is estimated by $\tau_s \approx d/v_s$, where v_s denotes the speed of sound and d the size structure of interest. For imaging, d can be used as an approximation for the achievable resolution.

3. τ_p must also be small against the thermal relaxation time τ_t to ensure thermal confinement of the temperature rise to the actual absorber only. The thermal relaxation time is estimated by $\tau_t \approx d^2/D$ where D is the thermal diffusivity in the structure of interest.

If these prerequisites are given, an ultrasonic wave emanates from a suddenly heated absorber. Ultrasonic waves have a two orders of magnitude lower scattering in tissue than light[14]. This makes it possible to reconstruct the origin of an ultrasonic wave and thereby image the absorber.

Using approximate soft tissue properties of $v_s = 1500\,\mathrm{ms}^{-1}$ and $D = 10^{-7}\,\mathrm{m}^2\mathrm{s}^{-1}$ while, for example, aiming to resolve structures of $d = 100\,\mu\mathrm{m}$ in size, we need light pulses shorter than a duration τ_p, with $\tau_p < \tau_s = 67\,\mathrm{ns}$ for stress confinement, and $\tau_p < \tau_t = 100\,\mathrm{ms}$ for thermal confinement. For this approximation, τ_s excludes all light sources except pulsed lasers or possibly very fast light emitting diodes (LEDs).

3.2 FEASIBILITY OF PHOTOACOUSTIC IMAGING IN TISSUE

To illustrate the practical feasibility of PA imaging in tissue, we start by assuming an illumination which causes a fluence rate $\Phi(\vec{x}, t)$, at location in the tissue $\vec{x}$, to a time t.

$\Phi(\vec{x}, t)$ is the energy passing through a unit area in a unit time. Absorbers distributed in our object absorb light giving us the absorbed power density $H(\vec{x}, t) = \mu_a(\vec{x}) \cdot \Phi(\vec{x}, t)$, as the loss in fluence rate by absorption. The absorption coefficient $\mu_a(\vec{x})$ in the tissue, is assumed to be time invariant.

The energy deposited in an absorbing structure by a single laser pulse is $H(\vec{x})$. The illumination causes the local irradiance or fluence $\phi(\vec{x})$ with[11]

$$H(\vec{x}) = \mu_a(\vec{x}) \int_0^\infty \Phi(\vec{x}, t)dt = \mu_a(\vec{x}) \cdot \phi(\vec{x}). \tag{4}$$

We will now estimate the initial pressure rise Δp caused by this absorbed energy in order to compare it to acoustic pressures in medical diagnostic US.

We will use the thermal expansion coefficient α and the compressibility β which are defined as[15]

$$\alpha = \frac{1}{V}\frac{\partial V}{\partial T} \qquad \Rightarrow \qquad \left(\frac{\partial V}{V}\right)_p = \alpha \cdot \delta T \tag{5}$$

$$\beta = -\frac{1}{V}\frac{\partial V}{\partial p} \qquad \Rightarrow \qquad -\left(\frac{\partial V}{V}\right)_T = \beta \cdot \partial p \tag{6}$$

where $(\delta V/V)_p$ is the relative increase in volume V of an absorber caused by the change in temperature T, and $(\delta V/V)_T$ is the relative decrease in volume adjacent to the absorber which is compressed by the expansion and not – assuming thermal confinement – heated itself. For a small timescale, we can assume linearity and obtain

$$\Delta p = \frac{\alpha}{\beta} \cdot \Delta T. \tag{7}$$

As we have an isentropic process due to our short time scale, our compressibility can be expressed in terms of the mass density ρ and the speed of sound v_s

$$\beta = \frac{1}{\rho \cdot v_s^2} \tag{8}$$

$$\Rightarrow \Delta p = \alpha \cdot \rho \cdot v_s^2 \cdot \Delta T. \tag{9}$$

ΔT is the rise in temperature in our absorber due to absorbed heat energy per unit volume $H(x)$. Using the specific heat capacity C_p defined as [15]

$$C_p \equiv \frac{1}{\rho}\left(\frac{\partial H}{\partial T}\right)_p \tag{10}$$

we reach an initial pressure rise only dependent on material constants and the added light energy per unit volume

$$\Delta p = \frac{\alpha \cdot v_s^2}{C_p} \cdot H. \tag{11}$$

At this point we define a commonly used dimensionless parameter – the Grüneisen parameter Γ

$$\Gamma = \frac{\alpha \cdot v_s^2}{C_p}. \tag{12}$$

The Grüneisen parameter for aqueous solutions Γ_a is heavily temperature dependent [16]. It follows this empirical relation [11]

$$\Gamma_a(T_{°C}) = 0.0043 + 0.0053\,°C^{-1} \cdot T_{°C}, \tag{13}$$

with $T_{°C}$ being the temperature in degree Celsius.

With that, the initial pressure rise is most often written as

$$\Delta p = \Gamma_a(T_{°C}) \cdot H \tag{14}$$

$$= \Gamma_a(T_{°C}) \cdot \mu_a \cdot \phi. \tag{15}$$

For a derivation of and solutions for the general PA equation see [11]

With this we can directly estimate our PA signal. Using equation 13 at body temperature we get $\Gamma_a(37\,°C) \approx 0.2$. As seen in Figure 1, whole blood has an absorption coefficient of $\mu_a \approx 4\,cm^{-1}$ at an isosbestic point of wavelength $800\,nm$ [12].

The maximum safe exposure (MSE) of skin to laser radiation is $33\,mJ\,cm^{-2}$ for that wavelength [17]. Such laser pulses can be delivered even for areas of some square centimeters by modern Q-switched lasers, and within a few nanoseconds. We can approximate the fluence in a shallow target – reduced by prior absorption and scattering – to be in the order of $\phi \approx 10\,mJ\,cm^{-2}$. These approximations result in initial pressure rise of $\Delta p \approx 10\,kPa$, which is in the order of magnitude of acoustic receive pressures for conventional US imaging. The signal

amplitude transmitted into the body in US imaging are $500\,\mathrm{kPa}$ to $5\,\mathrm{MPa}$ [14]. Assuming favorable changes in acoustic impedance and perpendicular incidence on boundaries the received signal is about $1\,\%$ of the input pressures. It should therefore be feasibility to detect PA signals with US imaging systems with comparable signal-to-noise ratio (SNR). The next section examines the reconstruction of these signals into images.

3.3 PHOTOACOUSTIC IMAGE RECONSTRUCTION AND QUANTIFICATION

A photoacoustic signal S caused by an initial pressure distribution $p_0(\vec{x})$ is chiefly dependent on fluence ϕ and absorption μ_a of the absorber, with

$$S \propto H \propto p_0 = \Gamma \cdot \phi \cdot \mu_a. \tag{16}$$

The origin of absorption was described in the last chapter. In multi-spectral photoacoustics we want to measure $\mu_a(\lambda)$. In our case this allows us to easily solve for the abundances of Hb and HbO.

In an ideal case, a multispectral stack would consist of n reconstructed images $S^{(1 \ldots n)}(\vec{x}, \lambda^{(1 \ldots n)})$ acquired with a set of laser pulses with wavelengths $\lambda^{(1 \ldots n)}$. These reconstructed images would then be a set of n spatial absorption maps $\mu_a^{(1 \ldots n)}(\vec{x}, \lambda^{(1 \ldots n)})$ in absolute units. For the purpose of sO_2 estimation a local proportionality of the reconstructed images to μ_a would suffice if

$$S^{(1 \ldots n)}(\vec{x}_0, \lambda^{(1 \ldots n)}) \propto \mu_a^{(1 \ldots n)}(\vec{x}_0, \lambda^{(1 \ldots n)}) \,\forall\, (\vec{x}_0 \text{ in } V) \tag{17}$$

where V is the imaged volume.

Like in every imaging technique this is complicated by various noise. There are two further complications to such an ideal case, which are ill-posed inverse problems that have lead to leaders in the field calling quantification of absorption the *'holy grail of photoacoustics'* and *'knowing the distribution of tissue optical properties'* an *'unattainable task'* [18]. These two complications are referred to as the optical inverse problem and the acoustic inverse problem. Figure 2 shows the PA forward process from the tissue properties to the recorded time series of PA signal. The optical and the acoustic parts of the forward processes are annotated. To solve these backwards is the corresponding inverse problem. In general, both of them are ill-posed [19]. The in-between thermalisation is dependent on the thermal properties of the tissue – as addressed in the previous section. Moving backwards through this diagram we will start with the time series $S_{(1 \ldots s)}(t)$ recorded with s sensors.

$\mu_a(\vec{x})$

$\phi(\vec{x})$

$p_0(\vec{x})$

$S_{(1 \ldots s)}(t)$
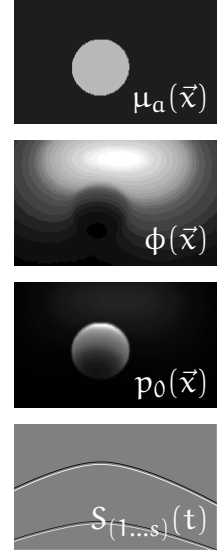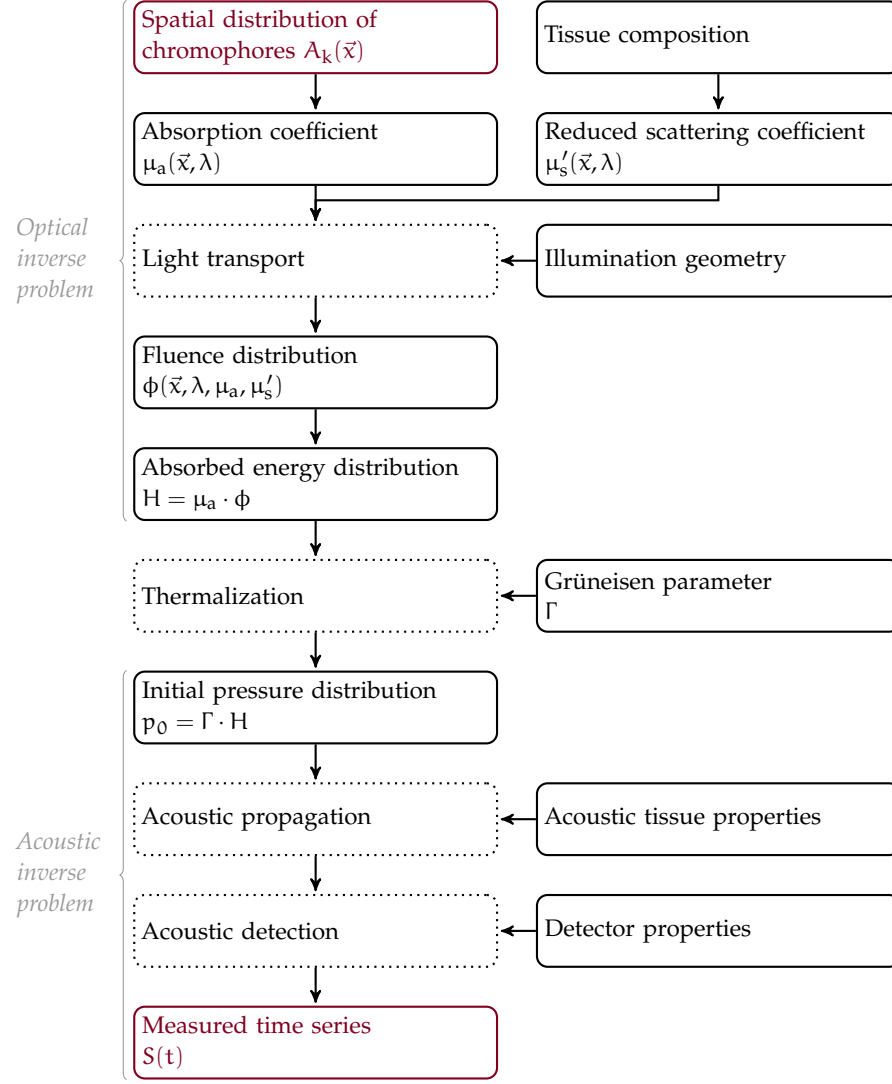
Figure 2: Chart of the photoacoustic (PA) forward problem, showing the processes – dotted – and the physical parameters that influence the measured signal $S(t)$ in photoacoustics. To estimate the chromophore distribution in tissue both the acoustic inverse problem and the optical inverse problem need to be addressed. The endpoints of the entirety of the problem are highlighted in red.

3.3.1   *Acoustic Inverse Problem*

The acoustic inverse problem is reconstructing $p_0(\vec{x})$ from the recorded signal time series $S_{(1\ldots s)}(t)$. This inverse problem can be split into a technical acoustic detection problem, and an unknown acoustic tissue property and the acoustic propagation problem. A PA signal's acoustic spectrum is very broad [20] reaching from the far ultrasonic to frequencies audible for humans.

The exact acoustic spectrum heavily depends on the macroscopic structures in the tissue – Figure 3 provides a representative illustration

… a sound that started in the far ultrasonic and finished somewhere in Rincewind's bowels.
— Terry Pratchett, The color of magic.

based on the PA response from the vasculature in a human palm [21]. It shows the expected $p_0(f)$ power spectrum and illustrates the acoustic attenuation for higher frequencies and depths. The acoustic signal that reaches the detector $p_D(f)$ is attenuated for higher frequencies. The acoustic response of transducers – i.e. piezoelectric sensors cause an additional loss of low frequency signal component missing which results in underrepresented larger structures. A typical clinical US transducer used for PAI has a sensor response $R(f)$ – a center frequency of 7.5 MHz with 80 % bandwidth. Such a response leads to a partial measurement of the PA signal $S(f)$. In addition, sensor sensitivity usually has an angular dependence on wave incidence [22].
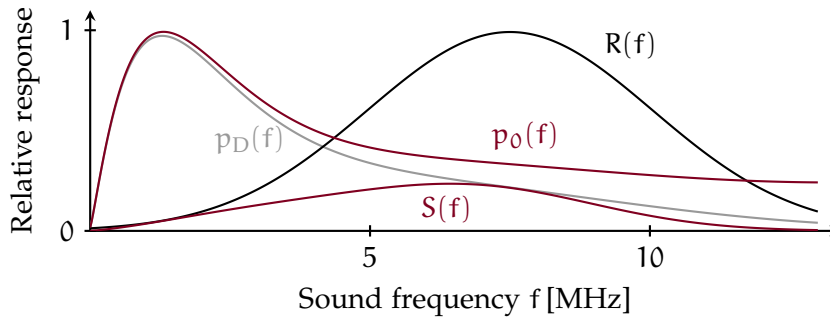
Figure 3: Illustration of the spectral attenuation. The initial PA $p_0(f)$ spectrum is broad, but acoustic attenuation of higher frequencies leaves $p_D(f)$ to reach to detector. $R(f)$ is the response of a typical medical ultrasound transducer centered at 7.5 MHz with 80 % bandwidth. These constraints leave a signal $S(f)$ to be detected by such a transducer.

In addition to these measurement sensitivity and sound attenuation issues, most PA measurement techniques have geometries with a limited view, meaning they can only recover partial data from the pressure waves originating from the imaged region. When reconstructing images from limited view data, artifacts will occur. However, there are both physical [23] and algorithmic [24] approaches to reduce these artifacts by either widening the view or adding prior knowledge about the imaged tissue to the problem. Acoustic propagation through media with highly inhomogeneous acoustic properties, i.e. soft tissue vs. bone, is difficult to account for without prior knowledge. State-of-the-art pressure sensors are miniaturized and data acquisition electronics can easily measure pressure data with 100 MHz temporal resolution, far above the necessary sampling rate according to the Shannon sampling theorem for band limited signals [25]. Technical issues therefore do not limit imaging resolution, as most PA imaging techniques are physically limited to acoustic resolutions above 50 µm.

The next chapter will introduce a wide range of PA imaging techniques, each of which allows for different reconstruction algorithms. Ranging from accurate but slow time reversal methods [20], over
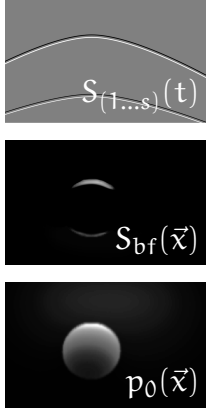
Radon transforms [26, 27] for small animal tomographs, to real-time beamforming and B-mode methods for linear transducer based systems.

$S_{(1\ldots s)}(t)$

$S_{bf}(\vec{x})$

$p_0(\vec{x})$

A beamformed image $S_{bf}(\vec{x})$ is illustrated in the margins, reconstructed from signals $S_{(1\ldots s)}(t)$ of s sensor elements. This illustrates the discrepancy between the initial pressure distribution $p_0(\vec{x})$ and even the ideal beamformed image reconstructed from the available data. In manuscript J1 of this thesis, an introduction to the most widely used reconstruction algorithm, delay and sum, is given before presenting an extension to it.

It has to be noted that no reconstruction algorithm so far actually solves the acoustic inverse problem completely. While time reversal on data without limited view and ideal spectral sensitivity can come close to a solution, it still breaks down for unknown and heterogeneous acoustic tissue properties. In practice, however, acoustic tissue properties are sufficiently homogeneous and artifacts sufficiently predictable that reconstructed images are at least interpretable. Importantly, for multispectral applications, local distortions of the reconstructed images relative to the real p_0 are not dependent on optical properties, but can be assumed to be similar for all illumination wavelengths.

3.3.2 *Optical Inverse Problem*

Quantification of absorption is the holy grail of photoacoustics.
— Alexander Oraevsky, public comment during SPIE Photonics West 2018

The optical inverse problem starts with assuming a known absorbed energy distribution H. To solve the *multispectral* inverse problem is to estimate the distribution of chromophores. For single wavelength illumination it consists of estimating the distribution of absorption coefficients. Since $H(\vec{x}, \lambda) = \mu_a(\vec{x}, \lambda) \cdot \phi(\vec{x}, \lambda)$, an estimation of $\mu_a(\vec{x})$ from $H(\vec{x})$ for a single wavelength is essentially the same task as the estimation of $\phi(\vec{x})$.

$\mu_a(\vec{x})$

$\phi(\vec{x})$

$H(\vec{x})$

As is illustrated in the margins, the fluence at position $\vec{x_0}$ is not only locally dependent on $\mu_a(x_0)$ and $\mu'_s(x_0)$ and the illumination I but depends on the entire context of optical tissue properties

$$\phi(\vec{x_0}, \lambda, \mu_a(\vec{x}, \lambda), \mu'_s(\vec{x}, \lambda), I). \tag{18}$$

In a simple one-dimensional example with no scattering and a pencil beam illumination, the fluence in a location within the beam is lower if there are absorbers in the light path. If we were to measure the absorbed energy distribution in this case, we could easily invert the problem using attenuation as described with Lambert-Beer's law.

$$\phi(x_0) = \phi(0) \cdot \exp(-\int_0^{x_0} \mu_a(x)dx) \tag{19}$$

But in a turbid three-dimensional case no such analytic inversion is possible. And while the illumination geometry is generally known, both $\mu'_s(\vec{x}, \lambda)$ and of course $\mu_a(\vec{x}, \lambda)$ are not. Even worse $\mu_a(\vec{x}, \lambda)$ must

be estimated at the same time as $\phi(\vec{x}, \lambda)$, which makes this inverse problem ill-posed.

In a multispectral case both absorption and scattering have a wavelength dependence which introduces wavelength dependent changes in fluence. These translate to the absorbed energy distribution $H(\vec{x}, \lambda)$ as so-called *spectral coloring* and distort measured spectral responses. This spectral coloring is exacerbated in deeper tissue.

The estimation of the fluence distribution, and thereby quantification of PAI has been the subject of intense study for more than a decade [28] and remains insufficiently solved for any translational application. In the last years, the field of quantitative photoacoustic imaging (qPAI) has started to make advances in the estimation of spectral coloring.

The fluence or spectral coloring estimation part of the optical inverse problem is key to solving it. The final step of estimating the spatial distribution of chromophores is straightforward, given good estimates for $\mu_a(\vec{x}, \lambda)$ for a number of wavelengths equal to or greater than the number of chromophores in the tissue. This spatial distribution of chromophores is usually obtained by linear spectral unmixing as described in Chapter 2.

4

PHOTOACOUSTIC IMAGING TECHNOLOGY AND TECHNIQUES

After introducing to PAI technology components, this chapter will give an overview over the existing variations of PAI techniques and present the prominent representatives of these techniques and their applications.

4.1 TECHNOLOGICAL REQUIREMENTS

Note that some specific implementations use 'optoacoustics' as a synonym to 'photoacoustics'.

The PA effect was first observed in 1880 and envisioned by Bell to be used for telecommunication – see Figure 4A. In the same year, Pierre and Jacques Curie first described the piezoelectric effect [29] – see Figure 4B – used today for transmitting and measuring US waves in medical US transducers.
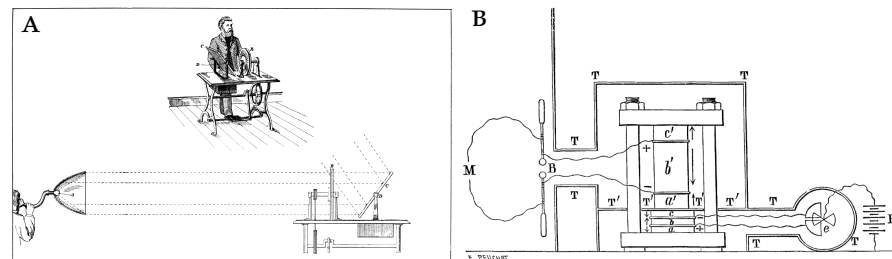
Figure 4: A — Bell's photophone setup with *a mode of interrupting a beam of sunlight* using a fast spinning shutter wheel to pulse sunlight.
B — Curie's device for measuring the converse piezoelectric effect with an isolated second direct piezoelectric crystal [30]. Figures reproduced from Bell [13] and Curie [31]

But sustained technological innovations in two fields – electronics and photonics – were necessary to apply these observations to biomedical imaging. Microelectronics are needed for the fast data acquisition (DAQ) necessary to measure pressure changes of megahertz frequency in tissue. In photoacoustics and in medical US imaging alike, computer technology development has, and continues to, enable not only DAQ but also fast image processing.

The innovation in photonics which provided high energy light pulses which allow stress confinement in small structures was Q-switched lasers [32]. Such lasers, often Nd:YAG lasers (sometimes frequency doubled) provide the illumination for most PAI systems. Often they pump a tunable optical parametric oscillator (OPO) to

produce a tunable range of VIS to NIR wavelengths. Laser diodes [33, 34] and also LEDs are increasingly considered for PA illumination [35, 36]. They can be driven to have rise times of less than 100 ns and are therefore somewhat stress confined but generally still suffer from low signal and therefore low penetration depth and slow acquisition speed. Diode based illumination may be a low cost perspective with wide utility in for photoacoustics, but Q-switched lasers yield simply superior illumination quality and quantity and are therefore currently the predominant light source for all PAI techniques.

4.2 MICROSCOPY, MESOSCOPY AND MACROSCOPY

The term photoacoustic microscopy (PAM) [37] referes to the highest resolution PA techniques where the sample is usually scanned with a single sensor in a raster scan. The sensor is most commonly either a single transducer or an optical sensor – a low power continuous wave probe laser with a Fabry-Perot interferometer. Transducer acoustic frequency responses are usually centered on high frequencies of 15 MHz to achieve higher resolutions. The illumination can follow the raster scan. Such an illumination is necessary for optical resolution (OR)-PAM. In OR-PAM the PA excitation laser is highly focused to illuminate a smaller area than could be resolved by acoustic waves. This technique usually uses VIS light – often around 532 nm because it is absorbed two orders of magnitude better in tissue than NIR light. Because of the focused illumination, OR-PAM is the only PAI technique that is limited in imaging depth by the diffusion limit. PAM is referred to as acoustic resolution (AR)-PAM when using an unfocused or weakly focused PA excitation. All non-microscopy PAI techniques are AR.

Non-microscopic PAI techniques are often classified as mesoscopy or macroscopy techniques. They have in common that their PA excitation illumination is wide-field and – depending on the detector geometry – an entire slice or volume can be imaged with a single pulse. Mesoscopy typically refers to imaging depths of up to five millimeters with imaging resolutions of less than 10 µm [9] while macroscopy techniques reach centimeters deep with lower resolution. This distinction is rather arbitrary but more consistent than the distinction between AR-PAM and PA mesoscopy. The exact detector geometries and properties vary widely, in the following PAI applications.

4.3 APPLICATIONS

PHOTOACOUSTIC MICROSCOPY   PAM is usually applied to small animals *in vivo* to image anatomical and functional contrast [37] and can be used to measure flow dynamics [38]. Zhang et al. [39] demonstrated AR-PAM *in vivo*, imaging angiogenesis, melanoma and sO_2 within single vessels in nude mice. In this work single A-line scan

was acquired in 2 μs and raster-scanning an area of 8 by 8 mm took 32 min.

Imaging a square-centimeter area can take tens of minutes but can be improved by faster lasers or more advanced acquisition schemes [40] and for small volumes or slices PAM can be real-time capable. A widely used iteration of PAM is raster-scan optoacoustic mesoscopy (RSOM), which is usually used to study nude mice for biomedical, often cancer research [41].

PHOTOACOUSTIC COMPUTED TOMOGRAPHY   Techniques which acquire PA signals with an array of unfocused transducers are sometimes referred to as photoacoustic computed tomography (PACT) or simply photoacoustic tomography (PAT). PACT systems computationally reconstruct slice or 3D volume data from k-space using a Radon transform or similar inverse algorithms [42]. Ring arrays surrounding the imaged subject are widely used for small animal imaging. Here the animal is submerged in water or deuterium and scanned slice by slice, moving it through the ring array. Using this technique, mice [43] and zebrafish [44] are most often scanned for various pre-clinical research applications [9] as well as pharmaceutical research [45]. Such small animal scanners can also be used to analyze *ex vivo* tissue samples i. e. breast tumors excised during a lumpectomy to check tumor margins [46].

First translational *in vivo* approaches of the technique also included breast imaging. Dedicated and often application-specific imaging systems are used for many *in vivo* human applications of PAI [47]. The detectors for PA mammography take the shape of submersion cups or plates. With such systems, imaging depths of up to 5 cm can be achieved [48], only using intrinsic contrast and usually with minutes of signal averaging. The US transducers used for these applications tend to have a broad bandwidth centered at low frequencies, e.g. 2.5 MHz. Angiography of the breast was performed using PACT mammography [49] and breast cancer screening [50] or related diagnosis is a promising field of application for PAI. Current state-of-the-art X-ray mammography can be insensitive to tumors in denser breasts and US imaging suffers from low sensitivity at an early stage lesions due to a acoustic contrast [42]. Imaging tumor markers other than density – like angiogenesis and sO_2 – can yield diagnostically relevant information [50]. One initial clinical study [51] found that regions with high PA contrast to background tended to indicate malignant lesions. The main advantage of these large fixed systems which often use patient beds with built in PACT scanner apertures is that a still patient allows for averaging of PA signals over durations like 30 min [52] – greatly increasing signal to noise.

HAND-HELD PHOTOACOUSTIC TOMOGRAPHY   Hand-held scanners usually loose the advantage of increasing SNR by prolonged averaging. They often rely on single laser shot acquisitions or averages over tens or hundreds of milliseconds of acquired signals – when using light sources that have kHz pulse repetition rates.

Smaller mesoscopic cup array probes are one very recent hand-held implementation of PAI. The technique uses broadband transducers and can be used for small animal[53] or superficial imaging[54] and provides volumetric data.

Hand-held PAT probes consisting of a line array or curved array of transducers started to be used in small animal imaging as well. They are easy to use as they can provide slice images in real time. Physicians are already very familiar with such images and handling of similar probes from medical US B-mode image streams. Using US imaging systems as a basis for a PAT system, can be seen as adding additional optical contrast to the morphological contrast of medical US. Providing an additional contrast to an existing modality may lower the translational hurdle for the clinical application of PAI.

Because they are compact, hand-held and familiar, such hybrid medical US and PAT systems are widely applicable to image several centimeters deep structures in real-time – which is why this scanner geometry was chosen in this thesis. Manuscript C1 will present such a system design. Kim et al.[55] present a similar, but less integrated system which they developed in parallel to the system in this thesis.

The Munich spin-off iThera even commercialized a PAT system for clinical research in 2016 which they refer to as clinical multispectral optoacoustic tomography (MSOT)[56]. The system is based on a smaller hand-held research version[57] and at first lacked hybrid US imaging. However, its specialized, concave sensor array does provide PA image quality superior to commercial US transducers. In the last years a number of clinical studies[58] started with this and other systems [59, 60], probing the clinical applicability of hand-held multispectral PAT. First results for promising applications include an application to breast cancer[61], and the staging of Crohn's disease with multispectral photoacoustics[62] – where remission and active disease could be distinguished by assessing the intestinal-wall photoacoustically.

*It is highly anticipated that further advancement
of this fast-growing imaging technology will revolutionize
both fundamental life sciences and clinical patient care.*

— L. V. Wang & S. Hu, Photoacoustic Tomography
In Vivo Imaging from Organelles to Organs. [63]

CHALLENGES IN CLINICAL TRANSLATION

In their 2012 review paper in Science [63] which with more than two thousand citations, has become the most cited work in the field, Lihong Wang and Song Hu emphasize the need for (1) faster and higher energy lasers to advance PA imaging into clinical use, and conclude their paper by writing:

> *Also needed are sophisticated algorithms to perfect* [(2)] *molecular quantification and to* [(3)] *suppress skull-induced artifacts. It is highly anticipated that further advancement of this fast-growing imaging technology will revolutionize both fundamental life sciences and clinical patient care.*

Put in the context of image reconstruction, these challenges can be pointedly rephrased to the research objectives (1) ensure a high SNR, (2) address the optical inverse problem (see Section 3.3.2), and (3) address the acoustic inverse problem (see Section 3.3.1).

These three technical challenges in photoacoustic imaging are addressed in this thesis to varying degrees. An additional translational challenge to the application of any new imaging modality in a clinical or even surgical context is its integration into the workflow. This thesis approaches this issue by integrating photoacoustics into clinical ultrasonic probes, retaining the already familiar use of ultrasound imaging in clinical workflows.

When moving from mice to men, the necessary penetration depth of both light and sound increases by an order of magnitude. On the acoustic side of this, the transition is mostly straight-forward: using lower frequency ultrasonic sensing, acoustic attenuation decreases almost linearly, and a higher acoustic imaging depth is paid for by proportionally lower resolution. An exception is the acoustic penetration of bone and the corresponding acoustic scattering and reflection artifacts. This issue is yet to be addressed conclusively and is for the most part avoided whenever possible. On the optical side, light attenuation does not impose a hard limit but still causes an exponential drop in fluence with depth. Higher imaging depth will also intensify spectral coloring in non-trivial ways.

Clinical translation of photoacoustics therefore only exacerbates the three main technical challenges for photoacoustics.

6

CONTRIBUTIONS

The contributions towards this thesis' objective are structured into three fields.

1. *Imaging System* design and implementation for real-time applications. This thesis presents a well-integrated hybrid multispectral PAI and US imaging system suitable for interventional use. To ensure high SNR the highest energy fast-tunable mobile laser system available was integrated in the system.

2. *Signal Processing* includes algorithmic work consisting of: a real-time image reconstruction approach addressing the acoustic inverse problem to some extend, quantification approaches to the optical inverse problem and an approach to motion compensation utilizing the morphological US information provided by our system.

3. *Application* to neurosurgical translational research: Where PA tomography is performed interventionally on a gyrencephalic brain for the first time – providing high spatiotemporal scans of brain hemodynamics during spreading depolarization (SD).

The seven manuscripts which follow in Part II – the main body of this thesis – will present studies and new methods related to these contributions. They are structured according to their primary field of contribution.

Part II

MANUSCRIPTS

From the seven manuscripts included in the main body of this work three are published in peer-reviewed journals (J1–J3) and one is a pre-print under review in journal (J4). I am the first author on J1, J3 and J4; the work of J1 was performed in equal contribution with my then-master-student Janek Gröhl, with whom I continued to collaborate as a doctoral student, co-authoring J2 amongst other work.
I included three non-peer-reviewed manuscripts (C1–C3) in this cumulative thesis as they clarify methods and constitute development steps necessary for J4. The contents of the non-peer-reviewed manuscripts were presented at the Photons Plus Ultrasound conference within SPIE Photonics West 2018 and 2019.
My specific contributions are detailed before each manuscript. I directly supervised two Bachelor theses (Niklas Holzwarth and Kris Dreher) and in addition to supervising the master thesis of Janek Gröhl, I co-supervised the master thesis of Dominik Waibel. I was almost continuously supported by a graduate assistant – Franz Sattler – who substantially contributed to computer code critical to most of my work.

As senior author of all the manuscripts and a supervisor of this thesis Lena Maier-Hein was continuously involved in discussions of methods, experiments and analysis, as well as the writing process for all the manuscripts. She also acquired the funding for the project.

Additional publications more peripheral to my thesis are listed in the complete List of publications.

IMAGING SYSTEM

C1

AN OPEN-SOURCE SOFTWARE PLATFORM FOR TRANSLATIONAL PHOTOACOUSTIC RESEARCH AND ITS APPLICATION TO MOTION-CORRECTED BLOOD OXYGENATION ESTIMATION

This manuscript gives an introduction to the imaging system and real-time software designed and implemented for this thesis. It also presents a first proof-of-concept application on the carotid artery and a simple-yet-effective motion-correction approach.

Own contribution

The initial manuscript was drafted by me and edited and revised by all authors.

I contributed the system design – acquiring a suitable commercial US research system from Fraunhofer IBMT and a commercial laser system suitable for multispectral photoacoustics. I integrated the two systems into one real-time imaging platform primarily extending the medical imaging interaction toolkit (MITK). I was greatly assisted in the extensive coding work by Franz Sattler and generally supported by the MITK development community. I conceived of and implemented the motion-correction approach.

The experiments were conceived of and designed in discussion with Janek Gröhl, and performed by me, Janek Gröhl, Moritz Bischoff und Angelika Laha. I performed the post-processing and analysis for the data from the experiments.

An open-source software platform for translational photoacoustic research and its application to motion-corrected blood oxygenation estimation

Thomas Kirchner [a,b], Janek Gröhl [a,c], Franz Sattler [a,b], Moritz S. Bischoff [d], Angelika Laha [a], Marco Nolden [e,c], and Lena Maier-Hein [a,c]

[a] Division of Computer Assisted Medical Interventions (CAMI), German Cancer Research Center (DKFZ), Heidelberg, Germany
[b] Faculty of Physics and Astronomy, Heidelberg University, Germany
[c] Medical Faculty, Heidelberg University, Germany
[d] Department of Vascular and Endovascular Surgery, Heidelberg University Hospital, Heidelberg, Germany
[e] Division of Medical Image Computing (MIC), German Cancer Research Center (DKFZ), Heidelberg, Germany

ABSTRACT

Photoacoustic (PA) imaging systems based on clinical linear ultrasound arrays have become increasingly popular in translational PA research. Such systems can be more easily integrated in a clinical workflow due to the simultaneous access to ultrasonic imaging and their familiarity of use to clinicians. In contrast to more complex setups, hand held linear probes can be applied to a large variety of clinical use cases. However, most translational work with such scanners is based on proprietary development and as such not accessible to the community. In this contribution, we present a custom-built, hybrid, multispectral, real-time photoacoustic and ultrasonic imaging system with a linear array probe that is controlled by software developed within the Medical Imaging Interaction Toolkit (MITK) a highly customizable and extendable open-source software platform. Our software offers direct control of both the laser and the ultrasonic system and may serve as a starting point for various translational research projects and developments. To demonstrate the applicability of the platform, we used it to implement a new method for blood oxygenation estimation in the presence of non-rigid inter-frame motion caused by pulsing arteries. Initial results from experiments with healthy human volunteers demonstrate the suitability of the method with the sample clinical application of imaging the common carotid artery as well as peripheral extremity vessels.

Keywords: Photoacoustics, Ultrasound, Real-time, Blood oxygenation, Open-source, Translational, MSOT, Motion correction

1. INTRODUCTION

Estimating blood oxygenation (sO_2) or similar functional parameters deep inside tissue is one of the key use cases for multispectral photoacoustic (PA) imaging.[1] A reliable and fast measurement of sO_2 can have many applications and is one of the main arguments for translation of PA imaging into the clinic.[2,3] PA imaging systems that are based on clinical ultrasound systems with hand held linear probes[4] are relatively easily integrated in a clinical workflow due to the simultaneous access to ultrasonic imaging and the familiarity of use to clinicians. In contrast to other PA imaging setups, hand held linear probes can be applied to a large variety of clinical use cases. However, most translational work with such scanners is based on proprietary software development and as such not accessible to the community.

Please address your correspondence to Thomas Kirchner, e-mail: t.kirchner@dkfz-heidelberg.de

To address this bottleneck, we present a real-time multispectral hybrid PA and ultrasonic (US) (PAUS) imaging system running on the open-source platform Medical Imaging Interaction Toolkit (MITK).[5] The functionality of the software framework is demonstrated by implementing a new method for sO_2 estimation in the presence of motion. The latter relies on the computer vision method *optical flow*[6] to co-register a sequence of PA images using brightness patterns in corresponding US images and was specifically designed to mitigate non-rigid inter-frame motion caused by pulsing arteries. The performance of the platform including the presented software modules is demonstrated by means of motion-corrected blood oxygenation estimation in the carotid artery and accompanying vein based on data acquired with the presented system.

2. PAUS IMAGING PLATFORM

In this section, we present the hardware setup and the open-source software components developed for our PAUS imaging platform.
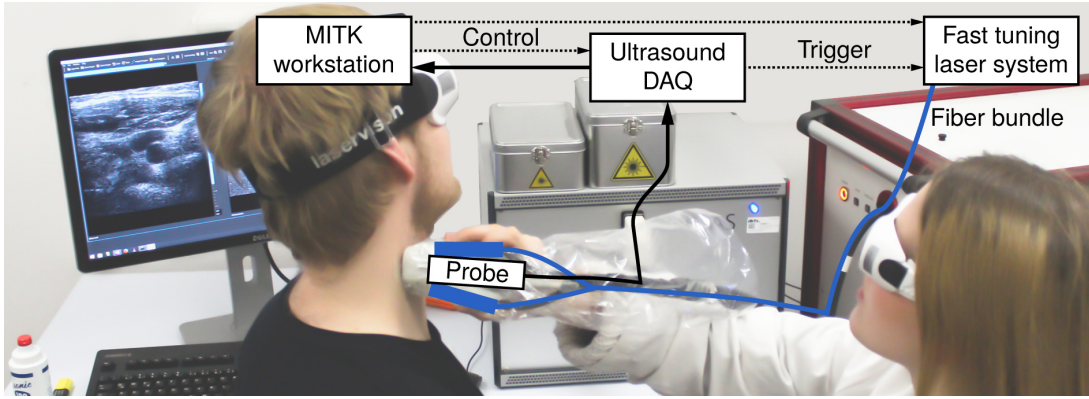
Figure 1. Hardware setup in use. The custom build photoacoustic-ultrasonic (PAUS) imaging system consists of a fast tuning optical parametric oscillator (OPO) laser triggered by the data acquisition (DAQ) system, which uses a linear transducer. The workstation runs the Medical Imaging Interaction Toolkit (MITK) for control of laser and DAQ as well as real-time processing and visualization of the photoacoustic (PA) and ultrasonic (US) data streams.

2.1 Hardware setup

The hardware setup is shown schematically in Fig. 1. Data acquisition is performed using our DiPhAS US system (Fraunhofer IBMT, St. Ingbert, Germany) and a 128-element linear US transducer operating on a center frequency of 7.5 MHz (L7-Xtech, Vermon, Tours, France). The light from a fast tuning OPO laser (Phocus Mobile, Opotek, Carlsbad, USA) is delivered via a custom fiber bundle to the probe and into the tissue or phantom. The pulse energy of up to 40 mJ at a pulse repetition rate of 20 Hz is delivered over a surface of $2\,cm^2$, below the maximum permissible exposure safety limit[7] to avoid tissue damage. The actual energy output of each individual laser pulse can be measured with an integrated pulse energy sensor. For all mentioned hardware components application programming interfaces (APIs) are provided by the vendors. Additionally, several software components were specifically developed by us for hardware communication, as detailed below.

2.2 MITK Photoacoustics software components

The real-time PAUS imaging software has been developed as part of MITK, a free open-source software platform for interactive medical image processing software. MITK has a modular architecture, where *Plugins* contain the user interface and have dependencies to *Modules* which comprise the application logic and domain specific functionality. Each plugin provides graphical user interfaces (GUIs) for specialized controls in so-called *Views* which are callable from the MITK workbench – the interactive user application for research within MITK. The structure of MITK therefore implements a clear separation of the application layer, i.e. the direct user interaction, and lower layers such as hardware control.

External libraries like the Insight Toolkit (ITK)[8] and the Visualization Toolkit (VTK)[9] are integral dependencies of MITK. For further specialized use cases other libraries are provided through their implementations in MITK. Examples for external libraries in use are the OpenCV[10] library for motion estimation, Eigen[11] for spectral unmixing and OpenCL[12] for implementations of algorithms on GPU for faster execution. Data can be exchanged in real-time with systems not running via MITK or even on different PCs using MITKs implementation of OpenIGTLink.[13] Offline processing of recorded data can be performed with the MITK PA image processing plugin, as was the case for the beamforming in the experiments.[14]* Fig. 2 shows the main software components we implemented or extended for PAUS imaging. The following paragraphs describe those components in detail.
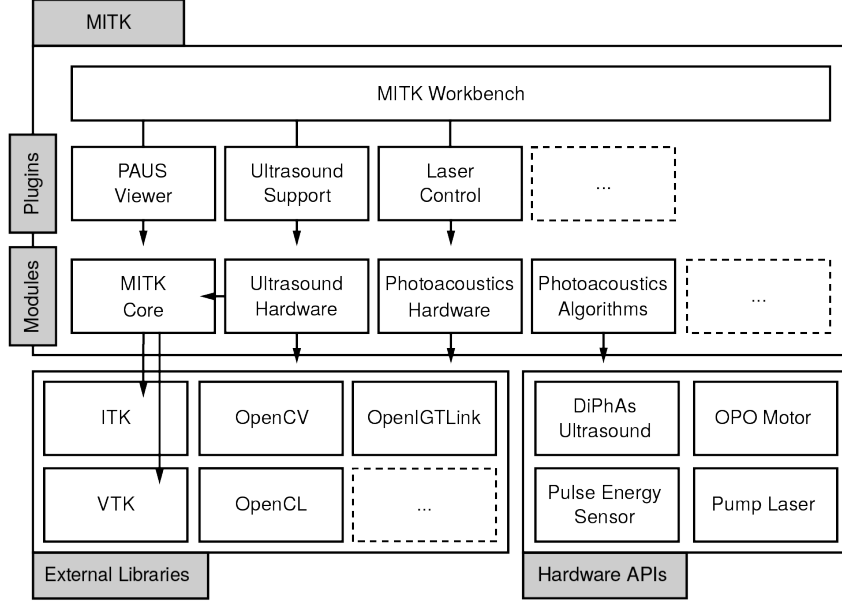
Figure 2. Software components of the Medical Imaging Interaction Toolkit (MITK). The MITK Workbench serves as an extendable user interface comprised of functionality provided by various *Plugins*. Those Plugins also connect the user interface with functional units provided in *Modules*. Those Modules can have dependencies on and draw their functionality from external libraries. The Modules also serve as an interface to external hardware and their application programming interface (API)s.

Hardware layer   The hardware layer abstracts the control of the hardware used, i.e. the DiPhAS US system and the OPO laser. Hardware control has been implemented in the classes corresponding to the *USHardwareDiPhAs* sub-module of the *Ultrasound Hardware* module and the *PhotoacousticsHardware* modules. The *Ultrasound Hardware* module and its sub-modules rely heavily on the existing generalized architecture of MITK for US devices.[15] Communication with the DiPhAs API and therefore control over the transducer and its output is implemented in the *USHardwareDiPhAs* sub-module. The transducer itself is represented as a generalized US device by a subclass of the abstract *Device* class where all hardware control is centralized. The *Device* class, as well as further classes, which are accessible through the *Device* class, such as an *ImageSource* subclass that handles image acquisition, handle communication, storage and adjustment of necessary parameters for image acquisition, e.g. time gain compensation or transducer voltage, as well as the setup of the interleaved PAUS acquisition sequence. This simple hierarchical approach allows to use a single unifying extendable interface to access multiple US devices, which can be managed in parallel.

---

*using commit `https://phabricator.mitk.org/rMITK9ce68418f58b`

The *ImageSource* class acquires image data from the US system through the external vendor API through a callback method. Both the raw image data, as well as images beamformed by the DiPhAS system are passed through the callback, allowing both for fast display of the beamformed US and PA images, as well as for later image processing of the raw data. The passed image data is continuously put into a buffer which is accessed by the processing layer for later display, while the raw data can be saved directly onto a hard drive for later use.

The *PhotoacousticsHardware* module handles communication with the laser system to control the pump laser and tune the OPO. Specifically, the pump laser is controlled via serial port using MITKs *SerialCommunication* class, while the OPO can be controlled using its API. The module also implements a method to allow the *USHardwareDiPhAs* sub-module to read out the data from an internal pyroelectrical sensor in the laser system which acquires the current laser pulse energy. This data can be matched to the acquired PA images and used to perform corrections for laser energy fluctuations.

Processing layer   Basic Processing is performed in the *ImageSource* class before the acquired images are displayed. Whenever the plugin within the application layer requests a new image, a method within the *ImageSource* class is called through the *Device* class, which grabs the most recent image within the buffer that contains the beamformed images. Various filters can be applied to the image depending on the settings, such as a resampling filter (i.e. vertically rescaling the image), a B-Mode filter, or basic fluence corrections for pre-defined illumination geometries. Afterwards, the processed image is passed to the application layer.

Application layer   Data acquisition from the DiPhAS setup is performed based on user settings specified in the MITK US Support plugin[15] which has been extended to work with our custom DAQ†. The US Support plugin communicates with the USHardwareDiPhAS sub-module through an instance of its *Device* subclass, which it accesses through MITK's micro service functionality; through micro services, a module is able to register as a specific service, which can be then requested by other modules or plugins. Various PA specific image acquisition settings are available within the US Support plugin. These preferences are handed over to the *USHardwareDiPhAS* sub-module which is responsible for communication with the hardware API. The plugin also passes image data acquired through the device's *ImageSource* class to the *PAUSViewer* plugin. The *PAUSViewer* plugin has been implemented specifically for the use case of PAUS imaging and provides a view that presents corresponding images of both modalities side by side in real-time, with options to set specific level windows and various colormaps. To set the triggers for the Laser system, define fast tuning wavelength sequences, as well as to control the status of the laser, the *Laser Control* Plugin was implemented. The plugin serves as a user interface for the *PhotoacousticsHardware* module. The application layer in general is highly customizable and extendable depending on the use case or specific problem at hand.

3. CLINICAL SAMPLE APPLICATION

An example for a possible clinical application of PA imaging is the visualization of transmural inflammatory processes such as large cell arteritis, i.e. giant cell arteritis,[16] where PA imaging could be used in the diagnostic workup. As an initial step towards this use-case we image the carotid artery of a healthy human volunteer and estimate blood oxygenation as a qualitative validation. The long term goal for PA imaging of the carotid artery is to investigate if and how multispectral PA imaging can be used in the diagnosis of inflammatory processes in arteries. In addition, PA imaging may be useful in the evaluation of plaque morphology in carotid artery stenosis or in the planning phase of surgeries for head and neck cancers invading the carotid artery.

One of the main issues during the sequential measurement of multiple multispectral PA images of the carotid artery is inter-frame motion, which leads to invalid results due to intense motion artifacts. If the motion is periodic, these artifacts might be somewhat mitigated by frame averaging[17] and there exist approaches in PA computed tomography which assume rigid motion[18] or perform gated image acquisition[19] to minimize motion artifacts. But frame averaging in moving structures will always improve imaging results at the expense of resolution and imaging time as well as temporal resolution. Also, the motion of the carotid artery and the

---

†The data acquisition was performed with commit `https://phabricator.mitk.org/rMITK2d2ebd4f22fa`

surrounding tissue is not rigid. Furthermore, gating is impractical due to the need for additional equipment and the about 20-fold decrease in imaging frame rate to approximately 1 Hz which in turn leads to increased motion artifacts due to the movement of patient and physician especially when using free hand probes. The following section shows how we aim to demonstrate the applicability of our framework to *in vivo* blood oxygenation estimation.

3.1 Motion-compensated blood oxygenation estimation

In the following we present the methods used for our platform demonstration experiments: (1) The spectral unmixing method for sO_2 estimation and (2) our new inter-frame motion correction approach. Both methods are implemented as python extensions with minimal overhead and can be used via the python interface offered by MITK.[‡]

3.1.1 Blood oxygenation estimation with spectral unmixing

sO_2 estimation with spectral unmixing from PA images requires a number of acquired wavelengths of at least the number of unmixed chromophores (two). Using more wavelengths will make the estimation more robust.[20] We record a *sequence* of raw PA data at five wavelengths in the near infrared. Based on Luke et al.[21] and considering the power spectrum of our laser source we skew our wavelength sequence from an equidistant spacing towards wavelengths where the differences between absorption of oxygenated and deoxygenated hemoglobin are most significant. The acquisition wavelength sequence is measured by a spectrometer (HR2000+, Ocean Optics, Dunedin, USA) to account for errors in OPO calibration.

Spectral unmixing is performed using a non negative constrained linear least squares solver[22][§] on the sets of five B-Mode images. The unmixing results for oxygenated (HbO_2) and deoxygenated hemoglobin (Hb) are used to calculate blood oxygenation and total hemoglobin (THb):

$$sO_2 = \frac{HbO_2}{Hb + HbO_2}, \qquad THb = Hb + HbO_2. \tag{1}$$

sO_2 is visualized by masking the results for low values of THb.

3.1.2 PAUS inter-frame motion correction

We propose a method which uses US images to compensate for intra-sequence motion of the PA images. Our PAUS imaging system acquires interleaved US images with minimal delay after each PA image. We estimate the *optical flow*[6] of each US image in a sequence with respect to the first US image in that sequence. We then use these estimated optical flows to warp their corresponding PA images. As "Optical flow is the distribution of apparent velocities of movement of brightness patterns in an image",[23] it is necessary to estimate the optical flow in the US images instead of the PA images, as brightness and the patterns having that brightness vary strongly in a multispectral PA acquisition sequence.

The specific optical flow implementation we use is by Farnebäck et al.[6] and part of the Open CV library[¶]. Knowing that the motion we want to compensate for is relatively small and quite homogeneous with no small structures moving independent of the surrounding tissue, we want an optical flow estimation which is approximated with a smooth surface – a blurred motion field. In addition, we aim for a fast (real-time capable) computation. Because of that we only perform two iterations (`iterations = 2`) and chose a large averaging window and neighborhood (specifically: `winsize = 40`, `poly_n = 7`, `poly_sigma = 1.5`). This will result in a blurred motion field that has the desirable side-effect of yielding a more robust algorithm.

[‡]see `http://docs.mitk.org/nightly/mitkPython_Overview.html`

[§]`scipy.optimize.nnls` using python 2.7

[¶]as `cv2.calcOpticalFlowFarneback` in phython 2.7

3.2 Validation experiments

The purpose of our validation experiments was to demonstrate the applicability of our platform to a translational research field. The validation experiments of the MITK PAUS real-time imaging platform were performed on data acquired with the platform. Two experiments were performed with the goal to (1) estimate blood oxygenation in peripheral vessels, namely the radial and ulnar arteries and to (2) estimate blood oxygenation the carotid artery. Both (1) and (2) require oxygenation estimation as detailed in section 3.1.1 and (2) requires additional motion correction as detailed in section 3.1.2. While the data acquired for the experiments was processed and visualized as B-Mode images (both PA and US) in real-time, we performed the analysis for the experiments offline on the data recorded beforehand by MITK. However, oxygenation estimation and motion correction have been both implemented to be real-time capable. Both *in vivo* PAUS experiments were performed free hand on healthy human volunteers while aiming to hold the probe as still as possible while acquiring approximately twenty seconds of data. Imaging of the carotid artery was performed by a vascular surgeon. The acquired raw PA data was corrected for fluctuations in laser pulse energy and then beamformed using the commonly used Delay and Sum (DAS) algorithm[4] with Hanning apodization.

4. RESULTS

During the acquisition of the presented data, the user had a real-time view of both US and PA images at frame rates of 13 to 20 Hz. The fast tuned PA acquisition wavelength sequence of the OPO laser was measured as $(722, 756, 831, 907, 943)$ nm with an accuracy of 1.5 nm. In the following we show oxygenation measurements in peripheral vessels and the effect of motion correction on sO_2 estimations in a carotid artery.

4.1 Blood oxygenation in peripheral vessels

Fig. 3 shows a representative example of sO_2 estimation in the radial artery and accompanying vein. sO_2 is visualized by thresholding the total hemoglobin from the unmixing results. The average sO_2 in the radial and ulnar artery was $SaO_2 = 72\% \pm 7\%$ averaged over a total of $n = 436$ mean oxygenations in a region of interest as marked in Fig. 3. The radial artery has been scanned twice, likewise the ulnar artery. The sO_2 in the accompanying vein of the radial artery was on average $SvO_2 = 38\% \pm 9\%$ over a total of $n = 238$ mean oxygenation estimations during two scans on the same healthy human volunteer.
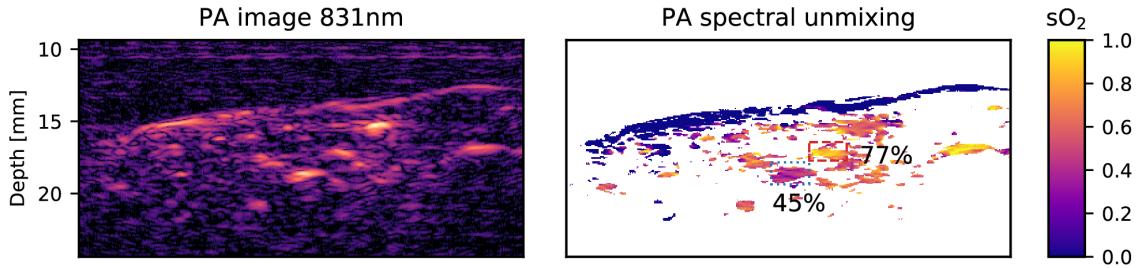
Figure 3. Representative photoacoustic (PA) B-mode image and blood oxygenation (sO_2) estimation in the radial artery and accompanying vein of a healthy human volunteer. The PA image is shows logarithmically compressed. The sO_2 estimation is visualized for pixels with relevant total hemoglobin results unmixed from one sequence of five wavelengths. The dashed red box deli the region of interest for arterial sO_2, the dotted blue box for venous. The average sO_2 values for this image are denoted on the boxes.

4.2 Motion correction and blood oxygenation estimation in the carotid artery

Estimating the optical flow for four $(350 \times 200$ px sized) US images of a sequence relative to the first US images in that sequence and warping the acquired PA and US images accordingly took (120 ± 10) ms (averaged over $n = 84$

sequences acquired in one scan) with python on a single core (2.6 GHz Intel Core i5-3230M). Fig. 4 illustrates the y position of the upper arterial wall in the US images of the acquisition sequences before and after the application of our optical flow based method by plotting the position of the maximum intensity pixel in the center of the upper arterial wall.
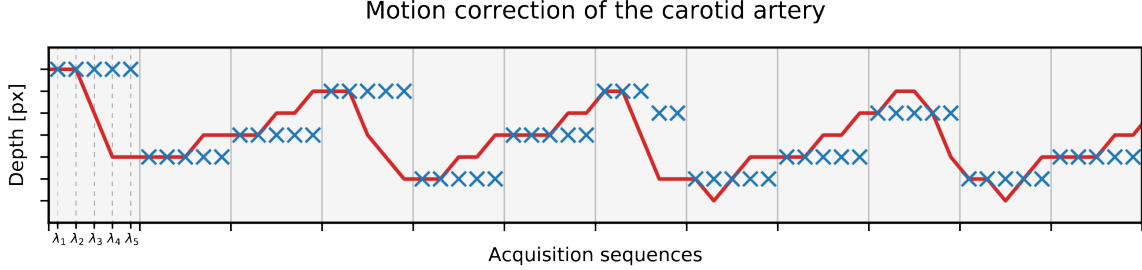
Figure 4. Illustration of motion correction in the first acquisition sequences; each sequence consisting of five images acquired at different wavelengths λ. The depth (y position of the upper arterial wall) in the ultrasonic (US) images is plotted before (red, $-$) and after the application of optical flow motion compensation (blue, $\times$). The periodic shift in position due to expansion of the carotid artery at a frequency corresponding to the resting heart rate of the volunteer is apparent.

Fig. 5 shows a section of the carotid artery and its corresponding oxygenation. The oxygenation was estimated based on the motion corrected stack of PA images. Average sO$_2$ in carotid artery and jugular vein is denoted on the regions of interest shown as red and blue boxes. An example of artifacts resulting from spectral unmixing on sequences not corrected for motion is shown in Fig. 6. We measured the oxygenation saturation with 84 image
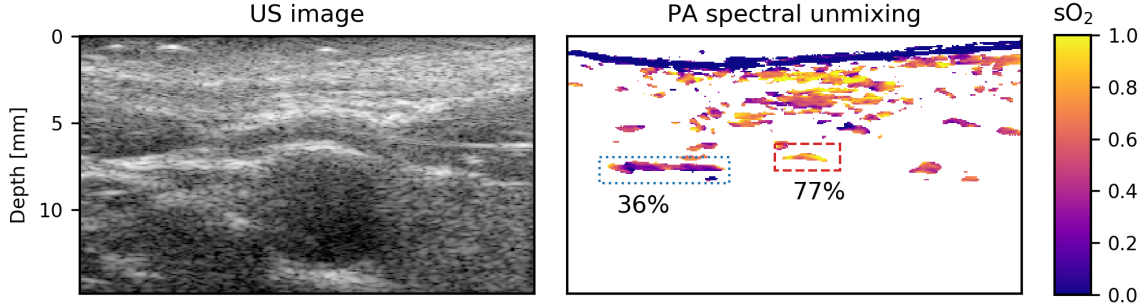
Figure 5. Representative ultrasonic (US) image of a carotid artery with corresponding blood oxygenation (sO$_2$) estimation with applied *optical flow* motion correction. The dashed red box is the region of interest for arterial blood oxygenation(sO$_2$), the dotted blue box for venous. The average sO$_2$ values for this image are denoted on the boxes.

sequences of the carotid artery. Estimating on images uncorrected for motion yielded mean(SaO$_2$) = 59 % when averaging over the $n = 29,861$ pixels over the THb threshold. The standard deviation of the measurement was std(SaO$_2$) = 31 %. After *optical flow in sequence (ofis)* motion correction we measured SaO$_2^{ofis}$ = (63 ± 17) % over $n = 12,172$ pixels. In the accompanying jugular vein the estimation changed from SvO$_2$ = (40 ± 21) % without motion correction to SvO$_2^{ofis}$ = (38 ± 15) % with motion correction. The distributions of sO$_2$ over all pixels is shown in the violin plots of Fig. 6. As some of these are no normal distributions, we also determined their inter quartial ranges (IQR): For arterial blood a reduction from IQR(SaO$_2$) = 50 % to IQR(SaO$_2^{ofis}$) = 25 % for venous blood a reduction from IQR(SvO$_2$) = 29 % to IQR(SvO$_2^{ofis}$) = 19 %.
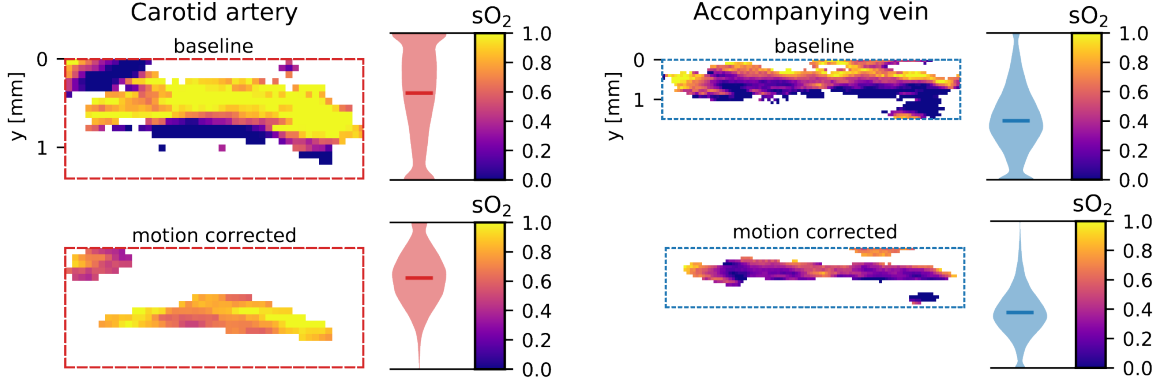
Figure 6. Representative blood oxygenation (sO_2) estimation by unmixing from photoacoustic (PA) images of a carotid artery (left) and vein (right) as well as the same estimations with applied *optical flow in sequence (ofis)* motion correction (bottom). The motion artifact in the artery is apparent in the top-left image and is vastly suppressed in the bottom-left. The attached violin plots show the distribution of the sO_2 measurements over all pixels in the region of interest from $n = 84$ sequences. A multimodal distribution of sO_2 in the carotid artery is apparent without motion correction. The inter quartial ranges (IQR) for the plotted distributions are: in arterial blood a reduction from $IQR(SaO_2) = 50\%$ to $IQR(SaO_2^{ofis}) = 25\%$ with motion correction; in venous blood a reduction from $IQR(SvO_2) = 29\%$ to $IQR(SvO_2^{ofis}) = 19\%$.

5. DISCUSSION

In this paper we present a real-time PAUS imaging platform with a linear array probe using a fast tuning laser. Within the open-source software platform MITK we provide implementations for direct control of the US DAQ and laser systems and their components. The presented software components are highly reusable and extensible due to the modular architecture of MITK. This should make it possible to use the project as a starting point for translational research projects with PA imaging. For each specific laser or DAQ system, only the hardware layer would have to be extended to comply with new APIs.

Furthermore we provide a method for correcting inter-frame motion as encountered in a clinical sample application which we presented as a demonstration use case of our system. In this clinical sample application we imaged the carotid artery of a healthy human volunteer. In this context we were faced with problematic inter-frame motion due to the pulsing artery. To address this issue we presented a new method for motion correction of multispectral PA image sequences using *optical flow* in seqence (ofis) on corresponding US images. Run time measurements of this methods show the real-time capability of the method considering motion correction of a sequence of five corresponding PA images is performed in 120 ms in our python implementation running single threaded on a consumer CPU core – while the sequence acquisition takes 250 ms with out fast tuning OPO. The motion correction method succeeds in reducing motion artifacts and the sO_2 estimations with applied motion correction make it possible to clearly distinguish between arterial and venous blood. The variation of estimated sO_2 is reduced as shown by the drop in standard deviation when correction for motion and illustrated in Fig. 6. This shows a higher precision of sO_2 estimation by spectral unmixing when correcting for inter-frame motion. It is to our knowledge the first inter-frame motion correction approach using corresponding US images or optical flow.

While the sO_2 estimates when using motion correction are more consistent and closer to the physiological values in a healthy human,[24] there is a systematic underestimation of oxygenation with our data. This is also the case in more superficial vessels, but to a lesser degree. We attribute this underestimation to (1) fluence effects due to a high overall oxygenation in tissue – this should be addressed quantitatively[20, 25] and to a lesser degree (2) noise levels.

We have presented a starting point for translational PAUS imaging research integrated in the open-source MITK platform. We validated its performance on a clinical sample application, were we were able to show that

we can image the carotid artery multispectrally by correcting for inter-frame motion using an optical flow based approach.

ACKNOWLEDGMENTS

REFERENCES

[1] Taruttis, A. and Ntziachristos, V., "Advances in real-time multispectral optoacoustic imaging and its applications," *Nature Photonics* **9**(4), 219–227 (2015).

[2] Gerling, M., Zhao, Y., Nania, S., Norberg, K. J., Verbeke, C. S., Englert, B., Kuiper, R. V., Bergström, Å., Hassan, M., Neesse, A., et al., "Real-time assessment of tissue hypoxia in vivo with combined photoacoustics and high-frequency ultrasound," *Theranostics* **4**(6), 604 (2014).

[3] Mohajerani, P., Tzoumas, S., Rosenthal, A., and Ntziachristos, V., "Optical and optoacoustic model-based tomography: theory and current challenges for deep tissue imaging of optical contrast," *IEEE Signal Processing Magazine* **32**(1), 88–100 (2015).

[4] Kim, J., Park, S., Jung, Y., Chang, S., Park, J., Zhang, Y., Lovell, J. F., and Kim, C., "Programmable real-time clinical photoacoustic and ultrasound imaging system," *Scientific reports* **6** (2016).

[5] Nolden, M., Zelzer, S., Seitel, A., Wald, D., Müller, M., Franz, A. M., Maleike, D., Fangerau, M., Baumhauer, M., Maier-Hein, L., Maier-Hein, K. H., Meinzer, H. P., and Wolf, I., "The medical imaging interaction toolkit: challenges and advances," *International Journal of Computer Assisted Radiology and Surgery* **8**, 607–620 (Jul 2013).

[6] Farnebäck, G., "Two-frame motion estimation based on polynomial expansion," *Image analysis* **1**, 363–370 (2003).

[7] American National Standards Institute, I., [*American National Standard for Safe Use of Lasers*], Laser Institute of America (2007).

[8] Ibanez, L., Schroeder, W., Ng, L., and Cates, J., "The itk software guide," (2005).

[9] Schroeder, W. J., Lorensen, B., and Martin, K., [*The visualization toolkit: an object-oriented approach to 3D graphics*], Kitware (2004).

[10] Culjak, I., Abram, D., Pribanic, T., Dzapo, H., and Cifrek, M., "A brief introduction to opencv," in [*MIPRO, 2012 proceedings of the 35th international convention*], 1725–1730, IEEE (2012).

[11] Guennebaud, G., Jacob, B., et al., "Eigen v3." http://eigen.tuxfamily.org (2010).

[12] Stone, J. E., Gohara, D., and Shi, G., "Opencl: A parallel programming standard for heterogeneous computing systems," *Computing in science & engineering* **12**(3), 66–73 (2010).

[13] Klemm, M., Kirchner, T., Gröhl, J., Cheray, D., Nolden, M., Seitel, A., Hoppe, H., Maier-Hein, L., and Franz, A. M., "Mitk-openigtlink for combining open-source toolkits in real-time computer-assisted interventions," *International journal of computer assisted radiology and surgery* **12**(3), 351–361 (2017).

[14] Kirchner, T., Sattler, F., Gröhl, J., and Maier-Hein, L., "Signed real-time delay multiply and sum beamforming for multispectral photoacoustic imaging," *Journal of Imaging* **4**(10) (2018).

[15] März, K., Franz, A. M., Seitel, A., Winterstein, A., Bendl, R., Zelzer, S., Nolden, M., Meinzer, H.-P., and Maier-Hein, L., "Mitk-us: real-time ultrasound support within mitk," *International journal of computer assisted radiology and surgery* **9**(3), 411–420 (2014).

[16] Hunder, G. G., Bloch, D. A., Michel, B. A., Stevens, M. B., Arend, W. P., Calabrese, L. H., Edworthy, S. M., Fauci, A. S., Leavitt, R. Y., Lie, J. T., Lightfoot, R. W., Masi, A. T., McShane, D. J., Mills, J. A., Wallace, S. L., and Zvaifler, N. J., "The American College of Rheumatology 1990 criteria for the classification of giant cell arteritis," *Arthritis & Rheumatism* **33**, 1122–1128 (Aug. 1990).

[17] Kim, M., Kang, J., Chang, J. H., Song, T.-K., and Yoo, Y., "Image quality improvement based on inter-frame motion compensation for photoacoustic imaging: A preliminary study," in [*Ultrasonics Symposium (IUS), 2013 IEEE International*], 1528–1531, IEEE (2013).

[18] Willemink, R., Slump, C., and van der Heijden, F., [*On image quality enhancement in photoacoustic image reconstruction by motion compensation*], 216–222, Technology Foundation (STW) (11 2006). http://eprints.ewi.utwente.nl/8919.

[19] Xia, J., Chen, W., Maslov, K., Anastasio, M. A., and Wang, L. V., "Retrospective respiration-gated whole-body photoacoustic computed tomography of mice," *Journal of biomedical optics* **19**(1), 016003–016003 (2014).

[20] Tzoumas, S., Nunes, A., Olefir, I., Stangl, S., Symvoulidis, P., Glasl, S., Bayer, C., Multhoff, G., and Ntziachristos, V., "Eigenspectra optoacoustic tomography achieves quantitative blood oxygenation imaging deep in tissues," *Nature communications* **7** (2016).

[21] Luke, G. P., Nam, S. Y., and Emelianov, S. Y., "Optical wavelength selection for improved spectroscopic photoacoustic imaging," *Photoacoustics* **1**(2), 36 – 42 (2013).

[22] Lawson, C. L. and Hanson, R. J., [*Solving least squares problems*], SIAM (1995).

[23] Horn, B. K. and Schunck, B. G., "Determining optical flow," *Artificial intelligence* **17**(1-3), 185–203 (1981).

[24] Zander, R., "The oxygen status of arterial human blood," *Scandinavian Journal of Clinical and Laboratory Investigation* **50**(sup203), 187–196 (1990).

[25] Kirchner, T., Gröhl, J., and Maier-Hein, L., "Context encoding enables machine learning-based quantitative photoacoustics," *Journal of Biomedical Optics* **23**, 1–9 (May 2018).

SIGNAL PROCESSING

J1

SIGNED REAL-TIME DELAY MULTIPLY AND SUM BEAMFORMING FOR MULTISPECTRAL PHOTOACOUSTIC IMAGING

This manuscript gives an introduction to PA beamforming with delay and sum – the most widely used image reconstruction algorithm for US transducer based PAI systems. It then presents a novel algorithm which improves the signal-to-noise ratio while not sacrificing linearity, as most algorithms that improve on delay and sum do. The real-time beamforming algorithms were implemented open-source within MITK.

Own contribution

The initial manuscript was drafted by me and edited and revised by all authors.

I conceived of the method. The implementation of the algorithm, I performed together with Franz Sattler. Franz Sattler coded the real-time capable GPU beamforming in MITK.

The experiments were designed by me, and performed by me and Janek Gröhl. I performed the post-processing and analysis for the data from the experiments.

Article

Signed Real-Time Delay Multiply and Sum Beamforming for Multispectral Photoacoustic Imaging

Thomas Kirchner [1,2,*] **, Franz Sattler** [1,2] **, Janek Gröhl** [1,3] **and Lena Maier-Hein** [1,3]

[1]   Division of Computer Assisted Medical Interventions (CAMI), German Cancer Research Center (DKFZ), 69120 Heidelberg, Germany; f.sattler@dkfz-heidelberg.de (F.S.); j.groehl@dkfz-heidelberg.de (J.G.); l.maier-hein@dkfz-heidelberg.de (L.M.-H.)
[2]   Faculty of Physics and Astronomy, Heidelberg University, 69120 Heidelberg, Germany
[3]   Medical Faculty, Heidelberg University, 69120 Heidelberg, Germany
*   Correspondence: t.kirchner@dkfz-heidelberg.de

check for
updates

Abstract: Reconstruction of photoacoustic (PA) images acquired with clinical ultrasound transducers is usually performed using the Delay and Sum (DAS) beamforming algorithm. Recently, a variant of DAS, referred to as Delay Multiply and Sum (DMAS) beamforming has been shown to provide increased contrast, signal-to-noise ratio (SNR) and resolution in PA imaging. The main reasons for the use of DAS beamforming in photoacoustics are its simple implementation, real-time capability, and the linearity of the beamformed image to the PA signal. This is crucial for the identification of different chromophores in multispectral PA applications. In contrast, current DMAS implementations are not responsive to the full spectrum of sound frequencies from a photoacoustic source and have not been shown to provide a reconstruction linear to the PA signal. Furthermore, due to its increased computational complexity, DMAS has not been shown yet to work in real-time. Here, we present an open-source real-time variant of the DMAS algorithm, signed DMAS (sDMAS), that ensures linearity in the original PA signal response while providing the increased image quality of DMAS. We show the applicability of sDMAS for multispectral PA applications, in vitro and in vivo. The sDMAS and reference DAS algorithms were integrated in the open-source Medical Imaging Interaction Toolkit (MITK) and are available as real-time capable implementations.

Keywords: photoacoustics; image reconstruction; multispectral imaging; signal processing; delay and sum; delay multiply and sum

1. Introduction

Currently, almost all applications of photoacoustic (PA) or ultrasonic (US) imaging, where real-time capability is crucial, use the straightforward Delay and Sum (DAS) beamforming algorithm [1,2]. Its linear complexity ensures very short computing times even on a central processing unit (CPU), but, in comparison to other beamforming algorithms, it suffers from worse contrast and Signal-to-Noise Ratio (SNR) [3]. The Delay Multiply and Sum (DMAS) beamforming algorithm, an extension to DAS beamforming, has recently been proposed for US B-Mode images [4] and has been shown to improve image quality also when applied to the field of photoacoustics [5]. On the other hand, DMAS is computationally expensive with a complexity of $\mathcal{O}(n^2)$ compared to the DAS complexity of $\mathcal{O}(n)$. Furthermore, DMAS, as proposed by Matrone et al. [4], is a non-linear beamformer [6] that has not yet been confirmed to produce a linear response, which is a necessity for multispectral applications. DMAS also needs to be post-processed with a bandpass filter (F-DMAS) to remove a low frequency artifact introduced by the algorithm, which affects PA data [7] as well as US data. While filtering is not problematic for US imaging, doing so with PA imaging systems that are sensitive to lower acoustic

frequencies would also remove valuable PA information, as PA signal responses have a substantial low frequency contribution [8].

The contribution of this paper is two-fold:

(1) We present a modified DMAS algorithm which we call signed DMAS (sDMAS). The modification addresses the non-linear optical and acoustic frequency response of conventional DMAS. We show linearity of sDMAS based B-Mode image reconstruction with respect to the source signal, which makes sDMAS usable for spectroscopic applications.
(2) We present a graphics processing unit (GPU)-based implementation of the sDMAS algorithm which is real-time capable and therefore usable in a clinical setting. This is validated on a tissue mimicking PA characterization phantom and applied by measuring blood oxygenation in vivo on the radial artery of a healthy human volunteer.

The implementation of the contributions of this paper, as well as all other algorithms used, are provided open-source as an extension of the Medical Imaging Interaction Toolkit (MITK) [9], and are applicable to both PA and US image data.

2. Materials and Methods

The first two parts of this section review the reference beamforming algorithms DAS (Section 2.1) and DMAS (Section 2.2) as applied in this paper. Section 2.3 introduces the proposed DMAS variant, sDMAS, and motivates theoretically how it achieves linearity to the original PA signal. Finally, Section 2.5 provides implementation details for all beamforming algorithms.

2.1. Delay and Sum Beamforming

DAS beamforming is the most common and widely used method for reconstructing photoacoustic and ultrasonic images in real-time applications [2,4]. The first step in beamforming an image is to calculate the delays at which a signal originating at some depth y and lateral position x arrives at each of the elements of the transducer. We assume to this end spherical waves coming from the positions we want to reconstruct. Furthermore, we consider a linear transducer consisting of N elements spaced with a distance Δx and a spatially constant speed of sound c.

As illustrated in Figure 1, the delay τ after which a wave originating at lateral position x at a depth y arrives at the element j is:

$$\tau(x,y,j) = \frac{\sqrt{y^2 + (|x - j \cdot \Delta x|)^2}}{c} \tag{1}$$

The DAS algorithm proceeds by summing up the delayed signals of one position (x,y). We call the signal response measured by transducer element j, at a time τ, $S(j,\tau)$. For a reconstructed pixel at position (x,y), the beamformed signal S_{DAS} is therefore:

$$S_{\text{DAS}}(x,y) = \sum_{j=1}^{N} S(j, \tau(x,y,j)) \cdot A_x(j) \tag{2}$$

where $0 \leq A_x(j) \leq 1$ is an apodization function, which can be used to reduce side lobes and similar beamforming related artifacts, usually by weighting the transducer elements near x stronger than those far away [10].

The complexity of the algorithm can be approximated to be proportional to the number of summations, and is therefore $\mathcal{O}(N)$ for DAS.
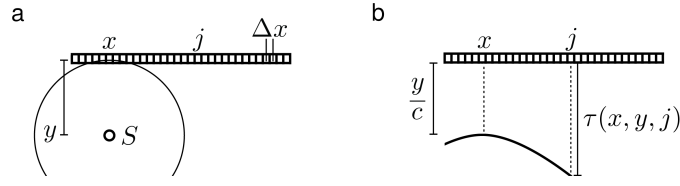
Figure 1. (**a**) Illustration of a signal *S* originating at depth *y* and lateral position *x* relative to a transducer array with example element *j* and propagating as a spherical acoustic wave with speed *c*; (**b**) Illustration of the same scenario in the time domain of pressure recorded in the transducer array (radio frequency (rf) data), where $\tau(x, y, j)$ denotes the propagation time of that signal *S*.

2.2. Delay Multiply and Sum Beamforming

The DMAS algorithm as proposed by Matrone et al. [4] improves on DAS by relating each signal response on each transducer to a single signal position by summing over the products of all non-identical combinations of responses. This has the intention of amplifying actual source signals and reducing noise. To retain linear units, the signed square root of the sums is taken to be the beamformer response. The correlation matrix $M_{nm}(x, y)$ of the signals of the transducer elements *n* and *m*, delayed for a signal at lateral position *x* at depth *y*, is introduced:

$$M_{nm}(x,y) = S(n, \tau(x,y,n)) \cdot A_x(n) \cdot S(m, \tau(x,y,m)) \cdot A_x(m) \tag{3}$$

The reconstructed signal $S_{\text{DMAS}}(x, y)$ is then defined as:

$$S_{\text{DMAS}}(x,y) = \sum_{n=1}^{N-1} \sum_{m=n+1}^{N} \text{sign}(M_{nm}(x,y)) \sqrt{|M_{nm}(x,y)|} \tag{4}$$

While $M_{nm}(x, y)$ is always positive in an ideal tissue and the absence of noise, $\text{sign}(M_{nm}(x, y))$ is introduced in the equation to reduce the mean calculated value for noise and artifacts.

The number of summations necessary to determine S_{DMAS} is $\frac{N^2 - N}{2}$. Therefore, in view of *N* being negligible against N^2, computational complexity can be concluded to be $\mathcal{O}(N^2)$ for DMAS.

2.3. Signed Delay Multiply and Sum Beamforming

In previous DMAS implementations [4], it was necessary to post-process the image after beamforming by using a bandpass filter, as the loss of the sign introduces an additional low frequency component to the actual signal, which is suppressed using the bandpass filter. Unlike in ultrasound imaging, photoacoustic signals usually have a broad acoustic spectrum and therefore contain low acoustic frequencies. These signal contributions will be filtered as well, which may lead to a suppression of important signal components.

In our implementation, we overcome this issue by keeping the sign of the original signal which is equivalent to integrating $\text{sign}(S_{\text{DAS}})$ into Equation (4)

$$S_{\text{sDMAS}}(x,y) = \text{sign}(S_{\text{DAS}}(x,y)) \cdot S_{\text{DMAS}}(x,y) \tag{5}$$

Keeping the sign of the original signal allows us to apply sDMAS for multispectral PAT application, as shown in the following paragraph.

Here, the number of summations necessary to determine S_{sDMAS} differs from the case of DMAS only in the *N* operations for the DAS coefficient; therefore, the number of necessary summations is $\frac{N^2 + N}{2}$. Even so, the summations for DAS require far less operations than those for DMAS; either way, we can approximate the complexity of sDMAS to be $\mathcal{O}(N^2)$, the same as for DMAS.

2.4. Linearity of Beamforming Algorithms

Spectral unmixing of multispectral photoacoustic signals assumes linearity of those signals to the underlying absorption coefficient. While this assumption usually breaks down due to fluence effects, we can still assure that we do not introduce further errors in our estimation through the beamforming algorithm. To show that a beamforming algorithm reconstructs a signal $S_{\text{BF}}(x, y, \lambda)$ linear to the originating signal $S_0(x, y, \lambda)$, we need to show that

$$S_{\text{BF}}(x, y, \lambda) = C(x, y) \cdot S_0(x, y, \lambda) \tag{6}$$

where $C(x, y)$ has to be a real number, independent of λ, for any given position (x, y). In the following, we show that this is the case for DAS but not for DMAS, and how we can remedy this by introducing sDMAS.

Whenever a PA signal originating at position (x, y) arrives at transducer element j, the sound wave traveled a distance $d(x, y, j) = c \cdot \tau(x, y, j)$. The signal will have experienced signal attenuation. This acoustic attenuation in a homogeneous medium is $e^{-\alpha(\omega)d}$, where $\alpha(\omega)$ is the sound attenuation coefficient dependent on sound frequency ω and medium. The acoustic signals generated in the tissue during PA image acquisition depend on the optical properties of the tissue and are wavelength dependent. Let $S_0(x, y, \lambda)$ denote the signal that originates as a spherical wave in a sufficiently homogeneous medium at a position (x, y) in response to a laser pulse of wavelength λ. Then, the resulting attenuated signal $S(j, d(x, y, j), \lambda)$ arriving at transducer element j can be expressed as follows:

$$S(j, d(x, y, j), \lambda) = e^{-\alpha(\omega) \cdot c \cdot \tau(x, y, j)} \cdot S_0(x, y, \lambda) \tag{7}$$

In the following paragraphs, we examine the DAS, DMAS and sDMAS algorithms to see how their reconstructions depend on the original signal S_0.

2.4.1. Linearity of DAS

From the definition of the DAS beamformed signal (Equation (2)), we directly find linearity for S_{DAS} after introducing signal attenuation (Equation (7)) and λ explicitly.

$$
\begin{aligned}
S_{\text{DAS}}(x, y, \lambda) &= \sum_{j=1}^{N} \left(A_x(j) \cdot e^{-\alpha(\omega) \cdot c \cdot \tau(x, y, j)} \right) \cdot S_0(x, y, \lambda) \\
&= C_{\text{DAS}}(x, y) \cdot S_0(x, y, \lambda)
\end{aligned}
\tag{8}
$$

2.4.2. Linearity of DMAS

Using the definition of the DMAS beamformed signal (Equation (4)), we need to consider signal attenuation (Equation (7)) in $M_{nm}(x, y)$, extended for λ.

$$S_{\text{DMAS}}(x, y, \lambda) = \sum_{n=1}^{N-1} \sum_{m=n+1}^{N} \text{sign}(M_{nm}(x, y, \lambda)) \sqrt{|M_{nm}(x, y, \lambda)|} \tag{9}$$

$$\text{with} \quad M_{nm}(x, y, \lambda) = A_x(n) A_x(m) \cdot e^{-\alpha(\omega) \cdot c \cdot (\tau(x, y, n) + \tau(x, y, m))} \cdot S_0(x, y, \lambda)^2$$

From this expression of $M_{nm}(x, y, \lambda)$m, we see that its sign has to be $+1$, considering $A_x(j) \geq 0$.

$$
\begin{aligned}
S_{\text{DMAS}}(x, y, \lambda) &= \sum_{n=1}^{N-1} \sum_{m=n+1}^{N} \left(\sqrt{A_x(n) A_x(m)} \cdot e^{-\frac{1}{2}\alpha(\omega) \cdot c \cdot (\tau(x, y, n) + \tau(x, y, m))} \cdot |S_0(x, y, \lambda)| \right) \\
&= C_{\text{DMAS}}(x, y) \cdot |S_0(x, y, \lambda)|
\end{aligned}
\tag{10}
$$

which means that, in DMAS beamforming, we lose the original sign of the signal.

2.4.3. Linearity of sDMAS

We aim to recover this lost sign with sDMAS (Equation (5)) by introducing the sign of S_{DAS} into DMAS

$$
\begin{aligned}
S_{\text{sDMAS}}(x,y,\lambda) &= \text{sign}(S_{\text{DAS}}(x,y,\lambda)) \cdot S_{\text{DMAS}}(x,y,\lambda) \\
&= \text{sign}(S_{\text{DAS}}(x,y,\lambda)) \cdot C_{\text{DMAS}}(x,y) \cdot |S_0(x,y,\lambda)|
\end{aligned}
\tag{11}
$$

from which we can restore the sign of S_0 lost in DMAS, because all other terms in S_{DAS} (Equation (8)) are positive ($A_x(j) \geq 0$ and $e^r \geq 0$ because r is a real number).

$$
\begin{aligned}
S_{\text{sDMAS}}(x,y,\lambda) &= \text{sign}(C_{\text{DAS}}(x,y)) \cdot C_{\text{DMAS}}(x,y) \cdot \text{sign}(S_0(x,y,\lambda)) \cdot |S_0(x,y,\lambda)| \\
&= C_{\text{sDMAS}}(x,y) \cdot S_0(x,y,\lambda)
\end{aligned}
\tag{12}
$$

Note that we did not explicitly model noise $N(x,y,\lambda)$ corresponding to the measured signals $S(j,d(x,y,j),\lambda)$ as we assume $S_0(x,y,\lambda) \gg N(x,y,\lambda)$ for the source signals of interest. If the original signal is too small—on a noise equivalent level—linearity cannot be ensured. In the absence of noise, the sign of S_{DMAS} is always positive for an emerging signal S_0, which means that the sign of the original signal is lost through the DMAS double summation process. In contrast, the sign of the original signal is not lost in sDMAS, because we inserted the factor $\text{sign}(S_{\text{DAS}})$ thereby eliminating the need for further post-processing with a bandpass filter. Other than that, both beamforming algorithms can be regarded as proportional to the original signal in each beamformed position (x,y). This is regardless of choice in apodization function (as long as $A_x(j) \geq 0$) but assuming the same acoustic spectrum of the source. For a spectroscopic PA application of DMAS, the acoustic spectrum ω has to be independent of PA excitation wavelength but can and will depend on the tissue under examination [11].

2.5. Implementation of Beamforming Algorithms

Our implementation of the beamforming algorithms running on a CPU has been multithreaded, but the attainable speed is nevertheless limited. We therefore added implementations of DAS, DMAS and sDMAS using the GPU through the Open Computing Language (OpenCL) [12], which enables us to get increased performance through the massive parallelization of the beamforming algorithms. Delays $\tau(i,j,y)$ for the whole image are computed for a given speed of sound c and up to a maximum scan depth and saved in a persistent GPU buffer. Whenever relevant beamforming parameters change a renewed calculation of the delay buffer is needed. The number of transducer elements which are used for the calculation of a pixel is determined by the sensitive angle, therefore the apodization is also computed beforehand by a separate OpenCL kernel and saved in a persistent buffer. The actual beamforming kernel uses the previously computed buffers to sum over the needed input values according to DAS or sDMAS. In doing so, the main performance limitation is the memory access time on the GPU. Furthermore, we use $A_x(j) = 1$, for all x and j for the calculation of $\text{sign}(S_{\text{DAS}})$, as apodization mainly increases SNR, but the sign of actual signals remains unaffected. Therefore, to reduce computational cost, we refrain here from using an apodization function.

In contrast to the original DMAS formulation, sDMAS does not rely on a bandpass filter as integral part of the beamforming process, which increases performance, as bandpass filters rely on two computationally intensive Fourier transforms. Nevertheless, we provide a bandpass filter as an optional processing step for our implementations of DAS, DMAS and sDMAS as it can reduce noise and artifacts. Our bandpass implementation performs first a Fourier transform of the beamformed image in depth direction using the Fast Fourier Transform (FFT) implementation of the Insight Imaging Toolkit (ITK), then multiplies the resulting image with a Tukey window which can be adjusted to select the desired band of frequencies and gives the option to smoothly set the boundaries of that band to

zero [13]. Afterwards, an inverse FFT is applied. The ITK FFT implementation runs on CPU exclusively. Regarding apodization, our MITK implementation supports boxcar, Hanning, and Hamming.

3. Experiments and Results

The purpose of our experiments was to characterize the sDMAS beamforming algorithm in vitro and apply it in vivo for qualitative validation. The first experiment (Section 3.1) characterizes sDMAS beamforming in a controlled in vitro setting and shows both its real-time capability and the linearity. The second experiment (Section 3.2) comprises in vivo measurements on a healthy human volunteer to estimate blood oxygenation (sO$_2$) with varying beamformers.

In our setup, raw PA data acquisition is performed using MITK with the DiPhAS US system (Fraunhofer IBMT, St. Ingbert, Germany) and a 128-element linear US transducer operating on a center frequency of 7.5 MHz (L7-Xtech, Vermon, Tours, France). The light from a fast tuning OPO laser (Phocus Mobile, Opotek, Carlsbad, CA, USA) is delivered via a custom fiber bundle to the probe and into the tissue or phantom. A pulse energy of up to 40 mJ at a pulse repetition rate of 20 Hz is delivered over a surface of 2 cm^2 to avoid tissue damage [14]. After the data acquisition, beamforming is performed with the MITK PA image processing plugin [15].

3.1. Beamforming Characterization

The phantom used to characterize the performance of our sDMAS implementation in comparison to DAS and DMAS consists of diluted milk as background medium and a methylene blue solution in silicone tubing with an inner diameter of 1 mm spaced 5 mm apart both vertically and horizontally. To achieve a reduced scattering comparable with tissue ($\mu_s' \approx 15$ cm^{-1} in the near infrared range) [16], the optical properties of concentrated (10% fat) milk and methylene blue were measured by a spectroscopic method [17] and then diluted to yield the desired optical properties, as shown in Figure 2c. The wavelength of the acquisition was varied between 700 and 800 nm to generate PA signals corresponding to a range of absorption coefficients μ_a between 21 and 1.4 cm^{-1}.
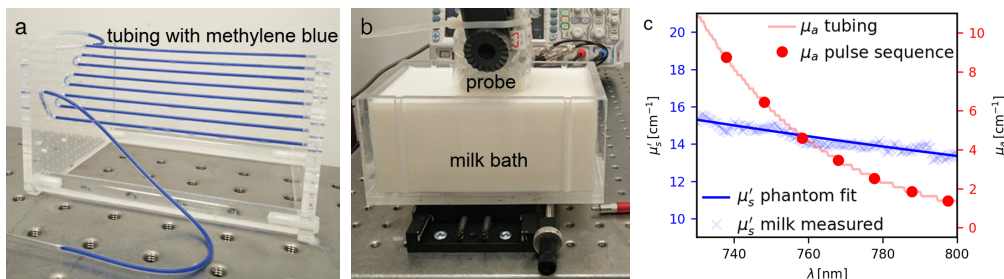
Figure 2. The characterization phantom, consisting of (**a**) an array of silicone tubing filled with diluted methylene blue and placed inside (**b**) a tank filled with diluted milk. (**c**) The methylene blue in the tubing was diluted to yield absorption coefficients as encountered in blood in the near infrared range (the overlaid dots are the wavelengths of the acquisition sequences). The milk was diluted to yield a reduced scattering coefficient consistent with tissue.

Before our characterization experiment, we imaged tubing filled only with water, using the same wavelength sequence to ensure that there was no PA signal contribution by the tubing itself. In these measurements we did not see any PA signal above a noise equivalent level. The characterization phantom was then filled with the diluted methylene blue and measured at a fixed position, as shown in Figure 2a. For each wavelength $n = 100$ measurements were performed. Beamforming of raw data from the 128-element transducer was performed to 256 beamformed lines with 2048 samples and up to a depth of 3.8 cm. The speed of sound for that reconstruction was set to 1474 m s^{-1} as calculated

using the corresponding US measurement. Beamforming was performed with with DAS, DMAS and sDMAS using both Hanning and boxcar apodization and with or without a subsequent bandpass filter. When a Tukey bandpass filter was used, it was always applied after beamforming and set to $\alpha = 0.5$ with a nominal range from 0 to 10 MHz. B-Mode images were formed by a Hilbert transform based envelope detection and subsequent down-sampling to a 0.15 mm equal spacing.

A section of the B-Mode images from the phantom which corresponds to $\mu_a = 8.5\,\text{cm}^{-1}$ is shown in Figure 3. Bandpass filtered (F) images are shown in the second row. To quantify the improvement in image quality when using sDMAS, we use the Contrast-to-Noise Ratio (CNR) defined as in [18]:

$$\text{CNR} = 20 \cdot \log_{10}\left(\frac{\langle S \rangle - \langle N \rangle}{\sigma(N)}\right) \quad \text{in db} \tag{13}$$

with $\langle S \rangle$ being the mean signal intensity in a region of interest, $\langle N \rangle$ the mean noise intensity and $\sigma(N)$ the standard deviation of the noise in the adjacent background, as highlighted in Figure 3.
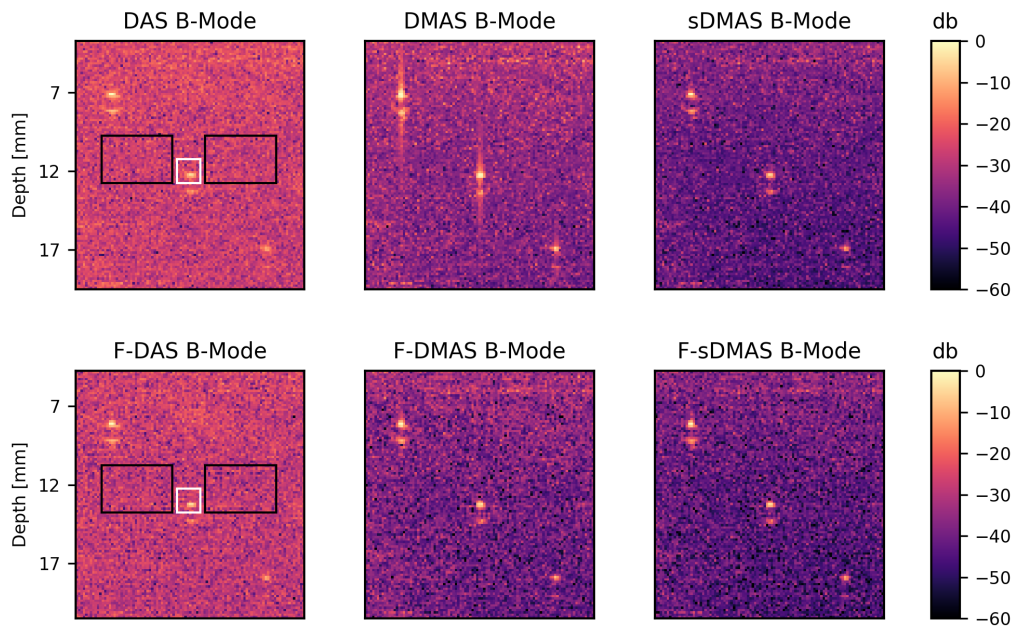
Figure 3. Visualization of B-Mode PA images with logarithmic compression using DAS, DMAS and sDMAS beamforming in the first row, with an additional bandpass filter (F) applied in the second row. The PA signals from the upper and lower boundaries of the tubes are visible with a distance of 1 mm. For the purpose of ascertaining a CNR ratio as defined in Equation (13), the white box indicates the signal S and the black boxes the corresponding noise N. These regions are identical for all algorithms. The images shown are a representative example, beamformed using a boxcar apodization using an acquisition wavelength corresponding to an absorption coefficient of $\mu_a = 8.5\,\text{cm}^{-1}$ inside the tubing.

We determine $\langle S \rangle$ from the area highlighted as a white box in Figure 3 and $\langle N \rangle$ as well as $\sigma(N)$ from the corresponding two black boxes. The increases in CNR using sDMAS over DAS are averaged over $n = 100$ and three depths (8, 13 and 18 mm—the three tube sections shown in the figure). As shown in Table 1, when apodization and bandpass filter are the same for both algorithms, CNR using sDMAS beamforming is consistently at least twice the CNR as when using DAS beamforming (>6 db). In addition, sDMAS improved over DAS regardless of apodization and bandpass for our settings. Sections of B-Mode images with boxcar apodization are shown in Figure 3, which also shows that sDMAS does not suffer from artifacts due to the low frequency term usually introduced in DMAS

beamforming. The bandpass filter is therefore an optional step in sDMAS beamforming. The increase in CNR had a depth dependence, with the CNR increasing an average of 1 db more for the structure at 13 mm depth, and having a higher standard deviation at higher depths. In additionl as shown in Table 2, the experiments suggest a 2 db increase in CNR using F-sDMAS over F-DMAS and a similar CNR when comparing sDMAS to F-DMAS.

Table 1. Increase in CNR using sDMAS in different variants (columns) compared to DAS in different variants (rows) in db for $\mu_a = 8.5\,\text{cm}^{-1}$. *Box* and *Hann* denotes if box car or Hanning apodization is compared. *F* denotes the use of a bandpass filter. For instance, the sDMAS algorithm with boxcar apodization and no bandpass filter (sDMAS, Box, -) on average yielded an improvement of 8 db in CNR over the DAS algorithm with boxcar apodization and using a bandpass filter (DAS, Box, F). CNRs are averaged over $n = 100$ slices and three signals in depths of 8 mm to 18 mm. The increases in CNR over the three structures in different depths had standard deviations of 2 db.

					sDMAS		
				Box		**Hann**	
				F	**—**	**F**	**—**
DAS	Box	F		9	8	11	9
		—		9	7	11	9
	Hann	F		6	4	8	6
		—		6	5	8	6

Table 2. CNR of DAS, DMAS and sDMAS in db for $\mu_a = 8.5\,\text{cm}^{-1}$. CNRs are averaged over $n = 100$ slices and listed for three signal positions. The CNRs for depths 8 mm and 13 mm had a standard deviation of ≈ 1 db. For the depth of 18 mm the standard deviation was ≈ 1.5 db.

	DAS				**F-DMAS**		**sDMAS**			
	Box		**Hann**		**Box**	**Hann**	**Box**		**Hann**	
Depth	**F**	**—**	**F**	**—**			**F**	**—**	**F**	**—**
8 mm	5	5	8	7	10	11	12	10	14	11
13 mm	4	5	8	7	12	14	14	13	17	15
18 mm	−3	−2	0	0	6	8	8	6	10	8

The runtimes of the sDMAS and DAS algorithms, as listed in Table 3, were measured on the characterization phantom dataset with $n = 1300$ recorded frames and for a reconstruction depth of 3.9 cm. The reconstruction was performed running MITK on a Ubuntu 18.04 operating system using a i7-5960X CPU (Intel, Santa Clara, CA, USA) and a GeForce GTX 970 GPU (Nvidia, Santa Clara, CA, USA). As the complexity of the DMAS and sDMAS algorithms is the same, the computational performance of DMAS has not been compared to sDMAS and DAS here explicitly.

Table 3. Runtime of our DAS and sDMAS implementations, processing one frame. The standard deviations of the runtimes are each smaller than 5% of the listed means. Choice of apodization had no impact on the runtime. The Tukey window bandpass as well as the B-Mode envelope detection were exclusively performed on CPU.

	DAS		**sDMAS**		**Bandpass**	**B-Mode**
Lines	**CPU**	**GPU**	**CPU**	**GPU**	**CPU**	**CPU**
128	29 ms	6 ms	502 ms	33 ms	9 ms	5 ms
256	58 ms	18 ms	990 ms	63 ms	18 ms	10 ms

In Figure 4, we plot the dependence of the signal intensity in the B-Mode images of the beamformed signals on the absorption coefficient of the methylene blue source in the tubing. We did this for the same three tubes as shown in Figure 3 using DAS and sDMAS with a boxcar apodization. A linear fit worked well for the three sources regardless of beamformer. Due to the lower noise level, using sDMAS beamforming, sDMAS has a smaller offset to the $x-$axis.
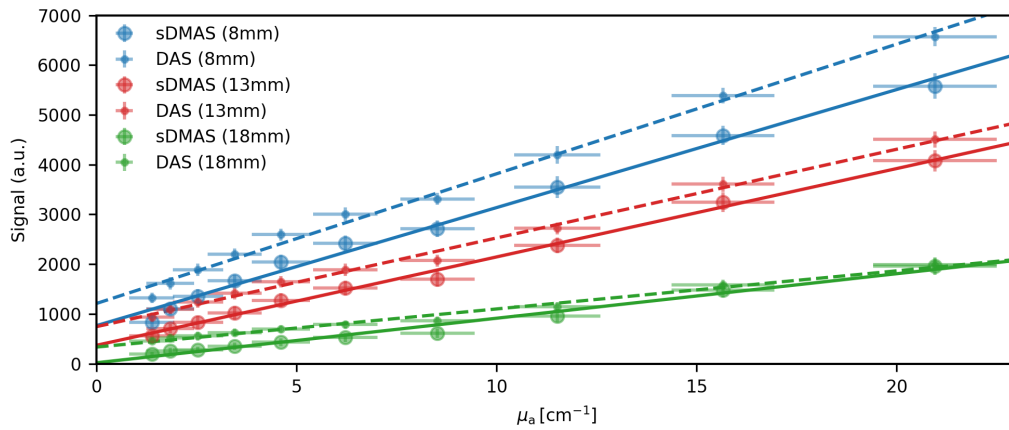

Figure 4. Comparison of the signal intensities dependence on the absorption coefficient. The maximum signal intensities in B-Mode images beamformed with DAS and sDMAS using boxcar apodization are averaged over $n = 100$ images for three sources. Linear fits are plotted alongside with the measured data. Both DAS and sDMAS have a proportional relation to the sources absorption coefficient when accounting for an additive noise term.

3.2. Blood Oxygenation Estimation

To demonstrate the increased quality of blood oxygenation estimation when using sDMAS instead of DAS, we recorded raw PA data of the radial artery and accompanying vein of a healthy human volunteer at five wavelengths in the near infrared. While a good ground truth for blood oxygenation is not easily obtained, in a healthy human, arterial blood is expected to have no less than 90% blood oxygenation [19], which we use as a qualitative reference. Based on the work of Luke et al. [20] and considering the power spectrum of our laser source, we altered our wavelength sequence from an equidistant spacing towards wavelengths with optimal differences between absorption of oxygenated and deoxygenated hemoglobin. The acquisition wavelength sequence was measured by a spectrometer (HR2000+, Ocean Optics, Dunedin, New Zealand) as $(722, 756, 831, 907, 943)$ nm with an accuracy of 1.5 nm. The acquired raw PA data were corrected for fluctuations in laser pulse energy and then beamformed using the DAS and sDMAS beamforming algorithms.

Spectral unmixing was performed using the non-negative constrained least squares solver scipy.optimize.nnls [21] on sets of five beamformed images, yielding abundances for hemoglobin and deoxygenated hemoglobin by fitting the spectra of the two chromophores to the five measured wavelengths in each pixel. The unmixing algorithm was implemented for CPU only, as its performance was not critical. Figure 5 shows a F-DAS and F-sDMAS beamformed example image recorded at an excitation wavelength of 831 nm. Sections of the radial artery and accompanying vein were identified by a vascular surgeon in the US image live stream of the acquisition system. The unmixing results for oxygenated (HbO_2) and deoxygenated hemoglobin (Hb) were used to calculate blood oxygenation and total hemoglobin (THb):

$$sO_2 = \frac{HbO_2}{Hb + HbO_2}, \qquad THb = Hb + HbO_2. \tag{14}$$

sO$_2$ is visualized by masking the results for low values of THb.

The median blood oxygenations sO$_2$ were averaged over $n = 84$ beamformed B-Mode images for both F-DAS and F-sDMAS. Using F-DAS, this yielded an estimation of arterial blood oxygenation $S_aO_2^{DAS} = 71\% \pm 6\%$ while the same unmixing on F-sDMAS yielded $S_aO_2^{sDMAS} = 89 \pm 6\%$. The estimation of venous blood oxygenation yielded $S_vO_2^{DAS} = 44\% \pm 7\%$ and $S_vO_2^{sDMAS} = 37 \pm 8\%$.
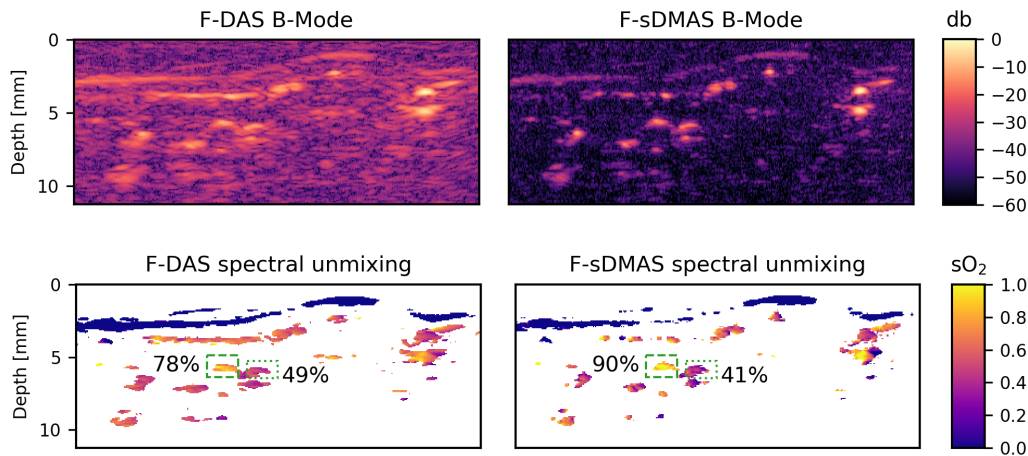

Figure 5. The radial artery and accompanying vein of a healthy human volunteer. Representative B-Mode images recorded at an acquisition wavelength of 831 nm are shown in the top row. Beamforming was performed using Hanning apodization and the images where postprocessed with a bandpass filter (F). In the second row, blood oxygenation (sO$_2$) is visualized. Only values with high total hemoglobin as determined by the spectral unmixing are shown. The dashed green box marks the artery and the dotted line the accompanying vein as identified by a consulting physician; both are annotated with the median oxygenation within these boxes.

4. Discussion

We presented a variant of the (F-)DMAS algorithm termed sDMAS that preserves linearity in the original signal response while increasing image quality. We implemented the sDMAS algorithm within MITK to be easily accessible and open-source to be easily reproducible and to address the lack of such resources in the field. A user manual for the software can be found here http://docs.mitk.org/nightly and demo installation packages with a sample of the raw data here http://mitk.org/wiki/Photoacoustics. We also provide reference DAS, DMAS implementations and bandpass filtering and include envelope detection algorithms for B-Mode imaging. Our results clearly show that our implementation is real-time capable (for frame rates of 20 Hz at which our imaging system operates), although there is a limit for the achievable image resolution when using consumer GPUs, as we did. Image quality was clearly improved using (F-)sDMAS compared to (F-)DAS. Due to this increase in CNR, we could also show that sDMAS B-Mode images are not only linear to the absorption coefficient of a source but also have a lower noise component than DAS, which systematically skews the spectral unmixing of DAS beamformed images more than for DMAS. This is finally illustrated in vivo on a healthy human volunteer's radial artery and accompanying vein. Although we are missing a reliable reference measurement, the spectral unmixing results of the arterial blood oxygenation for sDMAS (89%) are in closer agreement with the literature [19] than the S$_a$O$_2$ values using F-DAS, which estimated it as 71%, which is definitely too low for a healthy human. While this suggests that sDMAS results are more easily quantified in functional terms and can more accurately estimate quantities such as blood oxygenation, it is far from conclusive and, as it is only a qualitative result, further research is needed. The reconstructed images still contain artifacts and noise that might be

reduced further using other beamforming methods such as Minimum Variance (MV) beamforming [10], Double stage DMAS [3] or further modifications of DMAS such as the introduction of MV into DMAS [22]. They are however non-linear and computationally expensive. Therefore, they are currently not usable for real-time multispectral applications. However, further study of those methods and appropriate extensions and implementations might give insight into their applicability to multispectral PA imaging. Other issues such as wavelength dependent fluence effects [23], or limited views of PA sensor arrays cannot be solved by a beamforming algorithm alone and will impact functional PA imaging independent of the beamformer.

In conclusion, the presented sDMAS algorithm offers a superior image quality compared to DAS and preserves linearity in the original signal on the same level as DAS, which makes it suitable for spectroscopic PA applications. Furthermore, sDMAS can be performed in real-time and is as such usable in a clinical setting.

Abbreviations

PA	photoacoustic
DAS	Delay and Sum
DMAS	Delay Multiply and Sum
sDMAS	signed DMAS
MV	Minimum Variance
US	ultrasonic
MITK	Medical Imaging Interaction Toolkit
SNR	Signal-to-Noise Ratio
CNR	Contrast-to-Noise Ratio
GUI	Graphical User Interface
API	Application Programming Interface
ITK	Insight Toolkit

References

1. Griffiths, L.; Jim, C. An alternative approach to linearly constrained adaptive beamforming. *IEEE Trans. Antennas Propag.* **1982**, *30*, 27–34. [CrossRef]
2. Kim, J.; Park, S.; Jung, Y.; Chang, S.; Park, J.; Zhang, Y.; Lovell, J.F.; Kim, C. Programmable real-time clinical photoacoustic and ultrasound imaging system. *Sci. Rep.* **2016**, *6*. [CrossRef] [PubMed]
3. Mozaffarzadeh, M.; Mahloojifar, A.; Orooji, M.; Adabi, S.; Nasiriavanaki, M. Double Stage Delay Multiply and Sum Beamforming Algorithm: Application to Linear-Array Photoacoustic Imaging. *IEEE Trans. Biomed. Eng.* **2017**, *65*, 31–42. [CrossRef] [PubMed]
4. Matrone, G.; Savoia, A.S.; Caliano, G.; Magenes, G. The Delay Multiply and Sum Beamforming Algorithm in Ultrasound B-Mode Medical Imaging. *IEEE Trans. Med. Imag.* **2015**, *34*, 940–949. [CrossRef] [PubMed]
5. Park, J.; Jeon, S.; Meng, J.; Song, L.; Lee, J.S.; Kim, C. Delay-multiply-and-sum-based synthetic aperture focusing in photoacoustic microscopy. *J. Biomed. Opt.* **2016**, *21*. [CrossRef] [PubMed]

6. Matrone, G.; Ramalli, A.; Savoia, A.S.; Tortoli, P.; Magenes, G. High Frame-Rate, High Resolution Ultrasound Imaging With Multi-Line Transmission and Filtered-Delay Multiply And Sum Beamforming. *IEEE Trans. Med. Imag.* **2017**, *36*, 478–486. [CrossRef] [PubMed]

7. Alshaya, A.; Harput, S.; Moubark, A.M.; Cowell, D.M.; McLaughlan, J.; Freear, S. Spatial resolution and contrast enhancement in photoacoustic imaging with filter delay multiply and sum beamforming technique. In Proceedings of the 2016 IEEE International Ultrasonics Symposium (IUS), Tours, France, 18–21 September 2016; pp. 1–4.

8. Treeby, B.E.; Zhang, E.Z.; Cox, B.T. Photoacoustic tomography in absorbing acoustic media using time reversal. *Inverse Prob.* **2010**, *26*. [CrossRef]

9. Nolden, M.; Zelzer, S.; Seitel, A.; Wald, D.; Müller, M.; Franz, A.M.; Maleike, D.; Fangerau, M.; Baumhauer, M.; Maier-Hein, L.; et al. The Medical Imaging Interaction Toolkit: Challenges and advances. *Int. J. Comput. Assist. Radiol. Surg.* **2013**, *8*, 607–620. [CrossRef] [PubMed]

10. Holfort, I.K.; Gran, F.; Jensen, J.A. Broadband minimum variance beamforming for ultrasound imaging. *IEEE Trans. Ultrason. Ferroelectr. Freq. Control* **2009**, *56*, 314–325. [CrossRef] [PubMed]

11. Xu, G.; Dar, I.A.; Tao, C.; Liu, X.; Deng, C.X.; Wang, X. Photoacoustic spectrum analysis for microstructure characterization in biological tissue: A feasibility study. *Appl. Phys. Lett.* **2012**, *101*. [CrossRef] [PubMed]

12. Tompson, J.; Schlachter, K. An introduction to the opencl programming model. *Pers. Educ.* **2012**, *49*, 777–780.

13. Harris, F.J. On the use of windows for harmonic analysis with the discrete Fourier transform. *Proc. IEEE* **1978**, *66*, 51–83. [CrossRef]

14. Laser Institute of America. *American National Standard for Safe Use of Lasers*; Laser Institute of America: Orlando, FL, USA, 2007.

15. Kirchner, T.; Sattler, F.; Dinkelacker, S.; Goch, C.J.; Gröhl, J.; Nolden, M.; Maier-Hein, L. MITK/MITK: sDMAS-2018.07. 2018, doi:10.5281/zenodo.1303376. Available online: https://zenodo.org/record/1303376#.W7_9blL3McU (accessed on 11 September 2018).

16. Jacques, S.L. Optical properties of biological tissues: A review. *Phys. Med. Biol.* **2013**, *58*. [CrossRef]

17. Flock, S.T.; Jacques, S.L.; Wilson, B.C.; Star, W.M.; van Gemert, M.J.C. Optical properties of intralipid: A phantom medium for light propagation studies. *Lasers Surg. Med.* **1992**, *12*, 510–519. [CrossRef] [PubMed]

18. Welvaert, M.; Rosseel, Y. On the Definition of Signal-To-Noise Ratio and Contrast-To-Noise Ratio for fMRI Data. *PLoS ONE* **2013**, *8*, 1–10. [CrossRef] [PubMed]

19. Zander, R. The oxygen status of arterial human blood. *Scand. J. Clin. Lab. Investig.* **1990**, *50*, 187–196. [CrossRef]

20. Luke, G.P.; Nam, S.Y.; Emelianov, S.Y. Optical wavelength selection for improved spectroscopic photoacoustic imaging. *Photoacoustics* **2013**, *1*, 36–42. [CrossRef] [PubMed]

21. Lawson, C.L.; Hanson, R.J. *Solving Least Squares Problems*; SIAM: Bangkok, Thailand, 1995.

22. Mozaffarzadeh, M.; Mahloojifar, A.; Orooji, M.; Kratkiewicz, K.; Adabi, S.; Nasiriavanaki, M. Linear-array photoacoustic imaging using minimum variance-based delay multiply and sum adaptive beamforming algorithm. *J. Biomed. Opt.* **2018**, *23*. [CrossRef] [PubMed]

23. Kirchner, T.; Gröhl, J.; Maier-Hein, L. Context encoding enables machine learning-based quantitative photoacoustics. *J. Biomed. Opt.* **2018**, *23*, 056008. [CrossRef] [PubMed]

J2

CONTEXT ENCODING ENABLES MACHINE LEARNING-BASED QUAN-
TITATIVE PHOTOACOUSTICS

This manuscript tackles the optical inverse problem. It is the first work to use machine learning for this, but this is not the central innovation. Rather it presents a way to encode the relevant context information for a reduction in fluence in a descriptor for each voxel. Machine learning – using a simple random forest regressor – was the most suitable way to fit the these descriptors. Besides introducing the method, the manuscript presents a first simulation study.

See Section 3.3.2 for an introduction to the optical inverse problem.

Own contribution

The manuscript was drafted, edited and revised by me, Lena Maier-Hein and Janek Gröhl.

I conceived of the context encoding principle. The machine learning based method was the product of intense discussion with Lena Maier-Hein and Janek Gröhl. The implementation of the algorithm, was the product of a close collaboration between me and Janek Gröhl. The simulation experiments were designed by all the authors and chiefly performed by Janek Gröhl. I performed the post-processing and analysis for the data from the first experiment, Janek Gröhl for the second experiment.

Context encoding enables machine learning-based quantitative photoacoustics

Thomas Kirchner,[a,b,*,†] Janek Gröhl,[a,c,†] and Lena Maier-Hein[a,c,*]
[a]German Cancer Research Center (DKFZ), Division of Computer Assisted Medical Interventions (CAMI), Heidelberg, Germany
[b]Heidelberg University, Faculty of Physics and Astronomy, Heidelberg, Germany
[c]Heidelberg University, Medical Faculty, Heidelberg, Germany

Abstract. Real-time monitoring of functional tissue parameters, such as local blood oxygenation, based on optical imaging could provide groundbreaking advances in the diagnosis and interventional therapy of various diseases. Although photoacoustic (PA) imaging is a modality with great potential to measure optical absorption deep inside tissue, quantification of the measurements remains a major challenge. We introduce the first machine learning-based approach to quantitative PA imaging (qPAI), which relies on learning the fluence in a voxel to deduce the corresponding optical absorption. The method encodes relevant information of the measured signal and the characteristics of the imaging system in voxel-based feature vectors, which allow the generation of thousands of training samples from a single simulated PA image. Comprehensive *in silico* experiments suggest that context encoding-qPAI enables highly accurate and robust quantification of the local fluence and thereby the optical absorption from PA images. © *The Authors. Published by SPIE under a Creative Commons Attribution 3.0 Unported License. Distribution or reproduction of this work in whole or in part requires full attribution of the original publication, including its DOI.* [DOI: 10.1117/1.JBO.23.5.056008]

1 Introduction

Photoacoustic (PA) imaging is an imaging concept with a high potential for real-time monitoring of functional tissue parameters such as blood oxygenation deep inside tissue. It measures the acoustic waves arising from the stress-confined thermal response of optical absorption in tissue.[1] More specifically, a PA signal $S(v)$ in a location v is a pressure response to the locally absorbed energy $H(v)$, which, in turn, is a product of the absorption coefficient $\mu_a(v)$, the Grueneisen coefficient $\Gamma(v)$ and the light fluence $\phi(v)$

$$S(v) \propto H(v) = \mu_a(v) \cdot \Gamma(v) \cdot \phi(v). \qquad (1)$$

Given that the local light fluence not only depends on the imaging setup but is also highly dependent on the optical properties of the surrounding tissue, quantification of optical absorption based on the measured PA signal is a major challenge.[2,3] So far, the field of quantitative PA imaging (qPAI) has focused on model-based iterative optimization approaches to infer optical tissue parameters from measured signals (cf. e.g., Refs. 3–12). Although these methods are well suited for tomographic devices with high image quality (cf. e.g., Refs. 13–15) as used in small animal imaging, translational PA research with clinical ultrasound transducers or similar handheld devices (cf. e.g., Refs. 1 and 16–22) focuses on qualitative image analysis.

As an initial step toward clinical qPAI, we introduce a machine learning-based approach to quantifying PA measurements. The approach features high robustness to noise while being computationally efficient. In contrast to all other approaches proposed to date, our method relies on learning the light fluence on a voxel level to deduce the corresponding optical absorption. Our core contribution is the development of a voxel-based context image (CI) that encodes relevant information of the measured signal voxel together with characteristics of the imaging system in a single feature vector. This enables us to tackle the challenge of fluence estimation as a machine learning problem that we can solve in a fast and robust manner. Comprehensive *in silico* experiments indicate high accuracy, speed, and robustness of the proposed context encoding (CE)-qPAI approach. This is demonstrated for estimation of (1) fluence and optical absorption from PA images, as well as (2) blood oxygen saturation as an example of functional imaging using multispectral PA images.

2 Materials and Methods

A common challenge when applying machine learning methods to biomedical imaging problems is the lack of labeled training data. In the context of PAI, a major issue is the strong dependence of the signal on the surrounding tissue. This renders separation of voxels from their context—as in surface optical imaging[23]—impossible or highly inaccurate. Simulation of a sufficient number of training volumes covering a large range of tissue parameter variations, on the other hand, is computationally not feasible given the generally long runtime of Monte Carlo methods, which are currently the gold standard for the simulation of light transportation in tissue.[11]

Inspired by an approach to shape matching, where the shape context is encoded in a so-called spin image specifically for each node in a mesh,[24] we encode the voxel-specific context in so-called CIs. This allows us to train machine learning algorithms

*Address all correspondence to: Thomas Kirchner, E-mail: t.kirchner@dkfz-heidelberg.de; Lena Maier-Hein, E-mail: l.maier-hein@dkfz-heidelberg.de
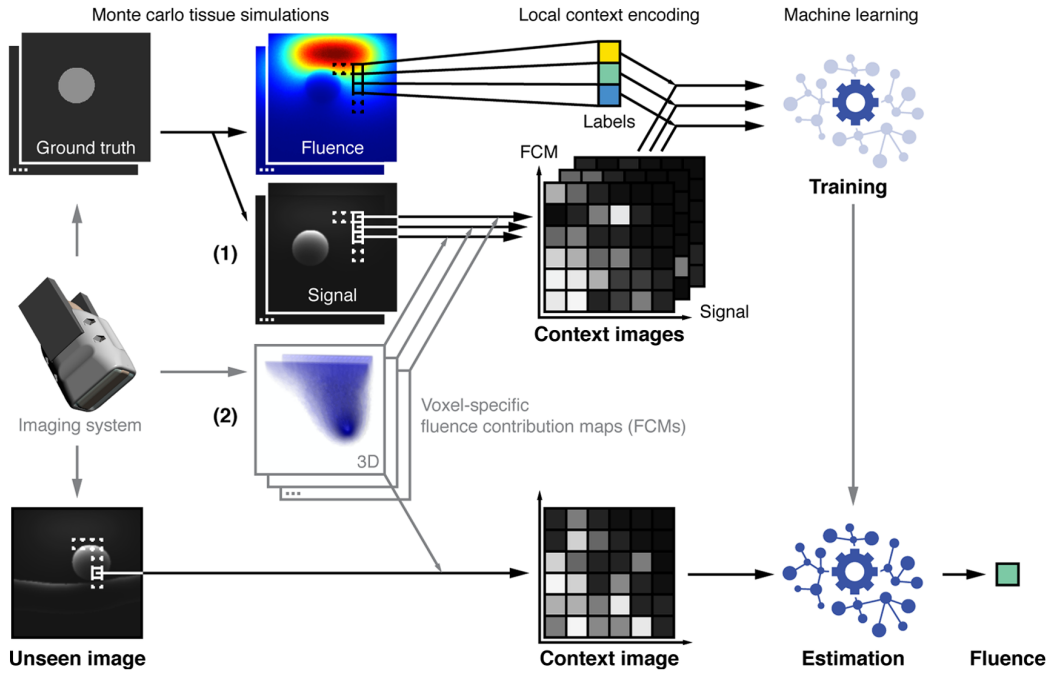
†These authors contributed equally.

54   SIGNAL PROCESSING

Kirchner, Gröhl, and Maier-Hein: Context encoding enables machine learning-based...

Fig. 1 Machine learning approach to fluence estimation with CIs. CIs are generated individually for each voxel and encode both (1) relevant information on the measured signal extracted from the PAI signal volume and (2) prior knowledge on the characteristics of the imaging system represented by FCMs. During algorithm training, a regressor is presented tuples of CIs and corresponding ground truth fluence values for each voxel in the training data. For estimation of optical absorption in voxels of a previously unseen image, the voxel-specific CI is generated and used to infer the local fluence using the trained regressor.

on a voxel level rather than image level and we thus require orders of magnitude fewer simulated training volumes. CIs encode relevant information of the measured signal as well as characteristics of the imaging system represented by so-called voxel-specific fluence contribution maps (FCMs). The CIs serve as a feature vector for said machine learning algorithm, which is trained to estimate fluence in a voxel. The entire quantification method is shown in Fig. 1, which serves as an overview with details given in the following sections.

2.1 Fluence Contribution Map

An important prerequisite for computing the CI for a voxel v is the computation of the corresponding FCM, referred to as FCM$[v]$. FCM$[v](v')$ represents a measure for the likelihood

that a photon arriving in voxel v has passed v'. In other words, an FCM reflects the impact of a PA signal in v' on the drop in fluence in voxel v. An illustration of an FCM corresponding to a typical handheld PA setup is shown in Fig. 2. The FCM$[v]$ is dependent on how the PA excitation light pulse propagates through homogeneous tissue to arrive in v given a chosen hardware setup. The $x \times y$ FCMs per imaging plane are generated once for each new hardware setup and each voxel in the imaging plane.

In this first implementation of the CE-qPAI concept, FCMs are simulated with the same resolution as the input data assuming a background absorption coefficient of 0.1 cm^{-1} and a constant reduced scattering coefficient of 15 cm^{-1}.[25] The number of photons is varied to achieve a consistent photon count in the
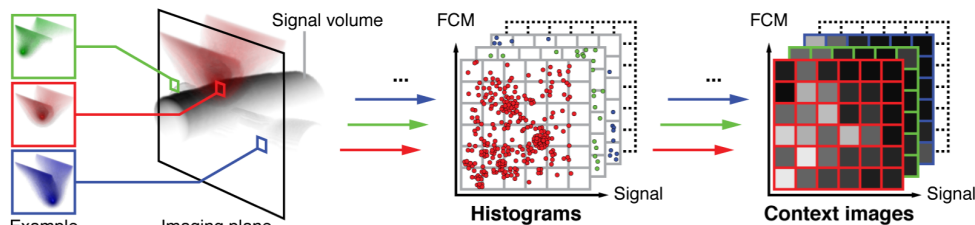
Fig. 2 Generation of CIs for three representative voxels based on their FCMs. The voxel-specific FCMs serve as a representation of how the PA excitation light pulse propagates through homogeneous tissue to arrive in a target voxel given a chosen hardware setup. For each voxel (here: green, red, and blue), tupels of measured signal and corresponding fluence contribution (for that voxel) are determined to generate the voxel-specific histograms from which the CI is generated.

target voxel. The FCMs are generated with the widely used Monte Carlo simulation tool mcxyz.[26] We integrated mcxyz into the open-source Medical Image Interaction Toolkit MITK[27] as mitkMcxyz and modified it to work in a multithreaded environment. Sample FCMs for three different voxels are shown in Fig. 2, which also shows the generation of CIs for those three example voxels.

2.2 Context Image

The CI for a voxel v in a PA volume is essentially a two-dimensional (2-D) histogram composed of (1) the measured PA signal S in the tissue surrounding v and (2) the corresponding $\text{FCM}[v]$. More specifically, it is constructed from the tuples $\{(S(v'), \text{FCM}[v](v')) | v' \in N(v)\}$ where $N(v)$ is defined as $N(v) = \{v' | \text{FCM}[v](v') > \epsilon\}$. This constraint is set to exclude voxels with a negligible contribution to the fluence in v. The tuples are arranged by magnitude of $S(v')$ and $\text{FCM}[v](v')$ into a 2-D histogram and thereby encode the relevant context information in a compact form. In our prototype implementation of the CE-qPAI concept, the fluence contribution and signal axes of the histogram are discretized in 12 bins and scaled logarithmically to better represent the predominantly low signal and fluence contribution components. The ranges of the axes are set as $0 < \log(S) < \log(255)$ and $\log(\epsilon) < \log(\text{FCM}) < -1$. Signals and fluence contributions larger than the upper boundary are included in the highest bin, whereas smaller signals and fluence contributions are not. Figure 2 shows the generation of CIs from FCMs and PA signals. Labeled CIs are used for training a regressor that can later estimate fluence, which, in turn, is used to reconstruct absorption [Eq. (1)].

2.3 Machine Learning-Based Regression for Fluence Estimation

During the training phase, a regressor is presented tuples $[\text{CI}(v), \phi(v)]$ of $\text{CI}(v)$ and corresponding ground truth fluence values $\phi(v)$ for each voxel v in a set of PAI volumes. For estimation of optical absorption in a voxel v_u of a previously unseen image, the voxel-specific CI is generated and used to infer fluence $\hat{\phi}(v_u)$ using the trained algorithm.

In our prototype implementation of the CE-qPAI method, we use a random forest regressor. A random forest regressor is an ensemble of decision trees, where the weighted vote of the individual trees is used as the estimation.[28] To train the random forest, all labeled CIs of the respective training set need to be evaluated at once. With voxel-based CIs, thousands of training samples can be extracted from a single slice of a simulated PA training volume. Ground truth training data generation is performed using a dedicated software plugin integrated into MITK and simulating the fluence with mitkMcxyz. It should be noted that the simulated images consist mainly of background voxels and not of vessel structures, which are our regions of interest (ROI). This leads to an imbalance in the training set. To avoid poor estimation for underrepresented classes,[29] we undersample background voxels in the training process to ensure a 1:1 ROI/background sample ratio. The parameters of the random forest are set to the defaults of sklearn 0.18 using python 2.7, except for the tree count which was set to $n_{\text{regressors}} = 100$. CIs are used as feature vectors and labeled with the optical property to be estimated (e.g., fluence or oxygenation). The parameters were chosen based on a grid search on a separate dataset not used in the experiments of this work.

2.4 Hardware Setup

We assume a typical linear probe hardware setup,[30] where the ultrasound detector array and the light source move together and the illumination geometry is the same for each image recorded. This is also the case for other typical tomographic devices.[31,32] All simulations were performed on high-end CPUs (Intel i7-5960X).

3 Experiments and Results

In the following validation experiments, we quantify the fluence up to an imaging depth of 28 mm in unseen test images for each dataset. With our implementation and setup, all images comprise 3008 training samples, which results in an average simulation time of about 50 ms per training sample. This allows us to generate enough training samples in a feasible amount of time, to train a regressor that enables fluence estimation in a previously unseen image in near real time. The measured computational time for quantifying fluence in a single 64×47 voxel image slice is $0.9 \text{ s} \pm 0.1 \text{ s}$.

In the following, we present the experimental design and results of the validation of CE-qPAI. First, we will validate the estimation of absorption from PAI volumes acquired at a fixed wavelength and then estimate blood oxygenation from multispectral PAI volumes.

3.1 Monospectral Absorption Estimation

3.1.1 Experiment

To assess the performance of CE-qPAI in PA images of blood vessels, we designed six experimental datasets (DS) with varying complexities as listed in Table 1. With the exception of DS_{multi}, each of the six experimental DS is composed of 150 training items, 25 validation items, and 25 test items, where each item comprises a three-dimensional (3-D) simulated PA image of dimensions $64 \times 47 \times 62$ and 0.6-mm equal spacing as well as a corresponding (ground truth) fluence map.

As labels of the generated CIs, we used a fluence correction $\phi_c(v') = \phi(v')/\phi_h(v')$, where $\phi_h(v')$ is a fluence simulation based on a homogeneous background tissue assumption. We used five equidistant slices out of each volume, resulting in a generation of a total of 2,256,000; 376,000 and 376,000 CIs for each dataset—for training, parameter optimization, and

Table 1 The design parameters of the DS. All ranges denote sampling from uniform distributions within the given bounds.

Dataset	Vessel radius [mm]	Vessel absorption μ_a [cm^{-1}]	Vessel count	Background absorption μ_a [cm^{-1}]
DS$_{\text{base}}$	3	4.7	1	0.1
DS$_{\text{radius}}$	**0.5 to 6**	4.7	1	0.1
DS$_{\text{absorb}}$	3	**1 to 12**	1	0.1
DS$_{\text{vessel}}$	3	4.7	**1 to 7**	0.1
DS$_{\text{background}}$	3	4.7	1	**10^{-4} to 0.2**
DS$_{\text{multi}}$	0.5 to 6	1 to 12	1 to 7	10^{-4} to 0.2

56   SIGNAL PROCESSING

Kirchner, Gröhl, and Maier-Hein: Context encoding enables machine learning-based...

testing, respectively. To account for the high complexity of DS_{multi}, we increased the number of training volumes for that set from 150 to 400. The baseline dataset DS_{base} represents simulations of a transcutaneously scanned simplified model of a blood vessel of constant radius (3 mm) and constant absorption (vessel: 4.73 cm^{-1}, background: 0.1 cm^{-1}) and reduced scattering coefficient (15 cm^{-1}). To approximate partial volume effects, the absorption coefficients in the ground truth images were Gaussian blurred with a sigma of 0.6 mm. Single slices were simulated using 2×10^6 photons for all training sets and 10^8 photons for the respective test and validation sets and then compounded in a fully scanned volume. Different shapes and poses of the vessel were generated by a random walk with steps r defined as

$$r_i = r_{i-1} + \eta \cdot a, \tag{2}$$

where η is a free parameter constant in each vessel with an inter-vessel variation within a uniform distribution $(0 < \eta < 0.2)$ and a is varied for each of its components in each step within a uniform distribution $(-0.2 \text{ mm} < a_i < 0.2 \text{ mm})$. To investigate how variations in geometry and optical properties impact the performance of our method, we designed further experimental DS in which the number of vessels (DS_{vessel}), the radii of the vessels (DS_{radius}), the optical absorption coefficients within the vessels (DS_{absorb}), the absorption coefficient of the background ($DS_{background}$), as well as all of the above (DS_{multi}) were varied. We tested the robustness of CE-qPAI to this range of scenarios without retuning CI or random forest parameters.

Although most studies assess the performance of a method in the entire image (cf. e.g., Refs. 6, 33, and 34), it must be pointed out that the accuracy of signal quantification is often most relevant in a defined region of interest—such as in vessels or regions that provide a meaningful PA signal. These are typically also the regions, where quantification is particularly challenging due to the strongest signals originating from boundaries with discontinuous tissue properties. To address this important aspect we validated our method, not only on the entire image, but also in the ROI, which we define for our DS as voxels representing a vessel and at the same time having a contrast-to-noise ratio (CNR) of larger than 2, to only include significant signal in the ROI. We define CNR following Walvaert and Rosseel[35] in a voxel v as

$$\text{CNR} = \frac{S(v) - \text{avg}(b)}{\text{std}(b)}, \tag{3}$$

where the avg(b) and std(b) are the average and standard deviations of the background signal b over a simulated image slice with a background absorption coefficient of 0.1 cm^{-1} and no other structures. Using such an image without application of a noise model, we simulated an intrinsic background noise of (4.2 ± 2.8) a.u.

To investigate the robustness of CE-qPAI to noise, we added the following noise models to each dataset. The noise models consist of an additive Gaussian noise term applied on the signal volumes followed by a multiplicative white Gaussian noise term, similar to noise assumptions used in prior work.[6,33] We examined three noise levels to compare against the simulation-intrinsic noise case:

1. 2% multiplicative and (0.125 ± 0.125) a.u. additive component

2. 10% multiplicative and (0.625 ± 0.625) a.u. additive component

3. 20% multiplicative and (1.25 ± 1.25) a.u. additive component

The additive and multiplicative noise components follow an estimation of noise components on a custom PA system.[30] For each experimental dataset introduced in Table 1 and each noise set, we applied the following validation procedure separately. Following common research practice, we used the training data subset for training of the random forest and the validation data subset to ensure the convergence of the training process, as well as to set suitable parameters for the random forest and ROI, whereas we only evaluated the test data subset to report the final results (as described in Ref. 36). As an error metric, we report the relative fluence estimation error e_r

$$e_r(v) = \frac{|\hat{\phi}(v) - \phi(v)|}{\phi(v)}, \tag{4}$$

rather than an absorption estimation error, to separate the error in estimating fluence with CE-qPAI from errors introduced through simulation-intrinsic or added noise on the signal, which will affect the quantification regardless of fluence estimation.

3.1.2 Results

Figures 3(a)–3(c) show representative examples of the previously unseen 125 simulated test images from the baseline dataset DS_{base}, with their corresponding fluence estimation results. The optical absorption is reconstructed using the fluence estimation. A histogram illustrating absorption estimation accuracy in ROI voxels of DS_{base} is shown in Fig. 3(d) and compared with a static fluence correction approach.

Table 2 summarizes the descriptive statistics of the relative fluence estimation errors e_r for the experiments on absorption estimation using single wavelength PA images. The relative fluence estimation error e_r does not follow a normal distribution due to large outliers especially in complex DS, which is why we report median e_r with interquartile ranges (IQR) for all DS. Even for the most complex dataset DS_{multi} with variations of multiple parameters, CE-qPAI yields a median overall relative fluence estimation error e_r below 4%. Errors are higher in the ROI, especially in DS with high variations of absorption.

Previously proposed qPAI approaches reveal high drops in estimation performance when dealing with noisy data (cf. e.g., Ref. 37). To remedy this, methods have been proposed to incorporate more accurate noise representations into model-based reconstruction algorithms.[33,38] When validating the robustness of CE-qPAI to noise, it yields high accuracy even under unrealistically high noise levels of up to 20% (cf. Fig. 4). Regardless of the noise level applied, the highest median errors occur in the ROIs of DS that are characterized by high absorption and inhomogeneous tissue properties.

3.2 Multispectral Blood Oxygenation Estimation

The concept of CE cannot only be used to estimate fluence and absorption, but also derived functional parameters such as

Kirchner, Gröhl, and Maier-Hein: Context encoding enables machine learning-based...
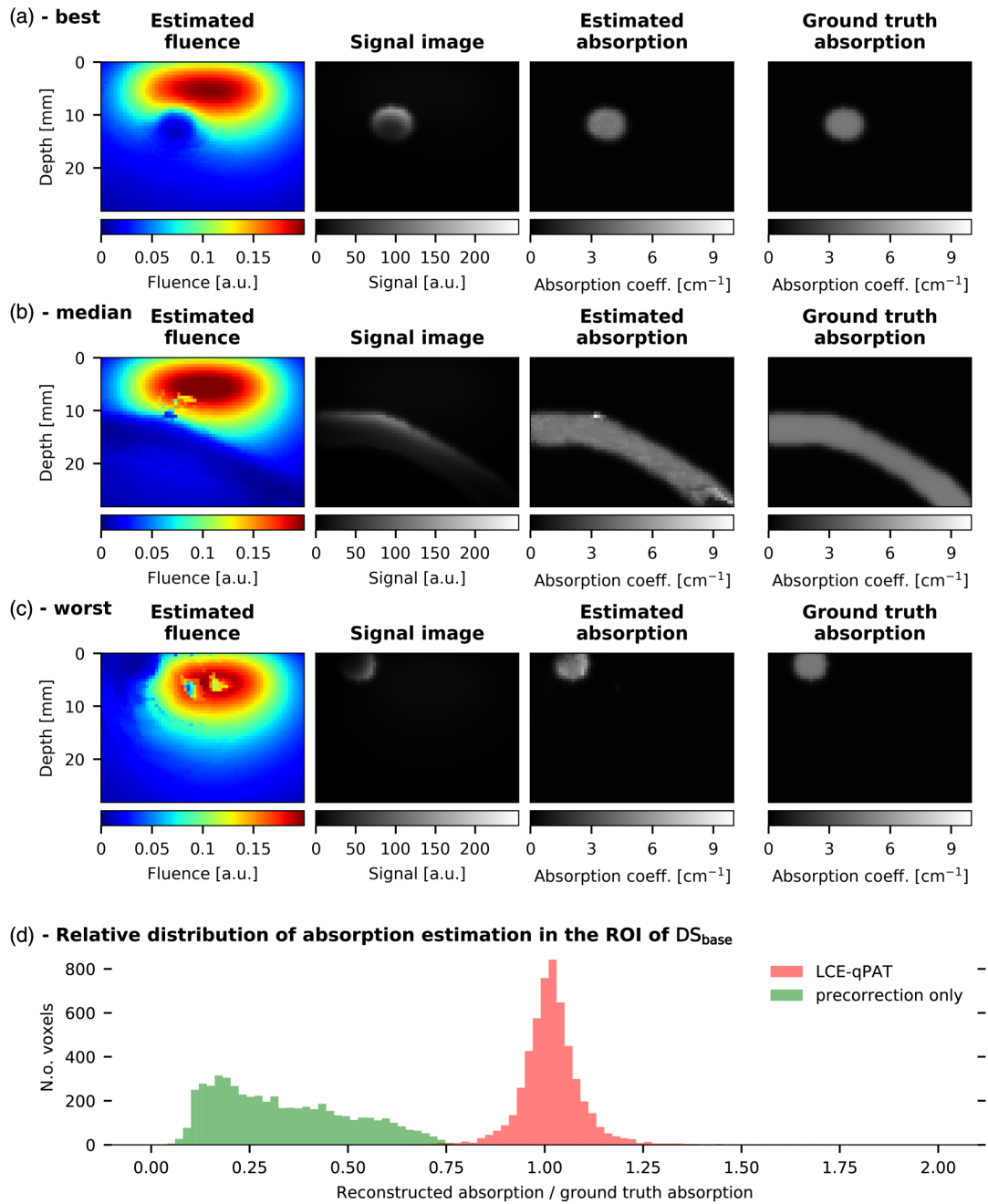
Fig. 3 Absorption reconstruction results after fluence estimation. For the slices with the (a) lowest, (b) median, and (c) highest median fluence estimation error e_r within the ROI of DS_{base}. We show (from left to right) the estimated fluence, the corresponding signal images, the resulting estimation of the absorption coefficient, and the ground truth optical absorption, for reference. (d) A histogram of the relative absorption estimation over all ROI voxels ($n = 5347$) in DS_{base} illustrating absorption estimation accuracy rather than fluence estimation accuracy measured by e_r. Precorrecting the signal with the fluence of a homogeneous tissue assumption underestimates the absorption and is considerably outperformed by CE-qPAI in the ROI. The CE-qPAI plot omits 5 outliers larger 2.

blood oxygenation. To this end, the estimated absorption in a voxel for multiple wavelengths can be applied to resolve oxygenation via linear spectral unmixing. Alternatively, a regressor can be trained using the CIs labeled with ground truth oxygenation.

3.2.1 Experiment

To investigate the performance of CE-qPAI for blood oxygenation (sO_2) estimation, we designed an additional multispectral simulated dataset DS_{oxy} using the wavelengths 750, 800, and 850 nm. It consists of 240 multispectral training volumes and

Kirchner, Gröhl, and Maier-Hein: Context encoding enables machine learning-based...

Table 2 Descriptive statistics of fluence estimation results. The median and IQR of the relative fluence estimation error e_r for the six validation DS used for the single wavelength experiments. The median error and IQR are provided (1) for all voxels in the respective test set as well as (2) for the voxels in the ROI only.

	Relative error e_r			
	All voxels		ROI	
Dataset	Median (%)	IQR (%)	Median (%)	IQR (%)
DS_{base}	1.0	(0.5, 1.9)	4.2	(1.9, 7.6)
DS_{radius}	1.4	(0.6, 3.3)	5.7	(2.4, 11.3)
DS_{absorb}	1.2	(0.5, 2.8)	14.7	(5.4, 32.2)
DS_{vessel}	1.8	(0.7, 6.2)	6.8	(3.0, 13.2)
$DS_{background}$	0.7	(0.3, 1.4)	4.1	(1.7, 7.3)
DS_{multi}	2.3	(0.7, 38.5)	15.7	(6.6, 40.0)

11 multispectral test volumes, each featuring homogeneous oxygenation and one vessel with a radius of 2.3 to 4 mm—modeled after a carotid artery.[39] For each image slice and at each wavelength, 10^7 photons were used for simulation. Oxygenation values for the training images were drawn randomly from a uniform sO_2 distribution $U(0\%, 100\%)$. For testing, we simulated 11 multispectral volumes at three wavelengths and 11 blood oxygenation levels ($sO_2 \in \{0\%, 10\%, 20\%, \ldots, 100\%\}$). The optical absorption was adjusted by wavelength and oxygenation, as described by Jacques.[25] Hemoglobin concentration was assumed to be 150 g/L.[25] The blood volume fraction was set to 0.5% in the background tissue and to 100% in the blood vessels. The reduced scattering coefficient was again set to 15 cm^{-1}. We estimated the oxygenation using three methods:

1. *Linear spectral unmixing on the signal images as a baseline.*[40] For this, we applied a non-negative constrained least squares approach as also used in Ref. 15 that minimizes $\|Ax - \mathbf{b}\| = 0$, where A is the matrix containing the reference spectra, $\mathbf{b}$ is the measurement vector, and x is the unmixing result.

Specifically, we used the python scipy.optimize.minimize function with the sequential least squares programming method and added a non-negativity inequality constraint. We evaluated the unmixing results of this method on all voxels in the ROI as well as exclusively on those voxels with the maximum intensity projection (MIP) along image x-axis at wavelength 800 nm to account for nonlinear fluence effects deep inside the vessels.

2. *Linear spectral unmixing of the signal after quantification of the three input images with CE-qPAI.* After correcting the raw signal images for nonlinear fluence effects using CE-qPAI, we applied the same method as described in (1) and evaluated on the same voxels that were used in (1) to ensure comparability of the results.

3. *Direct estimation of oxygenation using a functional adaptation of CE-qPAI.* For functional CE-qPAI (fCE-qPAI), triples of CIs for the three chosen wavelengths were concatenated into one feature vector and labeled with the ground truth oxygenation.

3.2.2 Results

Estimation of local blood oxygen saturation (sO_2) is one of the main qPAI applications and is only possible with multispectral measurements. As such, the presented approaches were validated together with the baseline method on the dataset DS_{oxy}. As shown in Fig. 5(a), the estimation results for both methods are in very close agreement with the ground truth. In fact, the median absolute oxygen estimation error was 3.1% with IQR (1.1% and 6.4%) for CE-qPAI and 0.8% with IQR (0.3% and 1.8%) for the fCE-qPAI adaptation. Furthermore, our methodology outperforms a baseline approach based on linear spectral unmixing of the raw signal (as also compared to in Ref. 15). By means of example Fig. 5(b) shows that the linear spectral unmixing of the ROI on the uncorrected signal fails deep inside the ROI, where the fluence varies strongly for different wavelengths. To compensate for this effect when comparing the approach to our method, we validate all methods only on the MIP along the depth axis (as also used in Ref. 41) in Fig. 5(a).
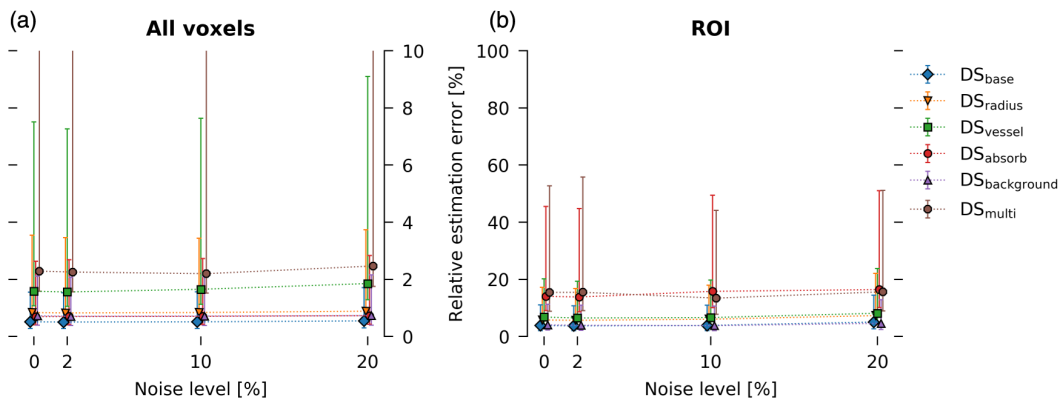

Fig. 4 Robustness of the fluence estimation against noise. Median relative fluence estimation errors e_r with IQR over all DS for, (a) all test voxels, and (b) in region of interest test voxels. The whiskers in this plot show the first and third quartile.
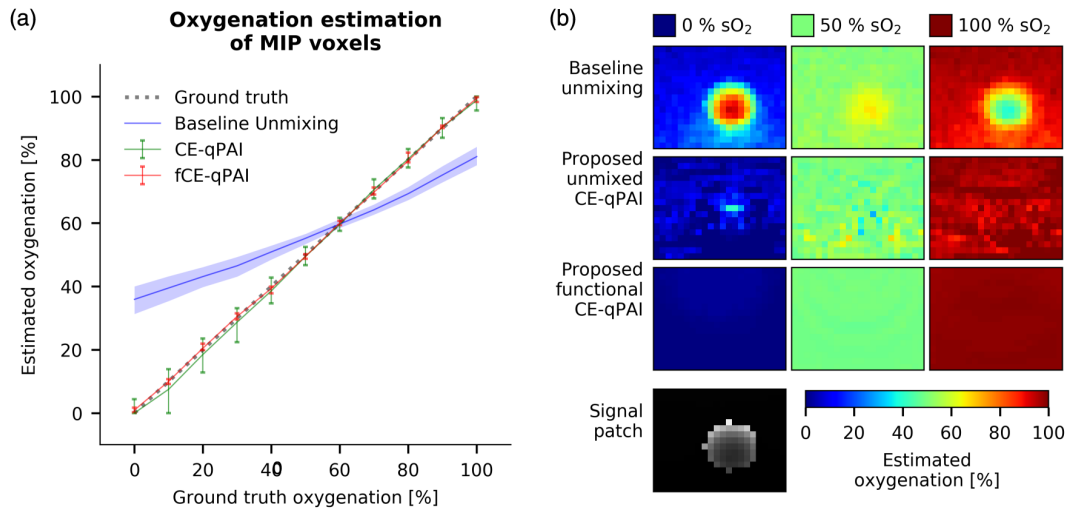
Fig. 5 Oxygenation estimation. (a) The median oxygen estimation with the IQR on the MIP voxels using linear spectral unmixing of (blue) the uncorrected signal, (green) the signal corrected by CE-qPAI, and (red) direct estimation by functional CE-qPAI (fCE-qPAI). (b) The oxygenation estimation for a representative patch of signal showing a vessel in 15-mm depth and with 3-mm radius. The signal for one of the measurement wavelengths is shown for reference together with the oxygen estimation results for 0%, 50%, and 100% ground truth homogeneous oxygenation and the three examined methods.

4 Discussion

This paper addresses one of the most important challenges related to PA imaging, namely the quantification of optical absorption based on the measured signal. In contrast to all other approaches proposed to qPAI to date (cf. e.g., Refs. 3–12), our method relies on learning the light fluence in a voxel to deduce the corresponding optical absorption. Comprehensive *in silico* experiments presented in this manuscript show the high potential of this approach to estimate optical absorption as well as derived functional properties, such as oxygenation, even in the presence of high noise.

Although machine learning methods have recently been applied to PAI related problems (cf. e.g., Refs. 42–44), these have mainly focused on image reconstruction but not signal quantification. We attribute this to the fact that *in vivo* training data generation for machine learning-based qPAI is not at all straightforward given the lack of reference methods for estimating optical absorption in depth. Despite recent developments related to hybrid diffusion approximation and Monte Carlo methods,[45] fast generation of *in silico* training data also remains an unsolved challenge. Note in this context that commonly applied methods of data augmentation (i.e., methods that may be used to automatically enlarge training data sets as discussed in Ref. 46) cannot be applied to PA images due to the interdependence of fluence and signal. With our contribution, we have addressed the challenge by introducing the concept of CIs, which allow us to generate one training case from each voxel rather than from each image.

As an important contribution with high potential impact, we adapted CE-qPAI to estimate functional tissue properties from multiwavelength data. Both variants—linear spectral unmixing of the fluence corrected signal, as well as direct estimation of oxygenation from multi wavelength CIs, yielded accurate results that outperformed a baseline approach based on linear spectral unmixing of the raw PA signal. It should be noted that linear spectral unmixing of the signal for sO$_2$ estimation is usually performed on a wider range of wavelengths to increase accuracy. However, even this increase in the number of wavelengths cannot fully account for nonlinear fluence effects.[3] Combined with the separately established robustness to noise, multiwavelength applications of CE-qPAI are very promising.

In our first prototype implementation of CE-qPAI, we used random forests regressors with standard parameters. It should be noted, however, that fluence estimation from the proposed CI can in principle be performed by any other machine learning method in a straightforward manner. Initial experiments suggest that even better performance can be achieved with convolutional neural networks.[47]

By relating the measured signals $S(v')$ in the neighborhood of v to the corresponding fluence contributions $FCM[v](v')$ we relate the absorbed energy in v', to the fluence contribution of v' to v. In this context, it has to be noted that the fluence contribution $FCM[v](v')$ is only an approximation of the true likelihood that a photon passing v has previously passed v', because $FCM[v]$ is generated independently of the scene under observation assuming constant background absorption and scattering. Nevertheless due to the generally low variance of scattering in tissue, it serves as a reliable input for the proposed machine learning-based quantification.

A limitation of our study can be seen in the fact that we performed the validation *in silico*. To apply CE-qPAI *in vivo*, further research will have to be conducted in two main areas. First, we are working on accurately solving the acoustical inverse problem for specific scanners.[48] The method will be integrated into the quantification algorithm to enable quantification of images acquired with common PAI probes such as clinical linear transducers. Second, training data have to be generated as close to reality as possible—considering, for example, imaging artifacts.

In contrast to prior work (cf. e.g., Refs. 6, 7, 33, 49, and 34), our initial validation handles the whole range of near infrared absorption in whole blood at physiological hemoglobin concentrations and demonstrates high robustness to noise. The impact

60   SIGNAL PROCESSING

Kirchner, Gröhl, and Maier-Hein: Context encoding enables machine learning-based...

of variations of scattering still needs investigation although these should be small in the near infrared.

Long-term goal of our work is the transfer of CE-qPAI to clinical data. In this context, run-time of the algorithm will play an important role. Although our current implementation can estimate absorption on single slices within a second, this might not be sufficient for interventional clinical estimation of whole tissue volumes and at higher resolutions. An efficient GPU implementation of the time intensive CI generation should enable real-time quantification.

In summary, CE-qPAI is the first machine learning-based approach to quantification of PA signals. The results of this work suggest that quantitative real-time functional PA imaging deep inside tissue is feasible.

Code and Data Availability

The code for the method as well as the experiments was written in C++ and python 2.7 and is partially open source and available at https://phabricator.mitk.org/source/mitk.git. Additional code and all raw and processed data generated in this work are available from the corresponding authors on reasonable request.

References

1. L. V. Wang and J. Yao, "A practical guide to photoacoustic tomography in the life sciences," *Nat. Methods* **13**(8), 627–638 (2016).
2. L. V. Wang and S. Hu, "Photoacoustic tomography: in vivo imaging from organelles to organs," *Science* **335**(6075), 1458–1462 (2012).
3. B. T. Cox, J. G. Laufer, and P. C. Beard, "The challenges for quantitative photoacoustic imaging," *Proc. SPIE* **7177**, 717713 (2009).
4. N. Iftimia and H. Jiang, "Quantitative optical image reconstruction of turbid media by use of direct-current measurements," *Appl. Opt.* **39**(28), 5256–5261 (2000).
5. B. T. Cox et al., "Quantitative photoacoustic imaging: fitting a model of light transport to the initial pressure distribution," *Proc. SPIE* **5697**, 49–55 (2005).
6. B. T. Cox et al., "Two-dimensional quantitative photoacoustic image reconstruction of absorption distributions in scattering media by use of a simple iterative method," *Appl. Opt.* **45**(8), 1866–1875 (2006).
7. Z. Yuan and H. Jiang, "Quantitative photoacoustic tomography: recovery of optical absorption coefficient maps of heterogeneous media," *Appl. Phys. Lett.* **88**(23), 231101 (2006).
8. J. Laufer et al., "Quantitative spatially resolved measurement of tissue chromophore concentrations using photoacoustic spectroscopy: application to the measurement of blood oxygenation and haemoglobin concentration," *Phys. Med. Biol.* **52**(1), 141–168 (2007).
9. E. Malone, B. Cox, and S. Arridge, "Multispectral reconstruction methods for quantitative photoacoustic tomography," *Proc. SPIE* **9708**, 970827 (2016).
10. M. Haltmeier, L. Neumann, and S. Rabanser, "Single-stage reconstruction algorithm for quantitative photoacoustic tomography," *Inverse Probl.* **31**(6), 065005 (2015).
11. B. Cox et al., "Quantitative spectroscopic photoacoustic imaging: a review," *J. Biomed. Opt.* **17**(6), 061202 (2012).
12. B. Banerjee et al., "Quantitative photoacoustic tomography from boundary pressure measurements: noniterative recovery of optical absorption coefficient from the reconstructed absorbed energy map," *J. Opt. Soc. Am. A* **25**(9), 2347–2356 (2008).
13. L. V. Wang, "Multiscale photoacoustic microscopy and computed tomography," *Nat. Photonics* **3**(9), 503–509 (2009).
14. J. Xia and L. V. Wang, "Small-animal whole-body photoacoustic tomography: a review," *IEEE Trans. Biomed. Eng.* **61**(5), 1380–1389 (2014).
15. S. Tzoumas et al., "Eigenspectra optoacoustic tomography achieves quantitative blood oxygenation imaging deep in tissues," *Nat. Commun.* **7**, 12121 (2016).
16. J. J. Niederhauser et al., "Combined ultrasound and optoacoustic system for real-time high-contrast vascular imaging in vivo," *IEEE Trans. Med. Imaging* **24**(4), 436–440 (2005).
17. S. Zackrisson, S. M. W. Y. van de Ven, and S. S. Gambhir, "Light in and sound out: emerging translational strategies for photoacoustic imaging," *Cancer Res.* **74**(4), 979–1004 (2014).
18. P. K. Upputuri and M. Pramanik, "Recent advances toward preclinical and clinical translation of photoacoustic tomography: a review," *J. Biomed. Opt.* **22**(4), 041006 (2017).
19. J. Gamelin et al., "Curved array photoacoustic tomographic system for small animal imaging," *J. Biomed. Opt.* **13**(2), 024007 (2008).
20. K. H. Song et al., "Noninvasive photoacoustic identification of sentinel lymph nodes containing methylene blue in vivo in a rat model," *J. Biomed. Opt.* **13**(5), 054033 (2008).
21. C. Kim et al., "Handheld array-based photoacoustic probe for guiding needle biopsy of sentinel lymph nodes," *J. Biomed. Opt.* **15**(4), 046010 (2010).
22. A. Garcia-Uribe et al., "Dual-modality photoacoustic and ultrasound imaging system for noninvasive sentinel lymph node detection in patients with breast cancer," *Sci. Rep.* **5**, 15748 (2015).
23. S. J. Wirkert et al., "Robust near real-time estimation of physiological parameters from megapixel multispectral images with inverse Monte Carlo and random forest regression," *Int. J. Comput. Assist. Radiol. Surg.* **11**(6), 909–917 (2016).
24. A. E. Johnson and M. Hebert, "Using spin images for efficient object recognition in cluttered 3D scenes," *IEEE Trans. Pattern Anal. Mach. Intell.* **21**(5), 433–449 (1999).
25. S. L. Jacques, "Optical properties of biological tissues: a review," *Phys. Med. Biol.* **58**(11), R37–R61 (2013).
26. S. L. Jacques, "Coupling 3D Monte Carlo light transport in optically heterogeneous tissues to photoacoustic signal generation," *Photoacoustics* **2**(4), 137–142 (2014).
27. I. Wolf et al., "The medical imaging interaction toolkit," *Med. Image Anal.* **9**(6), 594–604 (2005).
28. L. Breiman, "Random forests," *Mach. Learn.* **45**(1), 5–32 (2001).
29. A. Estabrooks, T. Jo, and N. Japkowicz, "A multiple resampling method for learning from imbalanced data sets," *Comput. Intell.* **20**(1), 18–36 (2004).
30. T. Kirchner et al., "Freehand photoacoustic tomography for 3D angiography using local gradient information," *Proc. SPIE* **9708**, 97083G (2016).
31. V. Neuschmelting et al., "Performance of a multispectral optoacoustic tomography (MSOT) system equipped with 2D vs. 3D handheld probes for potential clinical translation," *Photoacoustics* **4**(1), 1–10 (2016).
32. A. Needles et al., "Development and initial application of a fully integrated photoacoustic micro-ultrasound system," *IEEE Trans. Ultrason. Ferroelectr. Freq. Control* **60**(5), 888–897 (2013).
33. T. Tarvainen et al., "Bayesian image reconstruction in quantitative photoacoustic tomography," *IEEE Trans. Med. Imaging* **32**(12), 2287–2298 (2013).
34. R. J. Zemp, "Quantitative photoacoustic tomography with multiple optical sources," *Appl. Opt.* **49**(18), 3566–3572 (2010).
35. M. Welvaert and Y. Rosseel, "On the definition of signal-to-noise ratio and contrast-to-noise ratio for FMRI data," *PLoS One* **8**(11), e77089 (2013).
36. B. D. Ripley, *Pattern Recognition and Neural Networks*, Cambridge University Press, Cambridge (2007).

Kirchner, Gröhl, and Maier-Hein: Context encoding enables machine learning-based...

37. E. Beretta et al., "A variational method for quantitative photoacoustic tomography with piecewise constant coefficients," Chapter 6 in *Variational Methods*, M. Bergounioux et al., Eds., pp. 202–224, Walter de Gruyter (2016).

38. T. Tarvainen et al., "Image reconstruction with noise and error modelling in quantitative photoacoustic tomography," *Proc. SPIE* **9708**, 97083Q (2016).

39. J. Krejza et al., "Carotid artery diameter in men and women and the relation to body and neck size," *Stroke* **37**(4), 1103–1105 (2006).

40. N. Keshava and J. F. Mustard, "Spectral unmixing," *IEEE Signal Process. Mag.* **19**(1), 44–57 (2002).

41. X. L. Deán-Ben, E. Bay, and D. Razansky, "Functional optoacoustic imaging of moving objects using microsecond-delay acquisition of multispectral three-dimensional tomographic data," *Sci. Rep.* **4**, 5878 (2014).

42. A. Reiter and M. A. L. Bell, "A machine learning approach to identifying point source locations in photoacoustic data," *Proc. SPIE* **10064**, 100643J (2017).

43. A. Hauptmann et al., "Model based learning for accelerated, limited-view 3D photoacoustic tomography," arXiv:1708.09832v1 (2017).

44. S. Antholzer, M. Haltmeier, and J. Schwab, "Deep learning for photoacoustic tomography from sparse data," arXiv:1704.04587v2 (2017).

45. C. Zhu and Q. Liu, "Hybrid method for fast Monte Carlo simulation of diffuse reflectance from a multilayered tissue model with tumor-like heterogeneities," *J. Biomed. Opt.* **17**(1), 010501 (2012).

46. A. Dosovitskiy et al., "Discriminative unsupervised feature learning with convolutional neural networks," in *Advances in Neural Information Processing Systems*, Vol. 27, pp. 766–774 (2014).

47. K. He et al., "Deep residual learning for image recognition," in *IEEE Conf. on Computer Vision and Pattern Recognition (CVPR)* (2016).

48. D. Waibel et al., "Reconstruction of initial pressure from limited view photoacoustic images using deep learning," *Proc. SPIE* **10494**, 104942S (2018).

49. W. Naetar and O. Scherzer, "Quantitative photoacoustic tomography with piecewise constant material parameters," *SIAM J. Imaging Sci.* **7**(3), 1755–1774 (2014).

Thomas Kirchner received his MSc degree in physics from the University of Heidelberg in 2015. He currently works on his PhD at the Division of Computer Assisted Medical Interventions, German Cancer Research Center (DKFZ), where he does research in computational biophotonics, focusing on real-time multispectral photoacoustics and signal quantification.

Janek Gröhl received his MSc degree in medical informatics from the University of Heidelberg and Heilbronn University of Applied Sciences in 2016. He currently works on his PhD at the Division of Computer Assisted Medical Interventions (CAMI), German Cancer Research Center (DKFZ) and does research in software engineering and computational biophotonics focusing on signal quantification in photoacoustic imaging.

Lena Maier-Hein received her PhD from the Karlsruhe Institute of Technology in 2009 and conducted her postdoctoral research in the Division of Medical and Biological Informatics, German Cancer Research Center (DKFZ), and in the Hamlyn Centre for Robotics Surgery, Imperial College London. She is leading the Division of Computer Assisted Medical Interventions (CAMI) at the DKFZ. Currently, she is working on multimodal image processing, surgical data science, and computational biophotonics.

J3

CONFIDENCE ESTIMATION FOR MACHINE LEARNING-BASED QUANTITATIVE PHOTOACOUSTICS

This manuscript addresses the robustness and accuracy of results obtained with qPAI. It presents a method for relative error estimation using a deep learning model and applies this confidence estimate to discard uncertain results in a simulation study.

Own contribution

I am not the main author of this manuscript.

The initial manuscript was drafted by Janek Gröhl and edited and revised by all authors including me.

The concept and methodology was conceived of by Janek Gröhl, me, Tim Adler and Lena Maier-Hein but I had no part in the deep learning methodology. The simulation experiments were designed and discussed by all the authors, and performed by Janek Gröhl.

Journal of
Imaging

MDPI

Article
Confidence Estimation for Machine Learning-Based Quantitative Photoacoustics

Janek Gröhl [1,2,*] (ID)**, Thomas Kirchner** [1,3] (ID)**, Tim Adler** [1] (ID) **and Lena Maier-Hein** [1,2,*] (ID)

[1]   Division of Computer Assisted Medical Interventions (CAMI), German Cancer Research Center (DKFZ), 69120 Heidelberg, Germany; t.kirchner@dkfz-heidelberg.de (T.K.); t.adler@dkfz-heidelberg.de (T.A.)
[2]   Medical Faculty, Heidelberg University, 69120 Heidelberg, Germany
[3]   Faculty of Physics and Astronomy, Heidelberg University, 69120 Heidelberg, Germany
[*]   Correspondence: j.groehl@dkfz-heidelberg.de (J.G.); l.maier-hein@dkfz-heidelberg.de (L.M.-H.)

check for updates

Abstract: In medical applications, the accuracy and robustness of imaging methods are of crucial importance to ensure optimal patient care. While photoacoustic imaging (PAI) is an emerging modality with promising clinical applicability, state-of-the-art approaches to quantitative photoacoustic imaging (qPAI), which aim to solve the ill-posed inverse problem of recovering optical absorption from the measurements obtained, currently cannot comply with these high standards. This can be attributed to the fact that existing methods often rely on several simplifying a priori assumptions of the underlying physical tissue properties or cannot deal with realistic noise levels. In this manuscript, we address this issue with a new method for estimating an indicator of the uncertainty of an estimated optical property. Specifically, our method uses a deep learning model to compute error estimates for optical parameter estimations of a qPAI algorithm. Functional tissue parameters, such as blood oxygen saturation, are usually derived by averaging over entire signal intensity-based regions of interest (ROIs). Therefore, we propose to reduce the systematic error of the ROI samples by additionally discarding those pixels for which our method estimates a high error and thus a low confidence. In silico experiments show an improvement in the accuracy of optical absorption quantification when applying our method to refine the ROI, and it might thus become a valuable tool for increasing the robustness of qPAI methods.

1. Introduction

Photoacoustic imaging (PAI) has been shown to have various medical applications and to potentially benefit patient care [1–3]. It is a non-invasive modality that offers the ability to measure optical tissue properties, especially optical absorption μ_a, both locally resolved and centimeters deep in tissue. Knowledge of these properties allows for deriving functional tissue parameters, such as blood oxygenation SO_2, which is a biomarker for tumors and other diseases [4]. The photoacoustic (PA) signal is a measure of the pressure waves arising from the initial pressure distribution p_0, which depends mainly on μ_a, the Grüneisen coefficient Γ, and the light fluence ϕ, which is shaped by the optical properties of the imaged tissue [5]. Because of this dependence, the measured p_0 is only a qualitative indicator of the underlying μ_a, because even if the initial pressure distribution could be recovered perfectly, estimation of the light fluence is an ill-posed inverse problem that has not conclusively been solved [6].

In order to derive quantitative information from initial pressure p_0 reconstructions of photoacoustic images, one has to account for the light fluence and solve the optical inverse problem. Most methods model the distribution of optical absorption coefficients by iteratively updating the

distribution after computing the solution of a forward model (cf., e.g., [7–14]) with inclusion of the acoustic inverse problem [15,16]. Alternatively, in multispectral photoacoustic imaging applications, the functional parameters are approximated directly by using a variety of spectral unmixing techniques (cf., e.g., [17–19]). Recently, machine learning-based methods for quantitative PAI (qPAI) have been proposed. These encompass end-to-end deep learning on 2D images [20] or the estimation of voxel point estimates with Context Encoding qPAI (CE-qPAI) [21], which incorporates the 3D p_0 context around each voxel into a single feature vector that is used to learn the fluence at that particular voxel. Some of the listed approaches to qPAI have been shown to work in ideal in silico conditions or on specific datasets. At the same time, they have proven difficult to use in clinical applications, which can be attributed to a lack of robustness caused by a priori assumptions that are made regarding, e.g., illumination, probe design, calibration factors, or scattering properties [22]. Developing tools to estimate systematic errors and gain information on the quantification of uncertainties in PAI could thus be of great benefit and could be utilized to improve quantification accuracy.

Uncertainty quantification and compensation is an essential research objective in computer sciences and has been studied extensively in various fields, including image-guided navigation (cf., e.g., [23,24]), multi-modal image registration (cf., e.g., [25,26]), and lesion detection [27]. Current approaches to obtaining confidence intervals for neural network estimates include, e.g., dropout sampling (cf., e.g., [28–31]), probabilistic inference (cf., e.g., [32–34]), sampling from latent variables (cf., e.g., [35–37]), or using ensembles of estimators (cf., e.g., [38,39]). The exploration of such uncertainty quantification methods in the field of PAI, however, has only just started (cf., e.g., [40–43]).

In a recent publication [44], we showed a method for uncertainty quantification for the CE-qPAI method. A key result was that the practice of evaluating PA images over a purely input noise-based (aleatoric) region of interest (ROI) can be improved when also taking into account model-based (epistemic) uncertainty. To achieve this, we combined both sources of uncertainty into a joint uncertainty metric and used this to create an ROI mask on which to compute the statistics. A limitation to that approach could be seen in the fact that we used an uncertainty model specially tailored toward the CE-qPAI method. To overcome this bottleneck, we expand on our prior work in this contribution and present a method that yields confidence estimates by observing the performance of an arbitrary qPAI algorithm and uses the estimates to refine an ROI that was defined based on aleatoric uncertainty.

For validation in the context of qPAI, we applied this methodology to different PA signal quantification algorithms to investigate whether the approach is applicable in a general manner. We hypothesize that an estimated error metric is indicative of the actual absorption quantification error and that we can consequently improve on μ_a estimations by evaluating on an ROI that is further narrowed down with a confidence threshold (*CT*).

2. Materials and Methods

This section gives an overview of the confidence estimation approach, the experiments, and the used dataset and briefly introduces the different qPAI methods that are being used.

Method for Confidence Estimation. Our approach to confidence estimation can be applied to any qPAI method designed to convert an input image I (p_0 or raw time-series data) into an image of optical absorption I_{μ_a}. In order to not restrict the qPAI method to a certain class (e.g., a deep learning-based method), we made the design decision to base the confidence quantification method on an external observing method. For this, we use a neural network, which is presented tuples of input image I and absorption quantification error e_{μ_a} in the training phase. When applying the method to a previously unseen image I, the following steps are performed (cf. Figure 1).
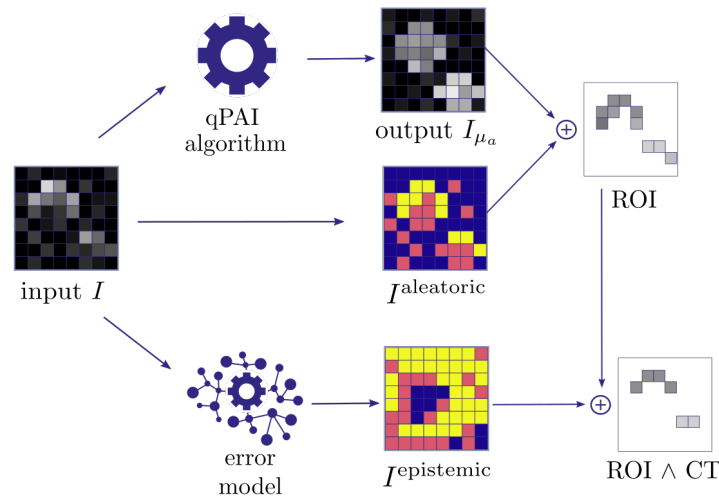
Figure 1. Visualization of the proposed method for confidence estimation using an observing neural network as an error model. The estimator generates an output for a given input and the error model is used to obtain an estimate of the quantification error from the same input data. The region of interest (ROI), which is based on the aleatoric uncertainty $I^{\text{aleatoric}}$ extracted from the input data, can then be refined using the error estimates $I^{\text{epistemic}}$ of the error model as a confidence threshold (*CT*).

1. Quantification of aleatoric uncertainty: I is converted into an image $I^{\text{aleatoric}}$ reflecting the aleatoric uncertainty. For this purpose, we use the contrast-to-noise-ratio (CNR), as defined by Welvaert and Rosseel [45], as $\text{CNR} = (S - \text{avg}(b))/\text{std}(b)$, with S being the pixel signal intensity, and $\text{avg}(b)$ and $\text{std}(b)$ being the mean and standard deviation of all background pixels in the dataset. Using this metric, we predefine our ROI to comprise all pixels with CNR > 5.
2. Quantification of epistemic confidence: I is converted into an image $I^{\text{epistemic}}$ reflecting the epistemic confidence. For this purpose, we use the external model to estimate the quantification error e_{μ_a} of the qPAI algorithm.
3. Output generation: A threshold over $I^{\text{aleatoric}}$ yields a binary image with an ROI representing confident pixels in I_{μ_a} according to the input signal intensity. We then proceed to narrow down the ROI by applying a confidence threshold (*CT*) which removes the n% least confident pixels according to $I^{\text{epistemic}}$.

Deep Learning Model. As our external observing network, we used an adapted version of a standard U-Net [46] implemented in PyTorch [47]. The model uses 2×2 max pooling for downscaling, 2×2 transpose convolutions for upscaling, and all convolution layers have a kernel size of 3×3 and a padding of 1×1. We modified the skip connections to incorporate a total of three convolution layers and thus generate an asymmetric U-Net capable of dealing with different input and output sizes (cf. Figure 2). This is necessary to enable the network to directly output reconstructed initial pressure or optical absorption distributions when receiving raw time-series data as input, as the data have different sizes on the y-axis. Specifically, the second of these convolutions was modified to have a kernel size of 3×20, a stride of 1×20, and a padding of 1×9, effectively scaling down the input along the y-axis by a factor of 20. To be more robust to overfitting, we added dropout layers with a dropout rate of 25% to each convolutional layer of the network. Note that a recent study [48] suggests that the U-net architecture is particularly well-suited for medical imaging applications because of its ability to generate data representations on many abstraction levels.
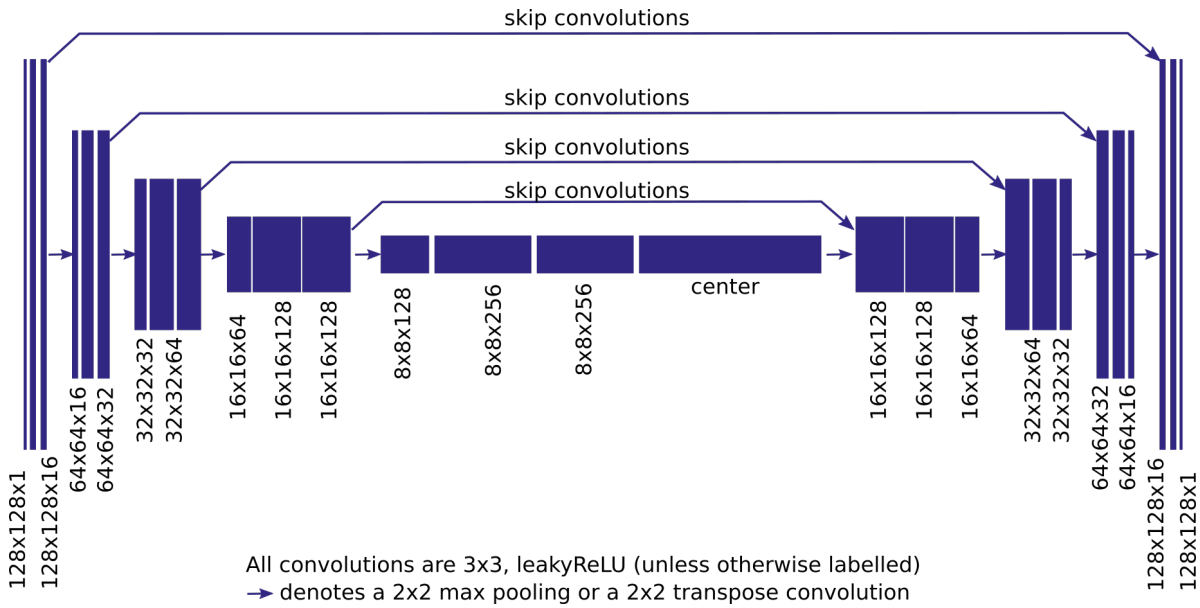
Figure 2. Visualization of the deep learning model used in the experiments: a standard U-Net structure with slight modifications to the skip connections. The (x, y, c) numbers shown represent the x and y dimensions of the layers, as well as the number of channels *c*. Specifically, in this figure, they show the values for a 128×128 input and 128×128 output. The center consists of an additional convolution and a skip convolution layer to enable different input and output sizes.

Quantitative PAI Methods. We applied our approach to confidence estimation to three different qPAI methods; a naïve quantification method, as well as two different deep learning-based approaches (cf. Figure 3). The three methods are detailed in the following paragraphs.

Naïve Fluence Correction: As a naïve quantitative PAI (qPAI) reference method that does not use a deep learning model to reconstruct a quantitative absorption estimate $\hat{\mu}_a$, we performed fluence compensation similar to, e.g., [49,50]. To achieve this, we used a simple Monte Carlo fluence simulation ϕ_h based on the same hardware setup as used in the dataset, without any vascular structures inside the volume but instead with a homogeneous absorption coefficient of 0.1 cm^{-1} and a reduced scattering coefficient of 15 cm^{-1}. To quantify optical absorption with this method, we corrected the simulated p_0 images with ϕ_h by calculating $\hat{\mu}_a = p_0/\phi_h$.

Fluence Correction: Fluence correction refers to a two-stage algorithm, where the initial pressure is corrected by an estimation of the underlying light fluence. The quantification model for this method uses two deep neural networks, N_1 and N_2, with adapted U-Net architectures, as described above (cf. Figure 2). N_1 yields an estimation of the underlying fluence $\hat{\phi}$ from the input data S: $N_1(S) = \hat{\phi}$, and N_2 is used to obtain the initial pressure distribution from the input data $\hat{p}_0$: $N_2(S) = \hat{p}_0$ with the aim of also reducing the noise of S. When using PA raw time-series data as the input, it has to be considered that the decoder and encoder sections of N_2 are asymmetric and the described U-Net adaptation has to be used. The optical absorption coefficients are then estimated from the results of N_1 and N_2 by computing $\hat{\mu}_a = N_2(S)/N_1(S) = \hat{p}_0/\hat{\phi}$ (for a visual representation of the method see Figure 3a).

Direct Absorption Estimation: Recently, a deep learning method for end-to-end estimation of absorption and derived functional parameters from p_0 distributions was proposed [20]. In a similar fashion, we also use a deep learning model N with a modified U-Net architecture (cf. Figure 2) to directly estimate μ_a from the input signal S: $N(S) = \hat{\mu}_a$ (for a visual representation of the method see Figure 3b). This time, μ_a estimation is done without the intermediate step of fluence correction, which might be more sensitive to errors due to error propagation or the presence of artifacts and noise.
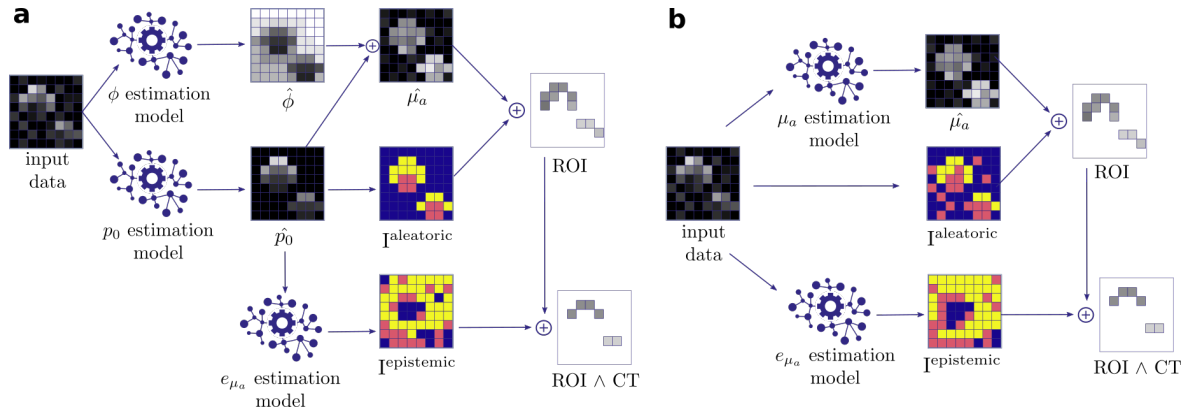
Figure 3. Visualization of the two methods for absorption quantification with subsequent confidence estimation. (**a**) A quantification approach based on fluence estimation. In our implementation, the denoised initial pressure $\hat{p}_0$ and the fluence $\hat{\phi}$ distributions are estimated using deep learning models. These are used to calculate the underlying absorption $\hat{\mu}_a$. An error model then estimates the quantification error and, in combination with an aleatoric uncertainty metric, a region of interest is defined. (**b**) An approach in which one model is used to directly estimate $\hat{\mu}_a$ from the input data. $I^{\text{aleatoric}}$ is calculated on the basis of the input data and $I^{\text{epistemic}}$ is estimated with a second model.

Validation Data.   We simulated an in silico dataset containing 3600 training samples, 400 validation samples, as well as 150 calibration and test samples which were used in all experiments. Each data sample consists of the ground truth optical tissue parameters, the corresponding light fluence, and the initial pressure distribution simulated with the mcxyz framework [51], which is a Monte Carlo simulation of photon propagation where we assume a symmetric illumination geometry with two laser outputs. The data sample also comprises raw time-series data simulated using the k-Wave [52] toolkit with the first-order 2D k-space method, assuming a 128-element linear array ultrasound transducer with a central frequency of 7.5 MHz, a bandwidth of 60%, and a sample rate of 1.5×10^{-8} s. The illumination and ultrasound geometry are depicted in Figure 4. Each tissue volume sample comprises 1–10 tubular vessel structures, whose absorption coefficients μ_a range from 2 to 10 cm^{-1} in vessel structures and are assumed constant with 0.1 cm^{-1} in the background. We chose a constant reduced scattering coefficient of 15 cm^{-1} in both background and vessel structures. Additional details on the simulation parameters can also be found in our previous work [53]. The raw time-series data was noised after k-space simulation with an additive Gaussian noise model of recorded noise of our system [54]. For the experiments where we directly use p_0, we noise the initial pressure distribution with a Gaussian additive noise model, as also described in [7]. In our case, the noise model comprised an additive component with $(5 \pm 5)\%$ of the mean signal and a multiplicative component with a standard deviation of 20% to simulate imperfect reconstructions of p_0. The data used in this study is available in a Zenodo repository [55].
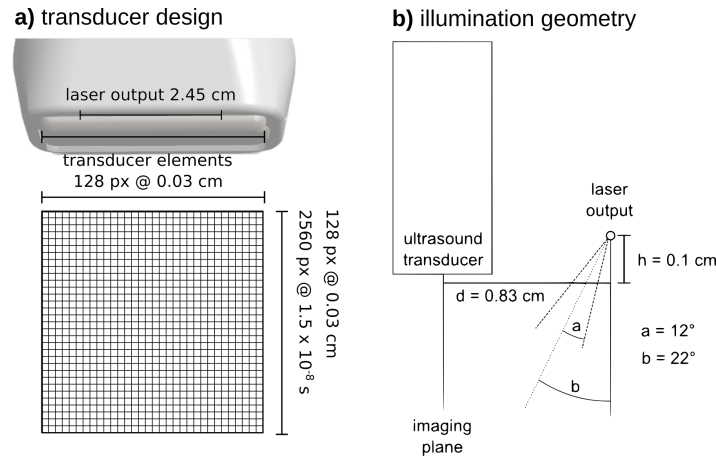
Figure 4. Depiction of the illumination geometry and the transducer design which is based on our Fraunhofer DiPhAS photoacoustic imaging (PAI) system [54]. (**a**) The ultrasound transducer design with the position of the laser output and the transducer elements, as well as the imaging plane; (**b**) one-half of the symmetric transducer design, where the laser outputs are in parallel left and right to the transducer elements over a length of 2.45 cm.

Experimental Design. We performed five in silico experiments to validate our approach to confidence estimation in qPAI—one experiment with naïve fluence correction applied to p_0 data, as well as our different configurations for quantification with deep learning. Both methods shown in Figure 3 are applied to initial pressure p_0, as well as raw time-series data. We used the Trixi [56] framework to perform the experiments. All qPAI models were trained on the training set and the progress was supervised with the validation set. We also used the validation set for hyperparameter optimization of the number of training epochs and batch sizes. We trained for 50 epochs, showing the network 10^4 randomly drawn and augmented samples from the training set; each epoch had a learning rate of 10^{-4}, used an L_1 loss function, and augmented every sample with a white Gaussian multiplicative noise model and horizontal mirroring to prevent the model from overfitting. Afterward, we estimated the optical absorption $\hat{\mu}_a$ of the validation set, calculated the relative errors $e_{\mu_a} = |\hat{\mu}_a - \mu_a|/\mu_a$, and trained the external observing neural networks on the errors of the validation set with the same hyperparameters, supervising the progression on the calibration set. For better convergence, we used the weights of the p_0 estimation model as a starting point for the e_{μ_a} estimation deep learning models. All results presented in this paper were computed on the test set.

3. Results

We report the relative absorption quantification error e_{μ_a} at various different confidence thresholds (*CT*). To this end, we evaluated only the top n percent most confident estimates by excluding all estimates below a certain *CT*. We performed this evaluation over all ROI image samples of the respective dataset and examined the relative changes in e_{μ_a} compared with the evaluation over all ROI pixels. This was done in five different in silico experiments, corresponding to the qPAI methods when applied to initial pressure, as well as raw time-series input data. Our findings are summarized in Figure 5.
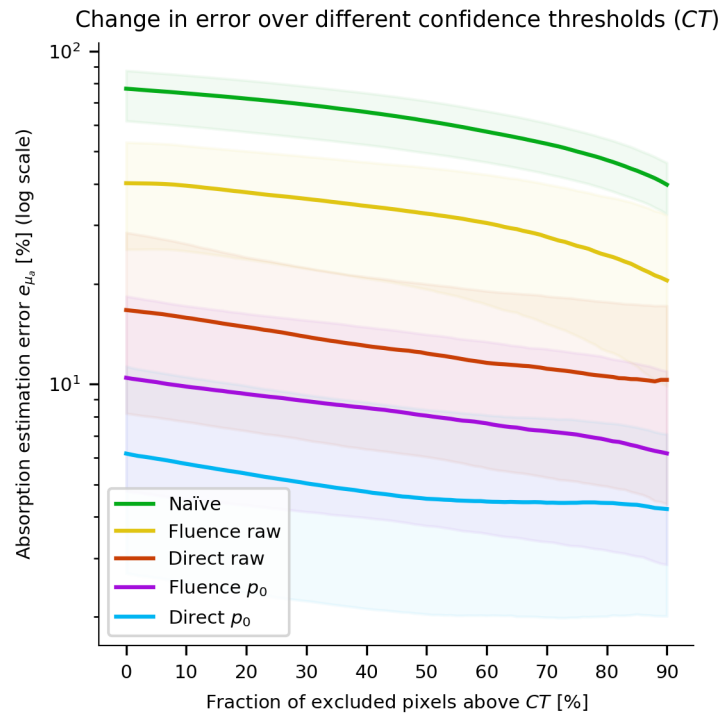
Figure 5. Quantification error as a function of the confidence threshold (*CT*) for five different quantification methods. The line shows the median relative absorption estimation error when only evaluating with the most confident estimates regarding *CT*, and the transparent background shows the corresponding interquartile range. Naïve: Fluence correction with a homogeneous fluence estimate; Fluence raw/p_0: Deep learning-based quantification of the fluence applied to p_0 and raw time-series input data and subsequent estimation of μ_a; Direct raw/p_0: End-to-end deep learning-based quantification of μ_a applied to p_0 and raw time-series input data.

Figure 5 shows the absorption quantification error e_{μ_a} for all five experiments for confidence thresholds *CT* ranging from 10 to 100%. In all cases, the error decreases when excluding more pixels with a higher estimated error. When only considering the top 50% most confident estimates, our method yields a decrease in the error e_{μ_a} of up to approx. 30% (increasing to up to about a 50% improvement when evaluating only the top 10% of the most confident estimates). Figure 6 shows violin plots visualizing the changes in the distribution of e_{μ_a} when applying different confidence thresholds *CT*. The results reveal a meandering of the distribution toward lower error values. Note that the results are only given for the ROI. When computing the statistics over the entire image (thus decreasing the difficulty of the problem due to the homogeneous background), the median quantification error drops to about 0.1% (direct estimation), 5–10% (fluence correction), and 20% (naïve approach).

Figure 7 shows representative images of the experiment corresponding to the end-to-end direct μ_a quantification method applied to p_0 data. It shows samples of the test set comprising the best, median, and worst result when applying a 50% *CT* to narrow down the ROI. The results show a maximum increase of nearly 80% in accuracy in the best case while achieving a median improvement of about 29% and worsening the quantification results by 28% in the worst case from the test set. Analogous illustrations for the other experiments can be found in Appendices A–D.
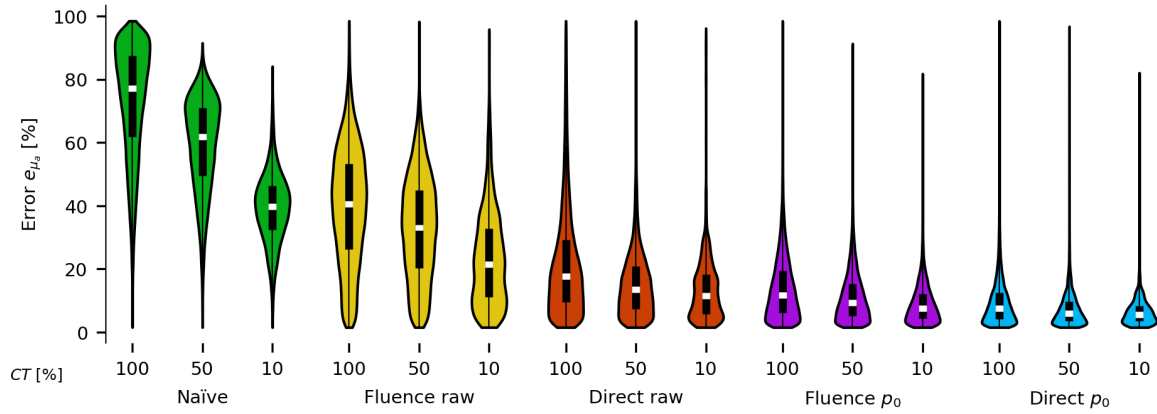
Figure 6. Visualization of the changes in the distribution of the absorption quantification error e_{μ_a} when applying different confidence thresholds $CT = \{100\%, 50\%, 10\%\}$. The plot shows results for all five conducted experiments. The white line denotes the median, and the black box corresponds to the interquartile range. Outliers of e_{μ_a} with a value greater than 100% have been omitted from this plot.

a. ground truth μ_a [cm^{-1}]   **b.** μ_a estimate [cm^{-1}]   **c.** ROI est. error $\hat{e}_{\mu_a}$ [%]   **d.** ROI error e_{μ_a}[%]
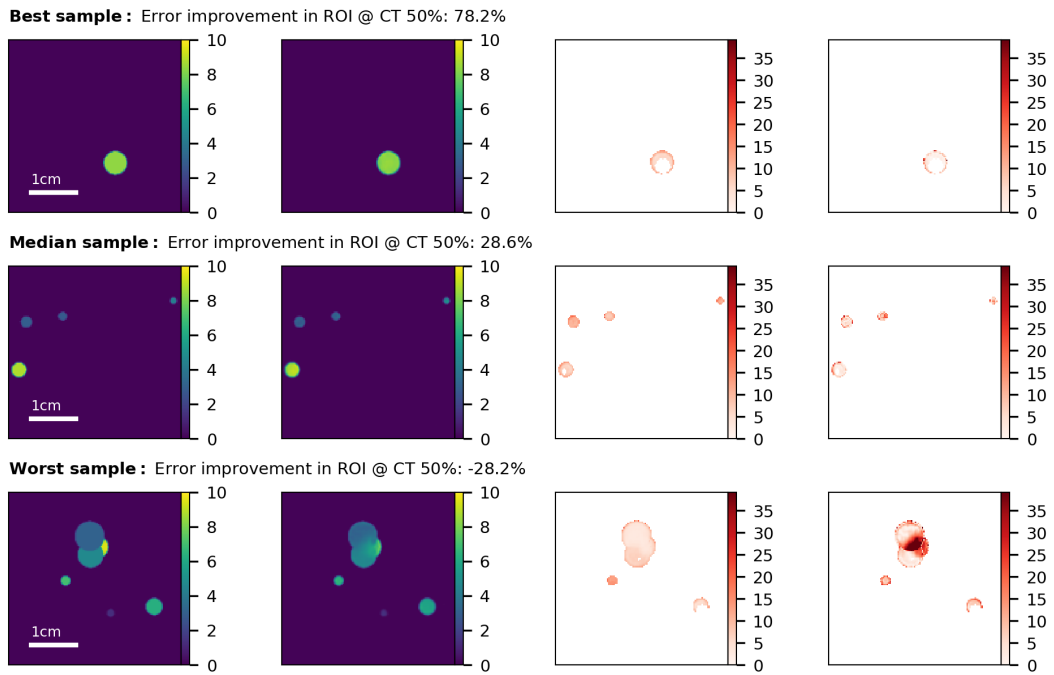
Figure 7. Sample images of the end-to-end direct μ_a quantification method applied to p_0 data, showing the best, the worst, and the median performance of our method when considering only the 50% most confident quantification estimations. All images show the (**a**) ground truth absorption coefficients (**b**) reconstructed absorption, (**c**) error estimate from external model, (**d**) the actual quantification error.

4. Discussion

In this work, we present a method which uses estimated confidences in the context of photoacoustic signal quantification to increase the accuracy of the quantification algorithms. In theory, the proposed method is independent of the underlying qPAI method, as it uses a deep learning model to observe the errors resulting from the quantification method in order to provide confidence estimates. While the application of our method to other state-of-the-art qPAI methods is the subject of future work, we aimed to show the general applicability of our method by also incorporating a

naïve fluence compensation method into the experiments. Our results suggest that using a method to estimate confidence information to refine a region of interest for subsequent computations might be a valuable tool for increasing the robustness of qPAI methods and could be easily integrated in future qPAI research.

We hypothesized that our confidence metric is indicative of e_{μ_a}. In the experiments, we showed that a deep learning model is able to learn a representation of the errors of the quantification method leading to error improvements of 10–50% in region-of-interest structures and yielding up to 5-fold improvements in background structures. Furthermore, Figure 5 shows that the absorption estimation error does not decrease monotonously, especially for the qPAI methods that yield more accurate results. One reason for this might be that the confidence estimates are not correlated to the quantification error and that low confidences might still correspond to low errors. One has to point out the worse performance of the quantification methods when applied directly to raw time-series data. One reason for this might be that the addition of the acoustic inverse problem and the inclusion of a realistic noise model greatly increased the complexity of the problem and reduced the amount of information in the data due to, e.g., limited-view artifacts. At the same time, we did not increase the number of training samples or change the methodology to account for this.

The dataset simulated for the experiments was specifically designed such that out-of-plane fluence effects cannot occur, as the in silico phantoms contain only straight tubular vessel structures that run orthogonal to the imaging plane. Additionally, other a priori assumptions of the parameter space were made, such as a constant background absorption, an overall constant scattering coefficient, and a fixed illumination geometry. Due to the homogeneous nature of the background structure, the errors observed in our study are highly specialized to our dataset. This is especially apparent with the direct estimation method, as here, e_{μ_a} is never greater than 0.2%. As such, we focus on reporting the errors in the ROI, as only reporting the results of the entire images would be misleading. In order for the method to generalize to more complex or in vitro datasets and yield similar μ_a and confidence estimation results, more elaborate and diverse datasets would need to be simulated. Nevertheless, the experiments demonstrate that applying an ROI threshold based on the estimation of the quantification error can lead to an increase in accuracy for a given dataset regardless of the underlying qPAI method.

From a qPAI perspective, end-to-end deep learning-based inversion of PA data is feasible in specific contexts and for specific in silico datasets, as shown previously [20] and in this work. However, PA signal quantification cannot be regarded as solved in a general manner. One of the main reasons is the large gap between simulated in silico data and in vivo recordings. In order for deep learning to tackle this problem, either highly sophisticated unsupervised domain adaptation methods have to be developed, or a large number of labeled correspondences between the simulation domain and real recorded images need to be provided, which is not currently feasible due to the lack of methodology to reliably measure ground truth optical properties in in vivo settings. However, with the promising progress in PA image reconstruction from limited-view geometries with deep learning techniques (cf., e.g., [57,58]), it might be possible to start bridging the gap and to improve on the current methods for qPAI.

Author Contributions: Conceptualization, J.G., T.K. and L.M.-H.; methodology, J.G., T.K. and T.A.; software, J.G.; data curation, J.G.; writing—original draft preparation, J.G.; writing—review and editing, J.G., T.K., T.A. and L.M.-H.; supervision, L.M.-H.

Conflicts of Interest: The authors declare no conflict of interest.

Abbreviations

The following abbreviations are used in this manuscript:

CNR   Contrast-To-Noise-Ratio
PA   Photoacoustic
PAI   Photoacoustic Imaging
qPAI   quantitative PAI
ROI   Region of Interest
CT   Confidence Threshold

Appendix A. Results for the Naïve Fluence Compensation Method

a. ground truth μ_a [cm^{-1}] **b.** μ_a estimate [cm^{-1}] **c.** ROI est. error $e_{\hat{\mu}_a}$ [%] **d.** ROI error e_{μ_a}[%]

Figure A1. Sample images showing the best, the worst, and the median performance of our method when considering only the 50% most confident quantification estimations. All images show the (**a**) ground truth absorption coefficients (**b**) reconstructed absorption, (**c**) error estimate from external model, (**d**) the actual quantification error.

Appendix B. Results for Fluence Correction on p_0 Data

a. ground truth μ_a [cm^{-1}]   **b.** μ_a estimate [cm^{-1}]   **c.** ROI est. error $e_{\hat{\mu}_a}$ [%]   **d.** ROI error e_{μ_a}[%]

Figure A2. Sample images showing the best, the worst, and the median performance of our method when considering only the 50% most confident quantification estimations. All images show the (**a**) ground truth absorption coefficients (**b**) reconstructed absorption, (**c**) error estimate from external model, (**d**) the actual quantification error.

Appendix C. Results for Fluence Correction on Raw PA Time Series Data

a. ground truth μ_a [cm^{-1}]   **b.** μ_a estimate [cm^{-1}]   **c.** ROI est. error $e_{\hat{\mu}_a}$ [%]   **d.** ROI error e_{μ_a}[%]

Figure A3. Sample images showing the best, the worst, and the median performance of our method when considering only the 50% most confident quantification estimations. All images show the (**a**) ground truth absorption coefficients (**b**) reconstructed absorption, (**c**) error estimate from external model, (**d**) the actual quantification error.

Appendix D. Results for Direct μ_a Estimation on Raw PA Time Series Data
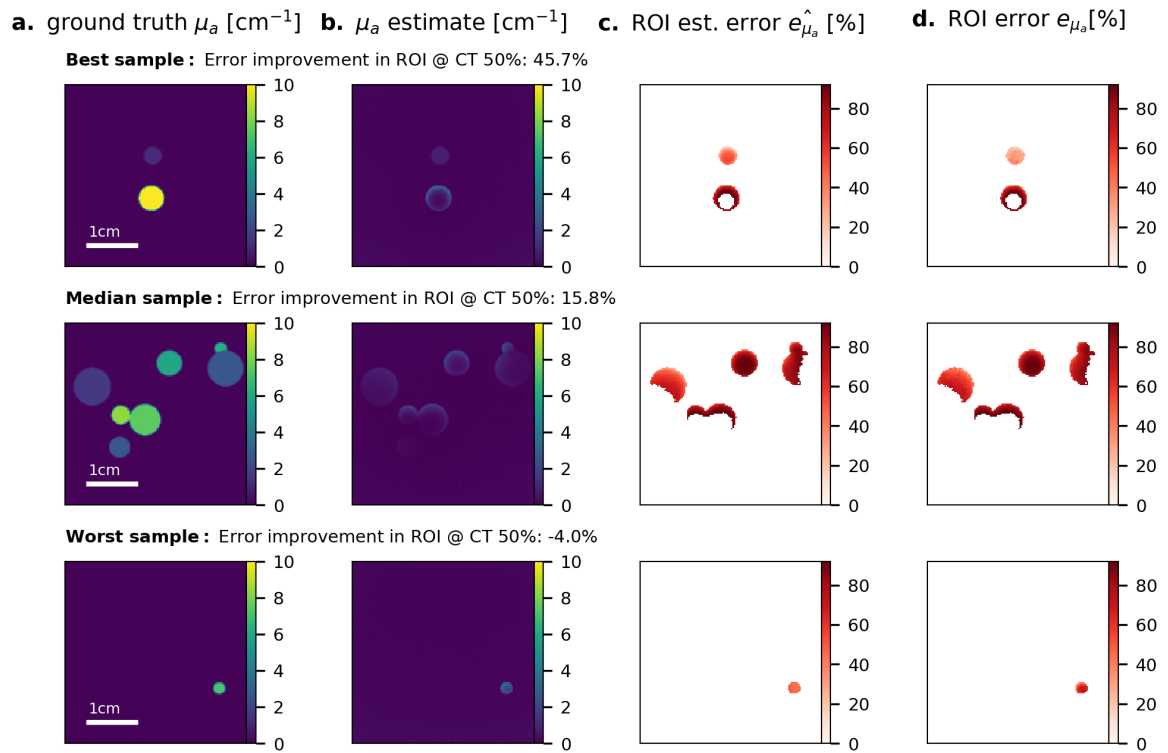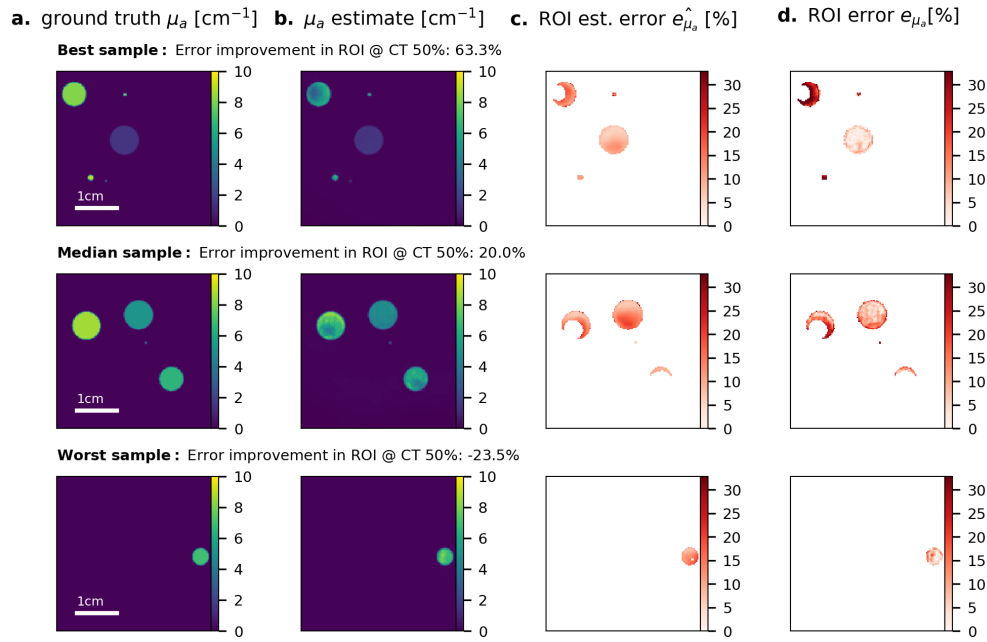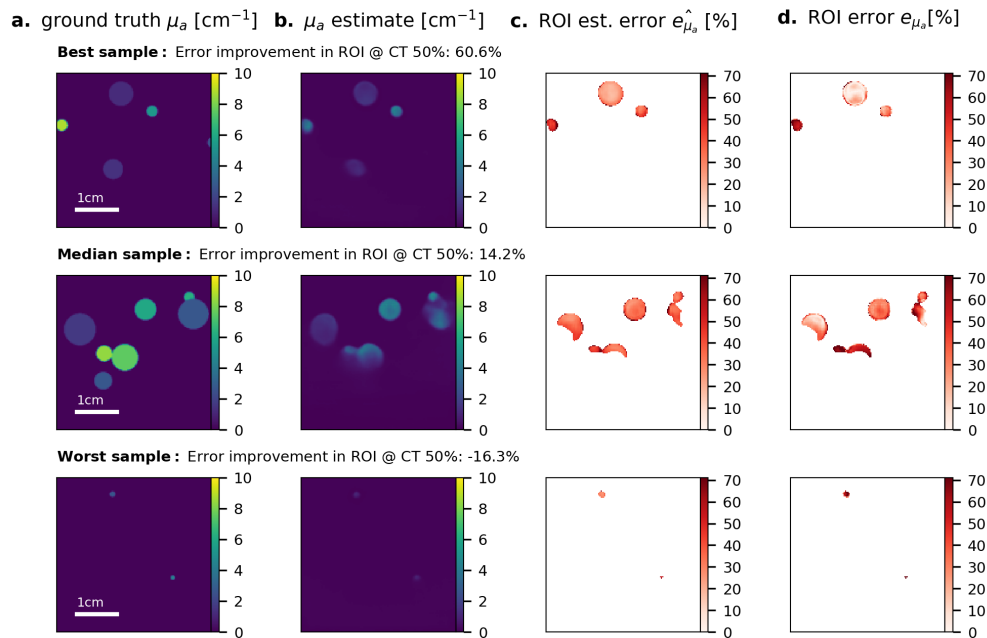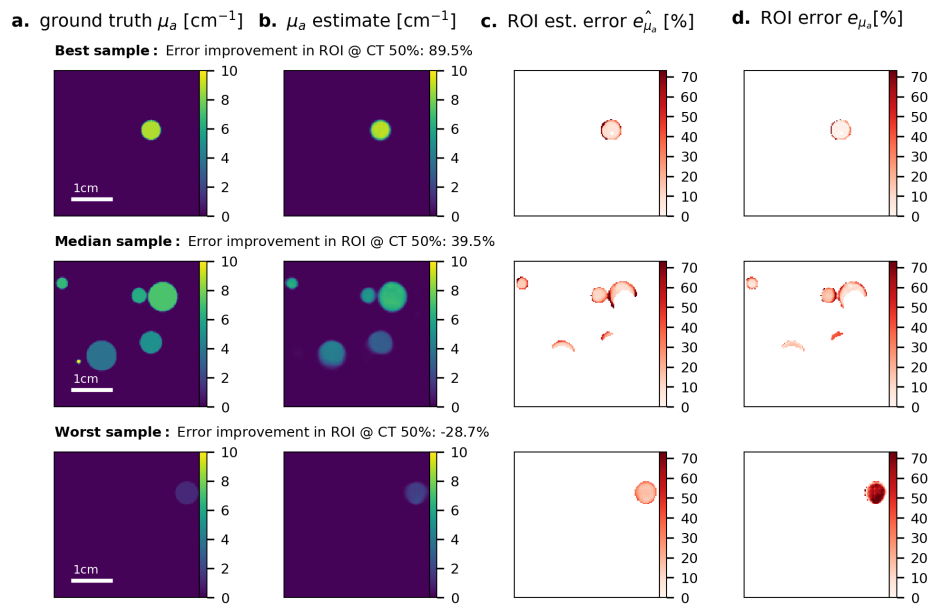

Figure A4. Sample images showing the best, the worst, and the median performance of our method when considering only the 50% most confident quantification estimations. All images show the (**a**) ground truth absorption coefficients (**b**) reconstructed absorption, (**c**) error estimate from external model, (**d**) the actual quantification error.

References

1. Valluru, K.S.; Willmann, J.K. Clinical photoacoustic imaging of cancer. *Ultrason* **2016**, *35*, 267–280. [CrossRef] [PubMed]
2. Knieling, F.; Neufert, C.; Hartmann, A.; Claussen, J.; Urich, A.; Egger, C.; Vetter, M.; Fischer, S.; Pfeifer, L.; Hagel, A.; et al. Multispectral Optoacoustic Tomography for Assessment of Crohn's Disease Activity. *N. Engl. J. Med.* **2017**, *376*, 1292–1294. [CrossRef] [PubMed]
3. Laufer, J. Photoacoustic Imaging: Principles and Applications. In *Quantification of Biophysical Parameters in Medical Imaging*; Springer: Cham, The Netherlands, 2018; pp. 303–324. [CrossRef]
4. Mitcham, T.; Taghavi, H.; Long, J.; Wood, C.; Fuentes, D.; Stefan, W.; Ward, J.; Bouchard, R. Photoacoustic-based SO_2 estimation through excised bovine prostate tissue with interstitial light delivery. *Photoacoust* **2017**, *7*, 47–56. [CrossRef] [PubMed]
5. Jacques, S.L. Optical properties of biological tissues: A review. *Phys. Med. Boil.* **2013**, *58*, R37. [CrossRef] [PubMed]
6. Tzoumas, S.; Nunes, A.; Olefir, I.; Stangl, S.; Symvoulidis, P.; Glasl, S.; Bayer, C.; Multhoff, G.; Ntziachristos, V. Eigenspectra optoacoustic tomography achieves quantitative blood oxygenation imaging deep in tissues. *Nat. Commun.* **2016**, *7*, 12121. [CrossRef] [PubMed]
7. Cox, B.T.; Arridge, S.R.; Köstli, K.P.; Beard, P.C. Two-dimensional quantitative photoacoustic image reconstruction of absorption distributions in scattering media by use of a simple iterative method. *Appl. Opt.* **2006**, *45*, 1866–1875. [CrossRef] [PubMed]
8. Cox, B.; Laufer, J.; Beard, P. The challenges for quantitative photoacoustic imaging. Photons Plus Ultrasound: Imaging and Sensing. *Int. Soc. Opt. Photonics* **2009**, *7177*, 717713.
9. Cox, B.; Laufer, J.G.; Arridge, S.R.; Beard, P.C. Quantitative spectroscopic photoacoustic imaging: A review. *J. Biomed. Opt.* **2012**, *17*, 061202. [CrossRef]
10. Yuan, Z.; Jiang, H. Quantitative photoacoustic tomography: Recovery of optical absorption coefficient maps of heterogeneous media. *Appl. Phys. Lett.* **2006**, *88*, 231101. [CrossRef]
11. Yuan, Z.; Jiang, H. Quantitative photoacoustic tomography. *Philos. Trans. R. Soc. Lond. A Math. Phys. Eng. Sci.* **2009**, *367*, 3043–3054. [CrossRef]

12. Wang, Y.; He, J.; Li, J.; Lu, T.; Li, Y.; Ma, W.; Zhang, L.; Zhou, Z.; Zhao, H.; Gao, F. Toward whole-body quantitative photoacoustic tomography of small-animals with multi-angle light-sheet illuminations. *Biomed. Opt. Express* **2017**, *8*, 3778–3795. [CrossRef] [PubMed]

13. Saratoon, T.; Tarvainen, T.; Cox, B.; Arridge, S. A gradient-based method for quantitative photoacoustic tomography using the radiative transfer equation. *Inverse Probl.* **2013**, *29*, 075006. [CrossRef]

14. Tarvainen, T.; Pulkkinen, A.; Cox, B.T.; Arridge, S.R. Utilising the radiative transfer equation in quantitative photoacoustic tomography. *Photons Plus Ultrasound Imaging Sens.* **2017**, *10064*, [CrossRef]

15. Haltmeier, M.; Neumann, L.; Rabanser, S. Single-stage reconstruction algorithm for quantitative photoacoustic tomography. *Inverse Probl.* **2015**, *31*, 065005. [CrossRef]

16. Kaplan, B.A.; Buchmann, J.; Prohaska, S.; Laufer, J. Monte-Carlo-based inversion scheme for 3D quantitative photoacoustic tomography. Photons Plus Ultrasound: Imaging and Sensing. *Int. Soc. Opt. Photonics* **2017**, *10064*, 100645J.

17. Tzoumas, S.; Ntziachristos, V. Spectral unmixing techniques for optoacoustic imaging of tissue pathophysiology. *Philos. Trans. R. Soc. A* **2017**, *375*, 20170262. [CrossRef] [PubMed]

18. Perekatova, V.; Subochev, P.; Kleshnin, M.; Turchin, I. Optimal wavelengths for optoacoustic measurements of blood oxygen saturation in biological tissues. *Biomed. Opt. Express* **2016**, *7*, 3979–3995. [CrossRef]

19. Glatz, J.; Deliolanis, N.C.; Buehler, A.; Razansky, D.; Ntziachristos, V. Blind source unmixing in multi-spectral optoacoustic tomography. *Opt. Express* **2011**, *19*, 3175–3184. [CrossRef]

20. Cai, C.; Deng, K.; Ma, C.; Luo, J. End-to-end deep neural network for optical inversion in quantitative photoacoustic imaging. *Opt. Lett.* **2018**, *43*, 2752–2755. [CrossRef]

21. Kirchner, T.; Gröhl, J.; Maier-Hein, L. Context encoding enables machine learning-based quantitative photoacoustics. *J. Biomed. Opt.* **2018**, *23*, 056008. [CrossRef]

22. Fonseca, M.; Saratoon, T.; Zeqiri, B.; Beard, P.; Cox, B. Sensitivity of quantitative photoacoustic tomography inversion schemes to experimental uncertainty. SPIE BiOS. *Int. Soc. Opt. Photonics* **2016**, *9708*, 97084X.

23. Maier-Hein, L.; Franz, A.M.; Santos, T.R.D.; Schmidt, M.; Fangerau, M.; Meinzer, H.; Fitzpatrick, J.M. Convergent Iterative Closest-Point Algorithm to Accomodate Anisotropic and Inhomogenous Localization Error. *IEEE Trans. Pattern Anal. Mach. Intell.* **2012**, *34*, 1520–1532. [CrossRef] [PubMed]

24. Alterovitz, R.; Branicky, M.; Goldberg, K. Motion Planning Under Uncertainty for Image-guided Medical Needle Steering. *Int. J. Robot. Res.* **2008**, *27*, 1361–1374. [CrossRef] [PubMed]

25. Sykes, J.R.; Brettle, D.S.; Magee, D.R.; Thwaites, D.I. Investigation of uncertainties in image registration of cone beam CT to CT on an image-guided radiotherapy system. *Phys. Med. Boil.* **2009**, *54*, 7263–7283. [CrossRef] [PubMed]

26. Risholm, P.; Janoos, F.; Norton, I.; Golby, A.J.; Wells, W.M. Bayesian characterization of uncertainty in intra-subject non-rigid registration. *Med. Image Anal.* **2013**, *17*, 538–555. [CrossRef] [PubMed]

27. Nair, T.; Precup, D.; Arnold, D.L.; Arbel, T. Exploring Uncertainty Measures in Deep Networks for Multiple Sclerosis Lesion Detection and Segmentation. In Proceedings of the International Conference on Medical Image Computing and Computer-Assisted Intervention, Granada, Spain, 16–20 September 2018; Springer: Berlin, Germany, 2018; pp. 655–663.

28. Srivastava, N.; Hinton, G.; Krizhevsky, A.; Sutskever, I.; Salakhutdinov, R. Dropout: A simple way to prevent neural networks from overfitting. *J. Mach. Learn. Res.* **2014**, *15*, 1929–1958.

29. Gal, Y.; Ghahramani, Z. Dropout as a Bayesian approximation: Representing model uncertainty in deep learning. In Proceedings of the International Conference on Machine Learning, New York, NY, USA, 19–24 June 2016; pp. 1050–1059.

30. Li, Y.; Gal, Y. Dropout Inference in Bayesian Neural Networks with Alpha-divergences. *arXiv* **2017**, arXiv:1703.02914.

31. Leibig, C.; Allken, V.; Ayhan, M.S.; Berens, P.; Wahl, S. Leveraging uncertainty information from deep neural networks for disease detection. *Sci. Rep.* **2017**, *7*, 17816. [CrossRef]

32. Feindt, M. A Neural Bayesian Estimator for Conditional Probability Densities. *arXiv* **2004**, arXiv:Phys./0402093.

33. Zhu, Y.; Zabaras, N. Bayesian deep convolutional encoder-decoder networks for surrogate modeling and uncertainty quantification. *J. Comput. Phys.* **2018**, *366*, 415–447. [CrossRef]

34. Kohl, S.A.; Romera-Paredes, B.; Meyer, C.; De Fauw, J.; Ledsam, J.R.; Maier-Hein, K.H.; Eslami, S.; Rezende, D.J.; Ronneberger, O. A Probabilistic U-Net for Segmentation of Ambiguous Images. *arXiv* **2018**, arXiv:1806.05034.

35. Kingma, D.P.; Welling, M. Auto-encoding variational bayes. *arXiv* **2013**, arXiv:1312.6114.
36. Mescheder, L.; Nowozin, S.; Geiger, A. Adversarial variational bayes: Unifying variational autoencoders and generative adversarial networks. *arXiv* **2017**, arXiv:1701.04722.
37. Ardizzone, L.; Kruse, J.; Wirkert, S.; Rahner, D.; Pellegrini, E.W.; Klessen, R.S.; Maier-Hein, L.; Rother, C.; Köthe, U. Analyzing Inverse Problems with Invertible Neural Networks. *arXiv* **2018**, arXiv:1808.04730.
38. Lakshminarayanan, B.; Pritzel, A.; Blundell, C. Simple and Scalable Predictive Uncertainty Estimation using Deep Ensembles. In *Advances in Neural Information Processing Systems 30*; Guyon, I., Luxburg, U.V., Bengio, S., Wallach, H., Fergus, R., Vishwanathan, S., Garnett, R., Eds.; Curran Associates, Inc.: Red Hook, NY, USA, 2017; pp. 6402–6413.
39. Smith, L.; Gal, Y. Understanding Measures of Uncertainty for Adversarial Example Detection. *arXiv* **2018**, arXiv:1803.08533.
40. Pulkkinen, A.; Cox, B.T.; Arridge, S.R.; Goh, H.; Kaipio, J.P.; Tarvainen, T. Direct estimation of optical parameters from photoacoustic time series in quantitative photoacoustic tomography. *IEEE Trans. Med. Imaging* **2016**, *35*, 2497–2508. [CrossRef] [PubMed]
41. Pulkkinen, A.; Cox, B.T.; Arridge, S.R.; Kaipio, J.P.; Tarvainen, T. Estimation and uncertainty quantification of optical properties directly from the photoacoustic time series. Photons Plus Ultrasound: Imaging and Sensing 2017. *Int. Soc. Opt. Photonics* **2017**, *10064*, 100643N.
42. Tick, J.; Pulkkinen, A.; Tarvainen, T. Image reconstruction with uncertainty quantification in photoacoustic tomography. *J. Acoust. Soc. Am.* **2016**, *139*, 1951–1961. [CrossRef] [PubMed]
43. Tick, J.; Pulkkinen, A.; Tarvainen, T. Photoacoustic image reconstruction with uncertainty quantification. In *EMBEC & NBC 2017*; Eskola, H., Väisänen, O., Viik, J., Hyttinen, J., Eds.; Springer: Singapore, 2018; pp. 113–116.
44. Gröhl, J.; Kirchner, T.; Maier-Hein, L. Confidence estimation for quantitative photoacoustic imaging. Photons Plus Ultrasound: Imaging and Sensing 2018. *Int. Soc. Opt. Photonics* **2018**, *10494*, 104941C. [CrossRef]
45. Welvaert, M.; Rosseel, Y. On the Definition of Signal-To-Noise Ratio and Contrast-To-Noise Ratio for fMRI Data. *PLoS ONE* **2013**, *8*, e77089. doi:10.1371/journal.pone.0077089. [CrossRef] [PubMed]
46. Ronneberger, O.; Fischer, P.; Brox, T. U-Net: Convolutional Networks for Biomedical Image Segmentation. In *Medical Image Computing and Computer-Assisted Intervention (MICCAI)*; Springer: Berlin, Germany, 2015; Volume 9351, pp. 234–241.
47. Paszke, A.; Gross, S.; Chintala, S.; Chanan, G.; Yang, E.; DeVito, Z.; Lin, Z.; Desmaison, A.; Antiga, L.; Lerer, A. Automatic Differentiation in PyTorch. In Proceedings of the 31st Conference on Neural Information Processing Systems (NIPS 2017), Long Beach, CA, USA, 4–9 December 2017.
48. Isensee, F.; Petersen, J.; Klein, A.; Zimmerer, D.; Jaeger, P.F.; Kohl, S.; Wasserthal, J.; Koehler, G.; Norajitra, T.; Wirkert, S.; et al. nnU-Net: Self-adapting Framework for U-Net-Based Medical Image Segmentation. *arXiv* **2018**, arXiv:1809.10486.
49. Bauer, A.Q.; Nothdurft, R.E.; Erpelding, T.N.; Wang, L.V.; Culver, J.P. Quantitative photoacoustic imaging: Correcting for heterogeneous light fluence distributions using diffuse optical tomography. *J. Biomed. Opt.* **2011**, *16*, 096016–096016. [CrossRef]
50. Daoudi, K.; Hussain, A.; Hondebrink, E.; Steenbergen, W. Correcting photoacoustic signals for fluence variations using acousto-optic modulation. *Opt. Express* **2012**, *20*, 14117–14129. [CrossRef] [PubMed]
51. Jacques, S.L. Coupling 3D Monte Carlo light transport in optically heterogeneous tissues to photoacoustic signal generation. *Photoacoust* **2014**, *2*, 137–142. [CrossRef] [PubMed]
52. Treeby, B.E.; Cox, B.T. k-Wave: MATLAB toolbox for the simulation and reconstruction of photoacoustic wave fields. *J. Biomed. Opt.* **2010**, *15*, 021314. [CrossRef] [PubMed]
53. Waibel, D.; Gröhl, J.; Isensee, F.; Kirchner, T.; Maier-Hein, K.; Maier-Hein, L. Reconstruction of initial pressure from limited view photoacoustic images using deep learning. Photons Plus Ultrasound: Imaging and Sensing 2018. *Int. Soc. Opt. Photonics* **2018**, *10494*, 104942S. [CrossRef]
54. Kirchner, T.; Wild, E.; Maier-Hein, K.H.; Maier-Hein, L. Freehand photoacoustic tomography for 3D angiography using local gradient information. *Photons Plus Ultrasound Imaging Sens.* **2016**, *9708*, 97083G. [CrossRef]
55. Gröhl, J.; Kirchner, T.; Adler, T.; Maier-Hein, L. *In Silico 2D Photoacoustic Imaging Data*; Zenodo: Meyrin, Switzerland, 2018. [CrossRef]

56. Zimmerer, D.; Petersen, J.; Koehler, G.; Wasserthal, J.; Adler, T.; Wirkert, A. *MIC-DKFZ/Trixi: Pre-Release*; Zenodo: Meyrin, Switzerland, 2018. doi:10.5281/zenodo.1345137.

57. Hauptmann, A.; Lucka, F.; Betcke, M.; Huynh, N.; Adler, J.; Cox, B.; Beard, P.; Ourselin, S.; Arridge, S. Model-Based Learning for Accelerated, Limited-View 3-D Photoacoustic Tomography. *IEEE Trans. Med. Imaging* **2018**, *37*, 1382–1393. [CrossRef]

58. Antholzer, S.; Haltmeier, M.; Schwab, J. Deep learning for photoacoustic tomography from sparse data. *Inverse Probl. Sci. Eng.* **2018**. [CrossRef]

C2

ESTIMATION OF BLOOD OXYGENATION WITH LEARNED SPECTRAL
DECOLORING FOR QUANTITATIVE PHOTOACOUSTIC IMAGING

This manuscript presets a method for direct quantification of sO_2 and
not like classic qPAI the quantification of optical properties. Such an approach should be more suited for realistic applications because it does
not need to solve the acoustic inverse problem explicitly and needs
to identify spectral coloring instead of explicit fluence values. A very
preliminary validation experiment shows that an *in vivo* quantification
is in principle possible.

Own contribution

I am not the main author of this manuscript.

The initial manuscript was drafted by Janek Gröhl and edited and
revised by all authors including me.

The method was conceived of by Janek Gröhl and me – I named
it LSD-qPAI – but I had no part in the deep learning methodology
and concept. Janek Gröhl and I intensely discussed the concept.
The simulation experiments were designed and discussed by all the
authors, and performed by Janek Gröhl. I curated and preprocessed
the data for the *in vivo* validation experiment.

Estimation of blood oxygenation with learned spectral decoloring for quantitative photoacoustic imaging (LSD-qPAI)

Janek Gröhl [a,b], **Thomas Kirchner** [a,c], **Tim Adler** [a,d], and **Lena Maier-Hein** [a,b]

[a]Division of Computer Assisted Medical Interventions (CAMI), German Cancer Research Center (DKFZ), 69120 Heidelberg, Germany; [b]Medical Faculty, Heidelberg University, 69120 Heidelberg, Germany; [c]Faculty of Physics and Astronomy, Heidelberg University, 69120 Heidelberg, Germany; [d]Faculty of Mathematics and Computer Science, Heidelberg University, 69120 Heidelberg, Germany

Correspondence: j.groehl@dkfz-heidelberg.de

One of the main applications of photoacoustic (PA) imaging is the recovery of functional tissue properties, such as blood oxygenation (sO$_2$). This is typically achieved by linear spectral unmixing of relevant chromophores from multispectral photoacoustic images. Despite the progress that has been made towards quantitative PA imaging (qPAI), most sO$_2$ estimation methods yield poor results in realistic settings. In this work, we tackle the challenge by employing learned spectral decoloring for quantitative photoacoustic imaging (LSD-qPAI) to obtain quantitative estimates for blood oxygenation. LSD-qPAI computes sO$_2$ directly from pixel-wise initial pressure spectra S_{P_0}, which are vectors comprised of the initial pressure at the same spatial location over all recorded wavelengths. Initial results suggest that LSD-qPAI is able to obtain accurate sO$_2$ estimates directly from multispectral photoacoustic measurements *in silico* and plausible estimates *in vivo*.

Keywords:
Deep learning, multispectral imaging, photoacoustics

1. Introduction

Photoacoustic (PA) imaging is a medical imaging modality that offers an optical signal contrast up to several centimeters deep inside tissue. In the last two decades, a lot of progress has been made towards its translation into clinical routine. However, the accurate and robust quantification of optical tissue properties or derived functional tissue properties still remains a major challenge (1, 2). In order to obtain functional tissue properties such as blood oxygen saturation (sO$_2$), spectral unmixing algorithms are used to decompose a multispectral signal and to determine the quantity of specific chromophores that contributed to the signal spectrum over the wavelengths. For this process, the core assumption is that the acquired PA signal image I - which is ideally an approximate reconstruction from the initial pressure distribution p$_0$ - is proportional to the optical absorption coefficient ($I \approx p_0 \propto \mu_a$) (3). However, this assumption does not always hold because p$_0$ is mainly proportional to the product of optical absorption μ_a and the light fluence ϕ ($I \approx p_0 \propto \mu_a \cdot \phi$). Hence, the fluence has an influence on the recorded spectra and potentially leads to large errors in sO$_2$ quantification.

To overcome this issue, part of the research in the field of quantitative PA imaging (qPAI) aims at compensating for these fluence effects (cf. e.g. (4–7)). For a long time, the field has focused on model-based approaches to extract quantitative information on optical tissue properties (8, 9) which typically suffer from long computation times. More recently, also machine learning-based approaches to qPAI have been published (10–12). These methods are often substantially faster than model-based algorithms but have not yet been demonstrated to work accurately and robustly in realistic *in vitro*

settings or *in vivo*. Due to the lack of fast and accurate fluence compensation algorithms, most researchers and applications default to the simple linear unmixing algorithms in order to provide qualitative rather than quantitative values for relevant functional tissue parameters.

This work tackles quantification of the functional tissue property sO$_2$ by introducing learned spectral decoloring for quantitative photoacoustic imaging (LSD-qPAI). LSD-qPAI is based on the assumption that there is a substantial benefit in considering fluence effects when quantifying sO$_2$ (7, 13, 14), compared to spectrally unmixing hemoglobin (Hb) and oxyhemoglobin (HbO$_2$) with commonly used linear methods (3) that neglect the aforementioned fluence effects. Previous deep learning approaches to qPAI try to estimate optical absorption from PA measurements and then derive functional tissue properties from these estimations, potentially leading to error propagation (10). In contrast to this, we propose to directly estimate the functional tissue parameter sO$_2$ from pixel-wise p$_0$ spectra S_{P_0}, which is a vector of the initial pressure at the same spatial location over all recorded wavelengths. For this, we use multispectral *in silico* p$_0$ training data, as illustrated in Figure 1. This way, we force the machine learning algorithm to account for fluence effects in the p$_0$ spectra during sO$_2$ estimation. According to initial results, our *in vivo* sO$_2$ estimates are physiologically more plausible when compared to linear spectral unmixing techniques.

2. Materials and Methods

A. Concept overview. With LSD-qPAI we approximate a function f to estimate sO$_2$ from initial pressure p$_0$ spectra S_{P_0} ($f: S_{P_0} \in \mathbb{R}^n \to sO_2 \in \mathbb{R}$). It is a data-driven method in which a neural network learns to compensate for different extents of *spectral coloring* within a given p$_0$ spectrum, where the term spectral coloring refers to changes in the spectrum at a given spatial location due to wavelength-dependent absorption in the surrounding tissue (15). To account for the lack of real data comprising reliable reference or even ground truth sO_2 values given p$_0$ recordings, we create a dataset of pixel-wise p$_0$ spectra with various degrees of spectral coloring obtained from Monte Carlo simulated *in silico* multispectral p$_0$ images (cf. Figure 1). The variety of possibilities for spectral coloring is simulated by extracting p$_0$ spectra from different spatial locations within the image (e.g. shallow or deep background structures and superficial of deep vascular structures). With the generation of a representative dataset, the network learns to account for spectral coloring when inferring sO_2 from input p$_0$ spectra.

A priori tissue assumption

↓

Multipectral p_0 simulation

λ_n

λ_{n-1}

λ_2
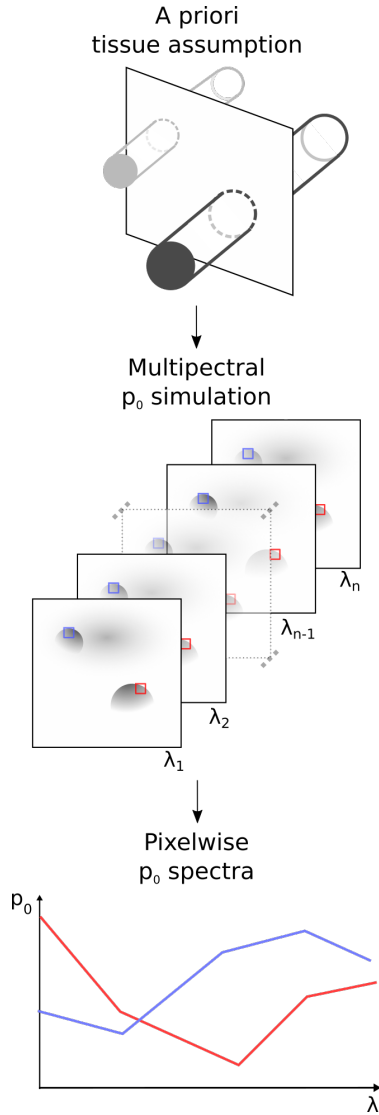
λ_1

↓

Pixelwise p_0 spectra

Fig. 1. Overview of the generation of p_0 spectra. An *in silico* tissue phantom with a ground truth tissue model is simulated over multiple wavelengths. The wavelength dependent behavior of the p_0 values in each pixel then defines the p_0 spectra.

During training, the algorithm is presented tuples (S_{p_0}, sO_2), with $S_{p_0} \in \mathbb{R}^n$ and $sO_2 \in \mathbb{R}$. Here, each spectrum is normalized such that $\sum_i^n p_{0\lambda_i} = 1$. When estimating oxygenation for recorded *in vivo* spectra these are normalized as well - sacrificing p_0 amplitude information to eliminate the need to calibrate the *in silico* p_0 training data to the target domain.

B. Prototype implementation. In the following paragraphs, we provide detailed descriptions of the prototype implementation of our approach, namely the simulation pipeline, the used deep learning model, and a linear spectral unmixing method.

Simulation pipeline. We create simple homogeneous tissue volumes comprising tubular vessel structures that run orthogonal to the imaging plane. We simulated the light transport in this medium with a Monte Carlo method and simulated each

of the *in silico* vessel phantoms with 26 wavelengths equidistant from 700 nm to 950 nm in 10 nm steps. For the Monte Carlo simulation, we used a multithreaded adaptation of the Monte Carlo framework *mcxyz* ([16]) with 10^7 photons for each simulation on a 0.6 mm grid.

Deep learning model. For reconstruction of sO_2 from S_{p_0}, we use a simple fully connected neural network architecture (cf. Figure 2). We implement the network with eight hidden layers with four times the size of the input layer using *pytorch* ([17]) and perform the experiments with the *trixi* framework ([18]). We use an $L1$ loss function, a learning rate of 10^{-4}, a batch size of 2000, with 1000 batches per epoch, and train the network for 25 epochs. The size of the input layers corresponds to the number of simulated or measured wavelengths (26 in this study) and we have a one dimensional output layer, which corresponds to the sO_2 estimation as the target parameter.
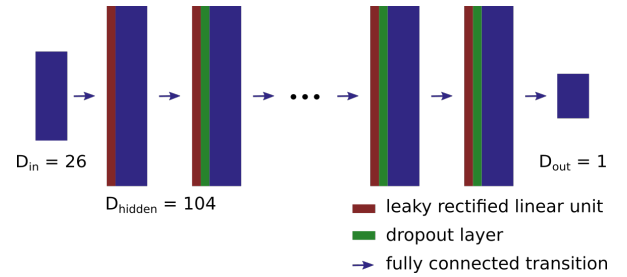

Fig. 2. Deep learning architecture for blood oxygenation (sO_2) reconstruction, comprising leaky rectified linear units (red), dropout layers (green), and layers of neurons (blue). In this setup, each of the neural layers is fully connected to the previous layer.

Linear spectral unmixing. We use a linear spectral unmixing algorithm as a reference for the *in vivo* imaging results. Specifically, we use the C++ *Eigen* ([19]) implementation of the QR householding matrix decomposition to unmix the recorded spectra for Hb and HbO$_2$ and calculate sO_2 from the ratio of these.

3. Experiments and Results

In the following section we outline the experiments we conducted for validation of the presented approach. The purpose of our experiments was two-fold: we first show the feasibility of our method with an *in silico* evaluation on a held-out set from the same distribution as the training data. Secondly, we conduct feasibility tests on two different *in vivo* datasets, of which the first contains PA images of an open porcine brain and the second dataset comprises PA images of the human forearm. These datasets are chosen because the compositions of relevant chromophores in tissue are very different in both cases. For both of these *in vivo* settings we also compute sO_2 with a linear spectral unmixing algorithm to provide a reference.

Simulation parameters. The key to the general applicability of the LSD-qPAI method is the simulation of a representative dataset of p_0 spectra. For this initial study, we created a total of 971 *in silico* phantoms containing 2 - 10 tubular vessel-mimicking structures in a homogeneous background at random

locations orthogonal to the imaging plane. For tissue mimicking *a priori* conditions, we assumed blood vessels to have a hemoglobin concentration of 150 g/dl ([20]), generic background tissue to have a blood volume fraction of 2%, and also consider an average of 5% fat and 80% water in this background tissue. The tubular vessel structures have a radius randomly drawn from a uniform distribution between 0.5 mm and 4 mm. Each vessel phantom was assigned a distinct constant blood oxygenation in vessel structures and the same constant blood oxygenation in the background. The tissue absorption coefficient was calculated for each voxel based on these assumptions and we set the reduced scattering coefficient to be constant over all wavelengths with $\mu'_s = 15\,\text{cm}^{-1}$.

In silico validation. We use 80% of the *in silico* dataset for training, 10% for supervision of the training process and hyperparameter optimization, and the remaining 10% as a test set to report the *in silico* results. We report the relative sO2 estimation error $e_{sO_2} = (\hat{sO_2} - sO_2)/sO_2$, where $\hat{sO_2}$ represents the estimated blood oxygen saturation and sO_2 represents the ground truth simulated blood oxygenation. All *in silico* estimation results for the test data are shown in Figure 3. Additionally, violin plots present the error distribution within each interval of ten percentage points (0 – 10%, 10 – 20%, etc). The median relative estimation error e_{sO_2} was 6.1% with an interquartile range of (2.4%, 18.7%).
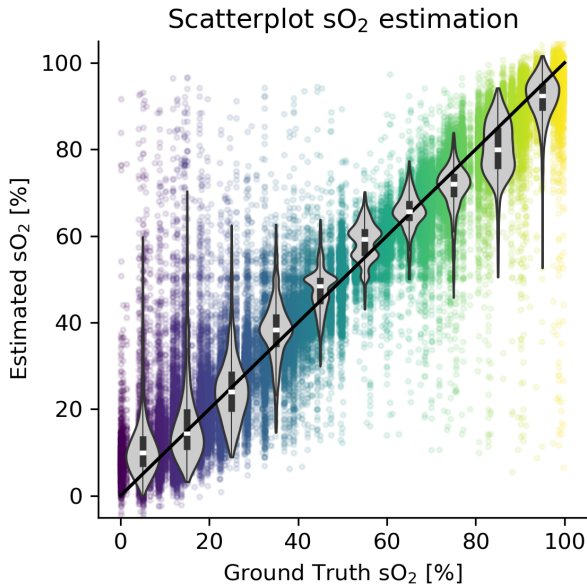

Fig. 3. Scatterplot of ground truth sO2 and $\hat{sO_2}$ estimated from the p_0 spectra with our algorithm. The bisector of the graph is indicated by a black line. In the violin plots, the black line represents the 25th and 75th percentile and the white box represents the median.

Imaging of porcine brain. As our first *in vivo* experiment, we applied our method to images of a porcine brain during open surgery. These images were recorded at the same wavelengths as in the training dataset. We evaluate a single series of images which were normalized by the recorded laser energy and reconstructed with the delay-and-sum algorithm using a hamming window. For the calculation of the mean oxygenation within

the ROI, only those point estimates were taken into consideration, where the signal at the isosbestic point of 800 nm was greater than a noise equivalent level.
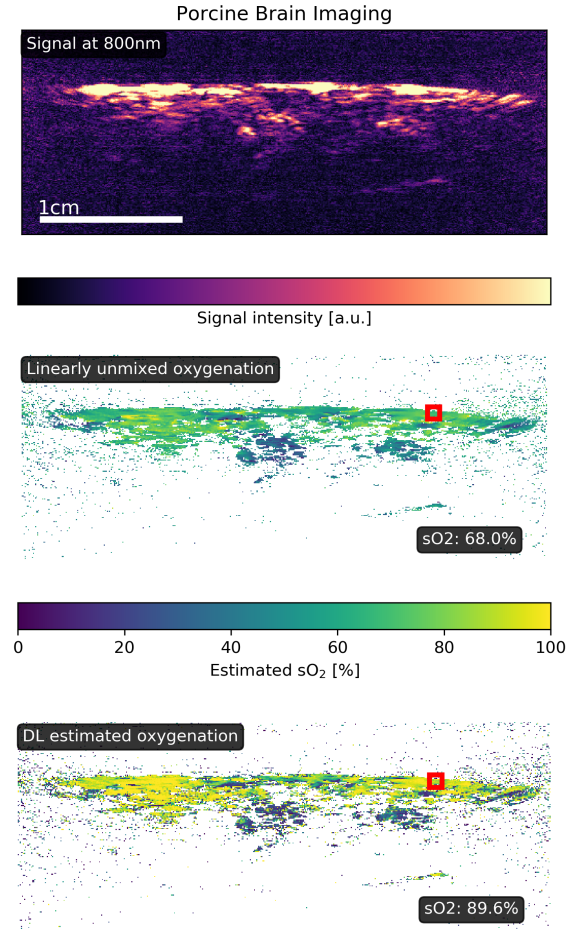
Fig. 4. Qualitative example of sO2 estimation derived from a multispectral PA image of a pig brain. The top image shows the signal at 800nm, the middle image shows the unmixing result using a linear spectral unmixing technique, and the bottom image shows the unmixing results with the proposed method. The red region of interest (ROI) shows a superficial region of highly oxygenated blood.

In the image, the red bounding box marks an area where blood with a high oxygenation was present (cf. Figure 4). Our method estimated a blood oxygenation of about 90% , whereas linear spectral unmixing using a QR decomposition yielded an estimate of 68% in the same area.

Imaging of human forearm. We also applied our method to *in vivo* images of a the forearm of a healthy human volunteer also with the same 26 wavelengths as used in the simulations. This imaging scenario was specifically chosen as an out-of-distribution test for the method. This is, because no well matching spectra should be contained in our training set, as we did not consider the presence of melanin in our simulation. We normalized each image by the laser energy and reconstructed the images with the delay-and-sum algorithm using a hamming window. To decrease the inter frame variability, we averaged over 10 consecutive frames of the same wavelength. Prior to

averaging we registered the images with an optical flow-based method to account for motion artifacts (21).

In the oxygenation images shown in Figure 5, the upper signal originating from the radial artery is chosen as the region of interest (ROI) and marked by a red bounding box. In this ROI, only those point estimates were taken into consideration for the averaged sO$_2$ result, where the signal at 800 nm was greater than a noise equivalent level. The arterial blood oxygenation as determined by our algorithm was about 98%, whereas spectral unmixing using a QR linear unmixing algorithm yielded a value of about 80%.
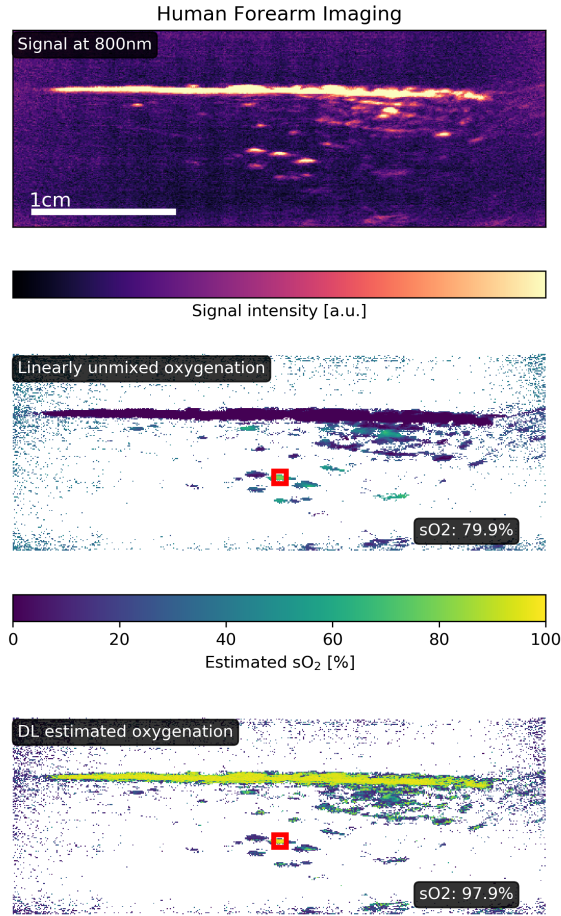

Fig. 5. Qualitative example of sO$_2$ estimation derived from a multispectral PA image of the forearm of healthy human volunteers. The red ROI shows the radial artery at a depth of about five millimeters. The top image shows the signal at 800nm, the middle image shows the unmixing result using a linear spectral unmixing technique, and the bottom image shows the unmixing results with the proposed method.

4. Discussion and Conclusion

In this work, we investigate the feasibility of inferring sO$_2$ from pixel-wise initial pressure spectra S_{p_0} using a deep learning model trained on simulated data. While a photoacoustic signal is proportional to the product of optical absorption μ_a and the light fluence ϕ, standard unmixing algorithms ignore the dependence on ϕ, which can potentially result in large errors, especially deep in tissue. To overcome this issue, we propose

the LSD-qPAI algorithm that learns a mapping function from pixel-wise multispectral initial pressure data to blood oxygenation. Our initial *in silico* results look promising, yielding a median sO$_2$ estimation error of 6% *in silico*. The LSD-qPAI method is potentially relevant especially for clinical imaging with hand-held PA scanners, as sO$_2$ estimations with high accuracy and robustness can potentially be computed in real time. This has been demonstrated in similar diffuse reflectance multispectral imaging applications (22).

In prior work, we achieved a comparable accuracy *in silico* when estimating the optical absorption coefficient (10, 12). However, in contrast to these methods, we now are also able to obtain plausible results *in vivo* when imaging an open pig brain. Here, the estimations of our method are closer to the expected arterial blood oxygenation values of healthy subjects (near 100% (23)). Especially in comparison to the results of classical linear unmixing, LSD-qPAI seems to provide physiologically more plausible estimations.

Our method utilizes a normalization of the simulated and recorded spectra, sacrificing p_0 amplitude information to eliminate the need to calibrate the *in silico* p_0 training data to the target domain. However, this also means that we discard one dimension of the feature vector, restricting the minimum amount of spectra needed to be able to reliably infer optical properties.

For the *in vivo* experiments it was to be expected that the recorded *in vivo* spectra of the brain images match our training distribution more closely compared to the forearm images. This is because light needs to penetrate through the skin in order to obtain images of the forearm, which contains melanin, a chromophore that was not included in the simulation framework. It can be seen that neither the proposed method nor linear unmixing can handle skin tissue well, estimating implausible and even impossible sO$_2$ results. Projecting the *in vivo* spectra to the first two principal components of the training data seems to confirm this hypothesis (cf. Fig. 6). In the figure it is apparent that most of the porcine spectra (colored in black) are contained within the support of the first two principal components of our simulation space, whereas this does not appear to be the case for the forearm spectra. In this context it should be noted that the first two principal components (computed on the training data) account for 95.4% of the variation in our dataset. The projection image illustrates that the distribution of the training data match the distribution of the test (in vivo) data more closely when imaging pig brain instead of human forearm.

When considering the large number of plausible tissue geometry and oxygenation configurations, the number of training samples used for this study was low. Also, no noise model was applied to the simulated spectra in addition to the simulation noise inherent to the Monte Carlo procedure. Hence, a thorough investigation of the influence of a realistic noise model on the spectra would be very interesting. Our a priori assumptions for the tissue parameters used in the simulation pipeline led to very difficult situations for the unmixing algorithm to resolve. For example, due to the 2 % blood volume fraction in the background, light fluence was the dominating factor even in shallow point absorbers - a behavior not usually observed in realistic scenarios, where less than 1% would be a more realistic assumption (20). Also, the simulation assumption that blood oxygenation is constant throughout the tissue is
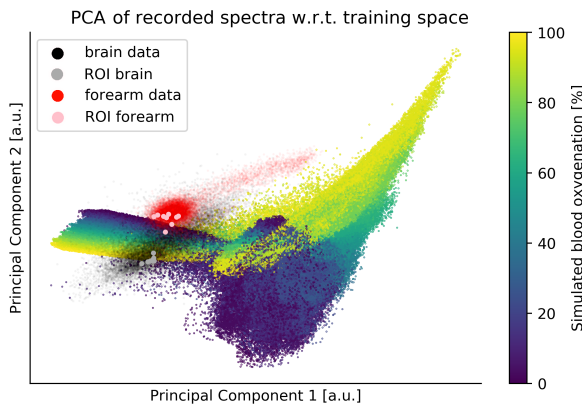
Fig. 6. Principal component analysis (PCA) of the *in vivo* recorded spectra of porcine brain tissue (black) and human forearm tissue (red). The samples of the regions of interest shown in Fig. 4 and Fig. 5 and shown in gray and pink respectively. The principal component projection of the training data is also color-coded with the associated oxygenation values.

not generally correct and more realistic variations on these assumptions should be considered in future work.

Overall, the presented initial results *in vivo* are very promising. However, a thorough and well-designed *in vivo* validation needs to be performed to deduce meaningful conclusions regarding the general applicability of the presented method. Such future studies should cover a much broader range of possible sO_2 values and include more realistic scenarios when assessing the unmixing accuracy. Future work should also include a comprehensive comparison of this method to state-of-the-art methods, such as eigenspectra multispectral optoacoustic tomography (eMSOT) (13), the end-to-end qPAI method presented by Cai et al. (11), as well as other linear and nonlinear spectral unmixing techniques (3, 24).

Acknowledgements

Author Contributions

Conceptualization, J.G., T.K., T.A., and L.M.-H.; Data curation, J.G. and T.K.; Formal analysis, J.G.; Funding acquisition, L.M.-H.; Investigation, T.K., T.A., and J.G.; Methodology, J.G. and T.K.; Project administration, L.M.-H.; Software, J.G.; Supervision, L.M.-H.; Validation, J.G. and T.K.; Visualization, J.G.; Method naming, T.K.; Writing—original draft, J.G.; and Writing—review and editing, J.G., T.K., T.A. and L.M.-H.

Bibliography

1. Cox, B., Laufer, J., and Beard, P., "The challenges for quantitative photoacoustic imaging," in [*Photons Plus Ultrasound: Imaging and Sensing 2009*], **7177**, 717713, International Society for Optics and Photonics (2009).

2. Wang, L. V. and Hu, S., "Photoacoustic tomography: in vivo imaging from organelles to organs," *science* **335**(6075), 1458–1462 (2012).

3. Li, M., Tang, Y., and Yao, J., "Photoacoustic tomography of blood oxygenation: A mini review," *Photoacoustics* (2018).

4. Maslov, K., Zhang, H. F., and Wang, L. V., "Effects of wavelength-dependent fluence attenuation on the noninvasive photoacoustic imaging of hemoglobin oxygen saturation in subcutaneous vasculature in vivo," *Inverse Problems* **23**(6), S113 (2007).

5. Bu, S., Liu, Z., Shiina, T., Kondo, K., Yamakawa, M., Fukutani, K., Someda, Y., and Asao, Y., "Model-based reconstruction integrated with fluence compensation for photoacoustic tomography," *IEEE Transactions on Biomedical Engineering* **59**(5), 1354–1363 (2012).

6. Zhao, L., Yang, M., Jiang, Y., and Li, C., "Optical fluence compensation for handheld photoacoustic probe: An in vivo human study case," *Journal of Innovative Optical Health Sciences* **10**(04), 1740002 (2017).

7. Vogt, W. C., Zhou, X., Andriani, R., Wear, K. A., Pfefer, T. J., and Garra, B. S., "Photoacoustic oximetry imaging performance evaluation using dynamic blood flow phantoms with tunable oxygen saturation," *Biomedical Optics Express* **10**(2), 449–464 (2019).

8. Cox, B. T., Arridge, S. R., Köstli, K. P., and Beard, P. C., "Two-dimensional quantitative photoacoustic image reconstruction of absorption distributions in scattering media by use of a simple iterative method," *Applied Optics* **45**(8), 1866–1875 (2006).

9. Laufer, J., Delpy, D., Elwell, C., and Beard, P., "Quantitative spatially resolved measurement of tissue chromophore concentrations using photoacoustic spectroscopy: application to the measurement of blood oxygenation and haemoglobin concentration," *Physics in Medicine & Biology* **52**(1), 141 (2006).

10. Kirchner, T., Gröhl, J., and Maier-Hein, L., "Context encoding enables machine learning-based quantitative photoacoustics," *Journal of biomedical optics* **23**(5), 056008 (2018).

11. Cai, C., Deng, K., Ma, C., and Luo, J., "End-to-end deep neural network for optical inversion in quantitative photoacoustic imaging," *Optics letters* **43**(12), 2752–2755 (2018).

12. Gröhl, J., Kirchner, T., Adler, T., and Maier-Hein, L., "Confidence estimation for machine learning-based quantitative photoacoustics," *Journal of Imaging* **4**(12), 147 (2018).

13. Tzoumas, S., Nunes, A., Olefir, I., Stangl, S., Symvoulidis, P., Glasl, S., Bayer, C., Multhoff, G., and Ntziachristos, V., "Eigenspectra optoacoustic tomography achieves quantitative blood oxygenation imaging deep in tissues," *Nature communications* **7**, ncomms12121 (2016).

14. Brochu, F. M., Brunker, J., Joseph, J., Tomaszewski, M. R., Morscher, S., and Bohndiek, S. E., "Towards quantitative evaluation of tissue absorption coefficients using light fluence correction in optoacoustic tomography," *IEEE transactions on medical imaging* **36**(1), 322–331 (2017).

15. Tzoumas, S., Deliolanis, N., Morscher, S., and Ntziachristos, V., "Unmixing molecular agents from absorbing tissue in multispectral optoacoustic tomography," *IEEE transactions on medical imaging* **33**(1), 48–60 (2014).

16. Jacques, S. L., "Coupling 3d monte carlo light transport in optically heterogeneous tissues to photoacoustic signal generation," *Photoacoustics* **2**(4), 137–142 (2014).

17. Paszke, A., Gross, S., Chintala, S., Chanan, G., Yang, E., DeVito, Z., Lin, Z., Desmaison, A., Antiga, L., and Lerer, A., "Automatic differentiation in pytorch," (2017).

18. Zimmerer, D., Petersen, J., Koehler, G., Wasserthal, J., Adler, T., and Wirkert, A., "MIC-DKFZ/trixi," (2018).

19. Guennebaud, G., Jacob, B., et al., "Eigen v3." http://eigen.tuxfamily.org (2010).

20. Jacques, S. L., "Optical properties of biological tissues: a review," *Physics in Medicine & Biology* **58**(11), R37 (2013).

21. Kirchner, T., Gröhl, J., Sattler, F., Bischoff, M. S., Laha, A., Nolden, M., and Maier-Hein, L., "An open-source software platform for translational photoacoustic research and its application to motion-corrected blood oxygenation estimation," *arXiv preprint arXiv:1901.09781* (2019).

22. Wirkert, S. J., Kenngott, H., Mayer, B., Mietkowski, P., Wagner, M., Sauer, P., Clancy, N. T., Elson, D. S., and Maier-Hein, L., "Robust near real-time estimation of physiological parameters from megapixel multispectral images with inverse monte carlo and random forest regression," *International journal of computer assisted radiology and surgery* **11**(6), 909–917 (2016).

23. Zander, R., "The oxygen status of arterial human blood," *Scandinavian Journal of Clinical and Laboratory Investigation* **50**(sup203), 187–196 (1990).

24. Keshava, N. and Mustard, J. F., "Spectral unmixing," *IEEE signal processing magazine* **19**(1), 44–57 (2002).

APPLICATION

C3

PHOTOACOUSTIC MONITORING OF BLOOD OXYGENATION DURING NEUROSURGICAL INTERVENTIONS

This manuscript investigates the applicability multispectral PAI and more specifically of our imaging system, to imaging sO_2 in a large mammal (gyrencephalic) brain. Specifically it investigates the sO_2 estimation results obtained with a range of linear spectral unmixing techniques. A hypoxia experiment on a craniotomized pig is performed.

Own contribution

The initial manuscript was drafted by me together with Niklas Holzwart and edited and revised by all authors.

I conceived of the imaging setup in discussion with our neurosurgical partners, chiefly Edgar Santos. The experiment was designed in discussion with all the authors. I performed the technical aspects of the experiment assisted by Janek Gröhl, while Mildred Herrera, Adrián Aguilera and Edgar Santos performed the surgery and handled the animal. Niklas Holzwart comparably re-implemented the various spectral unmixing approaches in MITK. I performed post-processing and analysis of the data together with Niklas Holzwart. Edgar Santos supervised the neurosurgical aspects of the work, Lena Maier-Hein supervised the technical aspects of the project.

Photoacoustic monitoring of blood oxygenation during neurosurgical interventions

Thomas Kirchner [a,b], Janek Gröhl [a,c], Niklas Holzwarth [a,b], Mildred A. Herrera [d], Adrián Hernández-Aguilera [d], Edgar Santos [d], and Lena Maier-Hein [a,c]

[a] Division of Computer Assisted Medical Interventions (CAMI), German Cancer Research Center (DKFZ), Heidelberg, Germany
[b] Faculty of Physics and Astronomy, Heidelberg University, Heidelberg, Germany
[c] Medical Faculty, Heidelberg University, Heidelberg, Germany
[d] Department of Neurosurgery, Heidelberg University Hospital, Heidelberg, Germany

ABSTRACT

Multispectral photoacoustic (PA) imaging is a prime modality to monitor hemodynamics and changes in blood oxygenation (sO_2). Although sO_2 changes can be an indicator of brain activity both in normal and in pathological conditions, PA imaging of the brain has mainly focused on small animal models with lissencephalic brains. Therefore, the purpose of this work was to investigate the usefulness of multispectral PA imaging in assessing sO_2 in a gyrencephalic brain. To this end, we continuously imaged a porcine brain as part of an open neurosurgical intervention with a handheld PA and ultrasonic (US) imaging system *in vivo*. Throughout the experiment, we varied respiratory oxygen and continuously measured arterial blood gases. The arterial blood oxygenation (SaO_2) values derived by the blood gas analyzer were used as a reference to compare the performance of linear spectral unmixing algorithms in this scenario. According to our experiment, PA imaging can be used to monitor sO_2 in the porcine cerebral cortex. While linear spectral unmixing algorithms are well-suited for detecting changes in oxygenation, there are limits with respect to the accurate quantification of sO_2, especially in depth. Overall, we conclude that multispectral PA imaging can potentially be a valuable tool for change detection of sO_2 in the cerebral cortex of a gyrencephalic brain. The spectral unmixing algorithms investigated in this work will be made publicly available as part of the open-source software platform Medical Imaging Interaction Toolkit (MITK).

Keywords: Photoacoustics, Neurosurgery, Blood oxygenation, Brain imaging, Translational research

1. INTRODUCTION

A major application of photoacoustic (PA) imaging is the monitoring of hemodynamics and changes in blood oxygenation (sO_2),[1] which are indicators of brain activity[2,3] or injury.[4] In clinical practice, techniques for the monitoring of brain injury can vary widely with the specific application. While there are various techniques that can image hemodynamics, PA imaging can potentially provide better functional information and higher resolution.[5] sO_2 is usually calculated via the estimation of abundances of oxygenated and deoxygenated hemoglobin chromophores.[6] In multispectral PA imaging, this concentration estimation is generally done by linear spectral unmixing (SU),[7–9] which involves solving a set of linear equations for the desired abundances of hemoglobin.[10] While PA imaging is widely used in small animal models with lissencephalic brains, larger and more complex brains remain challenging.[5] The purpose of this work was therefore to investigate the usefulness of multispectral PA imaging in assessing sO_2 in a gyrencephalic brain.

Please address your correspondence to Thomas Kirchner, e-mail: t.kirchner@dkfz-heidelberg.de

2. MATERIAL AND METHODS

To investigate the performance of sO$_2$ estimation by SU *in vivo* in a neurosurgical setting, we performed PA measurements during an open intervention on a porcine brain, which allowed us to image without the acoustic attenuation of the skull. In this setting, we were also able to take corresponding arterial blood gas (ABG)[11] measurements and thus to compare the quantitative sO$_2$ estimation performance of numerical algorithms for SU,[12] against a physiological arterial blood oxygenation (SaO$_2$) reference value.

Experimental setup

The PA imaging modality used in this study was a custom hybrid PA and ultrasonic (US) system with a fast-tunable optical parametric oscillator (OPO) laser system (Phocus Mobile, Opotek, Carlsbad, USA) and a 7.5 MHz linear US transducer with 128 elements (L7-Xtech, Vernon, Tours, France), on a DiPhAs ultrasonic research platform (Fraunhofer IBMT, St. Ingbert, Germany).[13] The custom probe holder covered the transducer with a gold leaf to reduce transducer absorption artifacts. For optimal contrast to noise,[14] the PA images were recorded at 760 nm and 858 nm, adding 798 nm as an isosbestic reference.

A porcine brain was continuously imaged for 45 min, as part of an open neurosurgical intervention with our hybrid PA and US probe. Our experiment was carried out following a craniotomy on a three month old female domestic pig. As illustrated in Figure 1a, the probe was fixed over the left hemisphere of the brain to record a sagittal slice, using a gel pad as acoustic coupling. During imaging, the ventilation of the animal was varied and SaO$_2$ and reference measurements with an ABG analyzer were taken. The ventilation changes and reference measurements are detailed in Figure 2 and Table 1. In addition, SaO$_2$ was monitored non-invasively with a pulse oximeter[15] placed on the left earlobe.
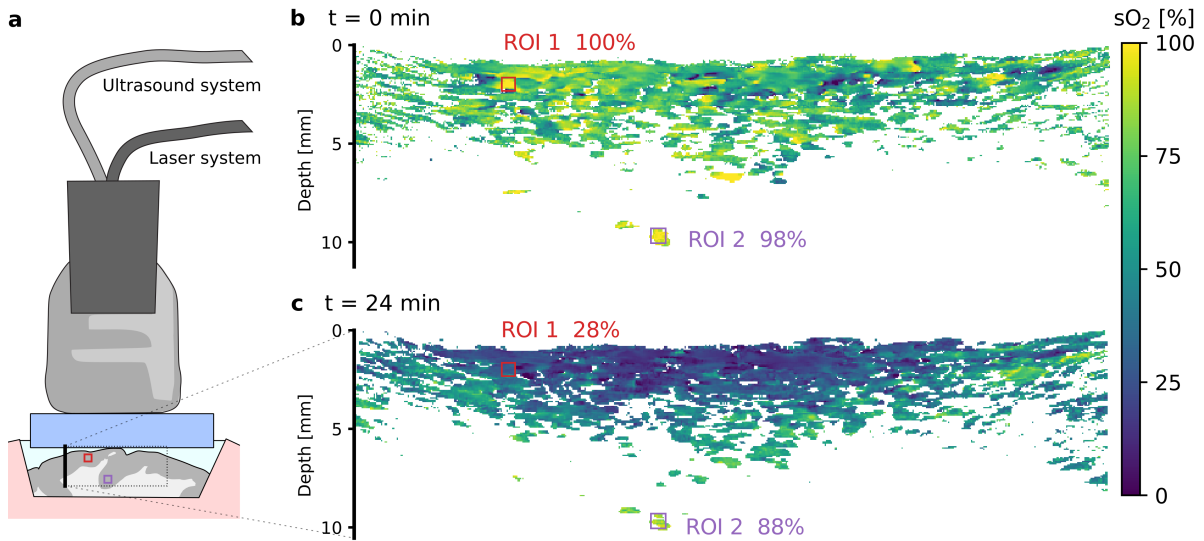
Figure 1. **(a)** Experimental setup. The photoacoustic (PA) probe was used to record sagittal images of a porcine brain. The field of view contains two regions of interest (ROIs) corresponding to arteries near (ROI 1 – red) and far (ROI 2 – purple) from the brain surface. **(b) & (c)** Example images of blood oxygenation (sO$_2$) in a brain slice. The ROIs are annotated with their corresponding median sO$_2$ value as determined with the Householder QR unmixing algorithm. t is the time from start of the experiment. In both sO$_2$ images, values under a noise equivalent threshold of unmixed total hemoglobin were masked. In **(b)** the respiratory oxygen (rO$_2$) was 35 % and arterial blood gas (ABG) analysis yielded an arterial blood oxygenation (SaO$_2$) of 100 %, while in **(c)** rO$_2$ was 0 % with SaO$_2$ = 26.2 %.

Image processing

Using the Medical Interaction Toolkit (MITK)[16] PA image processing plugin,[17] the raw PA data was beamformed with delay and sum[18,19] and von Hann apodization. The resulting images were motion corrected with the corresponding US B-mode images. All input images were averaged over ten recordings per wavelength before linear SU, which was performed on the PA images with five commonly used linear algorithms.[20] To cover a wide range of algorithms, we selected a QR decomposition with Householder transformation,[21] a LU (with full pivoting)[22] and a singular value decomposition[23] all from the C++ *Eigen*[24] library, as well as a weighted[25] (based on QR decomposition) and a non-negative (using least angle regression[26]) least square algorithm both from the C++ *Vigra*[27] library.

For quantitative validation of the SU algorithms, we selected two regions of interest (ROIs), for which we determined sO_2 values. We selected a surface ROI and a deep one to investigate the influence of fluence effects[28] on SU sO_2 estimation. We assumed that both ROIs contain arteries, as they had generally high PA signal and distinct characteristic pulsing in the US and PA image streams. The resulting sO_2 values for one ROI are the median of all pixels within that ROI that have a higher than noise equivalent total hemoglobin level.

3. RESULTS AND DISCUSSION

According to our results in Table 1, the different SU algorithms were similar in estimation performance, with the exception of the non-negative least square boundary effect. While other algorithms can yield physiologically impossible sO_2 values (even above 100 %, and theoretically also below 0 %), the non-negativity constraint artificially prevents this. This was especially relevant for the evaluation of changes in ROI 2. All other differences between the algorithms are within their respective standard deviations. The Householder QR algorithm performed the fastest. In the following, we therefore only present the SU results of the QR algorithm. Example slices are shown in Figure 1b&c with the marked ROIs and their corresponding median sO_2 value.
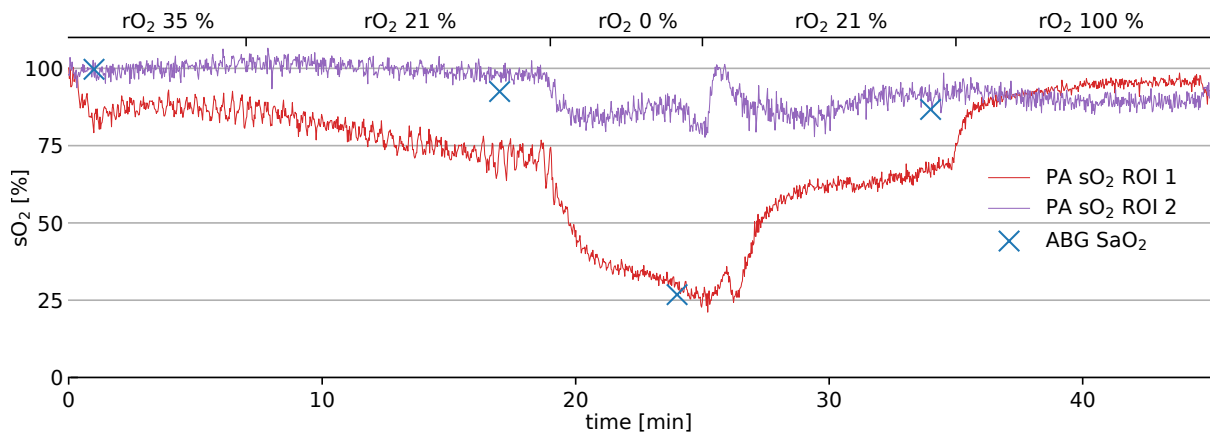
Figure 2. Photoacoustic blood oxygenation (sO_2) estimation over time in two regions of interest (ROIs) (see Figure 1). The different levels of respiratory oxygen (rO_2) delivered by the ventilation are displayed above the plot; the arterial blood gas (ABG) reference measurements of arterial blood oxygenation (SaO_2) as blue crosses.

Comparing the changes in ventilation with the time course characteristics of the unmixing results of ROI 1 in Figure 2, one can see that linear SU can be used for change detection of sO_2 in the cerebral cortex. However, the unmixing results do not closely follow the quantitative values of the ABG reference (Table 1). This illustrates the limits in quantification of sO_2 with PA imaging and is even more obvious in deep tissue, considering the small changes in sO_2 estimation for ROI 2.

In conclusion, our study suggests that PA imaging can be used to monitor sO_2 changes in the cerebral cortex during neurosurgical interventions. However, care must be taken when interpreting sO_2 estimation results due to the limits in quantitative accuracy when using linear SU algorithms. This is especially relevant in deep tissue

time	rO$_2$	SaO$_2$ [%]		QR/SVD sO$_2$ [%]		LU sO$_2$ [%]		NNLS sO$_2$ [%]		WLS sO$_2$ [%]	
[min]	[%]	ABG	PuOx	ROI 1	ROI 2	ROI 1	ROI 2	ROI 1	ROI 2	ROI 1	ROI 2
+1	35	100	99	85 ± 2	99 ± 2	85 ± 2	98 ± 2	85 ± 2	98 ± 2	85 ± 2	98 ± 2
+16	21	93	88-92	72 ± 3	98 ± 2	72 ± 4	98 ± 2	72 ± 3	98 ± 1	72 ± 3	98 ± 2
+24	0	26	40	27 ± 2	84 ± 3	26 ± 2	83 ± 4	27 ± 2	84 ± 3	27 ± 2	84 ± 3
+34	21	86	–	69 ± 2	91 ± 3	69 ± 2	91 ± 3	69 ± 2	91 ± 3	69 ± 2	91 ± 3
+45	100	–	100	95 ± 2	91 ± 2	95 ± 2	90 ± 2	95 ± 2	91 ± 2	95 ± 2	90 ± 2

Table 1. Comparison of the arterial blood gas (ABG), pulse oximetry (PuOx) and five spectral unmixing (SU) estimations – in region of interest (ROI) 1 & 2. Values are averaged over one minute beginning at the time after start of the recording. The respiratory oxygen (rO$_2$) value was adjusted at least five minutes before the recording (see Figure 2). SVD: singular value decomposition, NNLS: non-negative least squares, WLS: weighted least squares. –: Missing values failed to record due to technical issues.

due to fluence dependent spectral coloring. While there are promising approaches to address these fluence effects in general[29–31] and spectral coloring specifically,[28] the translation of quantitative PA imaging deep in tissue remains a major challenge.

REFERENCES

[1] Wang, L. V. and Hu, S., "Photoacoustic tomography: in vivo imaging from organelles to organs," *science* **335**(6075), 1458–1462 (2012).

[2] Fransson, P., "Spontaneous low-frequency bold signal fluctuations: An fmri investigation of the resting-state default mode of brain function hypothesis," *Human brain mapping* **26**(1), 15–29 (2005).

[3] Raichle, M. E., MacLeod, A. M., Snyder, A. Z., Powers, W. J., Gusnard, D. A., and Shulman, G. L., "A default mode of brain function," *Proceedings of the National Academy of Sciences* **98**(2), 676–682 (2001).

[4] Takano, T., Tian, G.-F., Peng, W., Lou, N., Lovatt, D., Hansen, A. J., Kasischke, K. A., and Nedergaard, M., "Cortical spreading depression causes and coincides with tissue hypoxia," *Nature neuroscience* **10**(6), 754 (2007).

[5] Yao, J. and Wang, L. V., "Photoacoustic brain imaging: from microscopic to macroscopic scales," *Neurophotonics* **1**(1), 011003 (2014).

[6] Jobsis, F. F., "Noninvasive, infrared monitoring of cerebral and myocardial oxygen sufficiency and circulatory parameters," *Science* **198**(4323), 1264–1267 (1977).

[7] Keshava, N. and Mustard, J. F., "Spectral unmixing," *IEEE signal processing magazine* **19**(1), 44–57 (2002).

[8] Li, M.-L., Oh, J.-T., Xie, X., Ku, G., Wang, W., Li, C., Lungu, G., Stoica, G., and Wang, L. V., "Simultaneous molecular and hypoxia imaging of brain tumors in vivo using spectroscopic photoacoustic tomography," *Proceedings of the IEEE* **96**(3), 481–489 (2008).

[9] Gerling, M., Zhao, Y., Nania, S., Norberg, K. J., Verbeke, C. S., Englert, B., Kuiper, R. V., Bergström, Å., Hassan, M., Neesse, A., et al., "Real-time assessment of tissue hypoxia in vivo with combined photoacoustics and high-frequency ultrasound," *Theranostics* **4**(6), 604 (2014).

[10] Chance, B., Leigh, J., Miyake, H., Smith, D., Nioka, S., Greenfeld, R., Finander, M., Kaufmann, K., Levy, W., and Young, M., "Comparison of time-resolved and-unresolved measurements of deoxyhemoglobin in brain," *Proceedings of the National Academy of Sciences* **85**(14), 4971–4975 (1988).

[11] McFadden Jr, E. and Lyons, H. A., "Arterial-blood gas tension in asthma," *New England Journal of Medicine* **278**(19), 1027–1032 (1968).

[12] Tzoumas, S., Deliolanis, N., Morscher, S., and Ntziachristos, V., "Unmixing molecular agents from absorbing tissue in multispectral optoacoustic tomography," *IEEE transactions on medical imaging* **33**(1), 48–60 (2014).

[13] Kirchner, T., Wild, E., Maier-Hein, K. H., and Maier-Hein, L., "Freehand photoacoustic tomography for 3d angiography using local gradient information," *Photons Plus Ultrasound: Imaging and Sensing 2016* **9708**, 97083G, International Society for Optics and Photonics (2016).

[14] Luke, G. P., Nam, S. Y., and Emelianov, S. Y., "Optical wavelength selection for improved spectroscopic photoacoustic imaging," *Photoacoustics* **1**(2), 36–42 (2013).

[15] Tremper, K. K., "Pulse oximetry," *Chest* **95**(4), 713–715 (1989).

[16] Nolden, M., Zelzer, S., Seitel, A., Wald, D., Müller, M., Franz, A. M., Maleike, D., Fangerau, M., Baumhauer, M., Maier-Hein, L., et al., "The medical imaging interaction toolkit: challenges and advances," *International journal of computer assisted radiology and surgery* **8**(4), 607–620 (2013).

[17] Kirchner, T., Sattler, F., Gröhl, J., and Maier-Hein, L., "Signed real-time delay multiply and sum beamforming for multispectral photoacoustic imaging," *Journal of Imaging* **4**(10), 121 (2018).

[18] Griffiths, L. and Jim, C., "An alternative approach to linearly constrained adaptive beamforming," *IEEE Transactions on antennas and propagation* **30**(1), 27–34 (1982).

[19] Kim, J., Park, S., Jung, Y., Chang, S., Park, J., Zhang, Y., Lovell, J. F., and Kim, C., "Programmable real-time clinical photoacoustic and ultrasound imaging system," *Scientific reports* **6**, 35137 (2016).

[20] Burden, R. L., Faires, J. D., and Reynolds, A. C., "Numerical analysis," (2001).

[21] Goodall, C. R., [*13 Computation using the QR decomposition*], Elsevier (1993).

[22] Adomian, G., "A review of the decomposition method in applied mathematics," *Journal of mathematical analysis and applications* **135**(2), 501–544 (1988).

[23] Boardman, J. W., "Inversion of imaging spectrometry data using singular value decomposition," (1989).

[24] Guennebaud, G., Jacob, B., Avery, P., Bachrach, A., Barthelemy, S., et al., "Eigen v3," (2010).

[25] Shimabukuro, Y. E. and Smith, J. A., "The least-squares mixing models to generate fraction images derived from remote sensing multispectral data," *IEEE Transactions on Geoscience and Remote sensing* **29**(1), 16–20 (1991).

[26] Efron, B., Hastie, T., Johnstone, I., Tibshirani, R., et al., "Least angle regression," *The Annals of statistics* **32**(2), 407–499 (2004).

[27] Köthe, U., "Vision with generic algorithms (vigra)." https://ukoethe.github.io/vigra/ (2018).

[28] Tzoumas, S., Nunes, A., Olefir, I., Stangl, S., Symvoulidis, P., Glasl, S., Bayer, C., Multhoff, G., and Ntziachristos, V., "Eigenspectra optoacoustic tomography achieves quantitative blood oxygenation imaging deep in tissues," *Nature communications* **7**, ncomms12121 (2016).

[29] Kirchner, T., Gröhl, J., and Maier-Hein, L., "Context encoding enables machine learning-based quantitative photoacoustics," *Journal of biomedical optics* **23**(5), 056008 (2018).

[30] Hänninen, N., Pulkkinen, A., and Tarvainen, T., "Image reconstruction with reliability assessment in quantitative photoacoustic tomography," *Journal of Imaging* **4**(12), 148 (2018).

[31] Gröhl, J., Kirchner, T., Adler, T., and Maier-Hein, L., "Confidence estimation for machine learning-based quantitative photoacoustics," *Journal of Imaging* **4**(12), 147 (2018).

J4

PHOTOACOUSTICS CAN IMAGE SPREADING DEPOLARIZATION DEEP IN GYRENCEPHALIC BRAIN

This manuscript shows that photoacoustics can image the hemodynamics of spreading depolarization deep in the cortex of a large mammal (gyrencephalic) brain. Before this work, imaging of spreading depolarization in depth was only possible in poorer contrast lower resolution fMRI.

Own contribution

The initial manuscript was drafted by me and edited and revised by all authors.

I conceived of the study in discussion with our neurosurgical partner Edgar Santos. The experiments were designed by me, in discussion with all authors. I performed the technical aspects of the experiment assisted by Janek Gröhl and Tim Adler, while Mildred Herrera, Adrián Aguilera and Edgar Santos performed the surgeries and handled the animals. I performed post-processing and analysis with assistance by Janek Gröhl and Tim Adler. Edgar Santos supervised the neurosurgical aspects of the work. Lena Maier-Hein supervised the technical aspects of the project.

Photoacoustics can image spreading depolarization deep in gyrencephalic brain

Thomas Kirchner [1,2,*], Janek Gröhl [1,3], Mildred A. Herrera [4], Tim Adler [1,5], Adrián Hernández-Aguilera [4], Edgar Santos [4], Lena Maier-Hein [1,3,‡]

1 Division of Computer Assisted Medical Interventions, German Cancer Research Center, Heidelberg, Germany.
2 Faculty of Physics and Astronomy, Heidelberg University, Heidelberg, Germany.
3 Medical Faculty, Heidelberg University, Heidelberg, Germany.
4 Department of Neurosurgery, Heidelberg University Hospital, Heidelberg, Germany.
5 Faculty of Mathematics and Computer Science, Heidelberg University, Heidelberg, Germany.

* t.kirchner@dkfz-heidelberg.de

‡ l.maier-hein@dkfz-heidelberg.de

Abstract

Spreading depolarization (SD) is a self-propagating wave of near-complete neuronal depolarization that is abundant in a wide range of neurological conditions, including stroke. SD was only recently documented in humans and is now considered a therapeutic target for brain injury, but the mechanisms related to SD in complex brains are not well understood. While there are numerous approaches to interventional imaging of SD on the exposed brain surface, measuring SD deep in brain is so far only possible with low spatiotemporal resolution and poor contrast. Here, we show that photoacoustic imaging enables the study of SD and its hemodynamics deep in the gyrencephalic brain with high spatiotemporal resolution. As rapid neuronal depolarization causes tissue hypoxia, we achieve this by continuously estimating blood oxygenation with an intraoperative hybrid photoacoustic and ultrasonic (PAUS) imaging system. Due to its high resolution, promising imaging depth and high contrast, this novel approach to SD imaging can yield new insights into SD and thereby lead to advances in stroke, and brain injury research.

Main

Spreading depolarization (SD) is a self-propagating wave of near-complete neuronal depolarization that occurs abundantly [1] in individuals with progressive neuronal injury after stroke [2] and traumatic brain injury [3] as well as subarachnoid hemorrhage [4], intracerebral hemorrhage [5], and migraine with aura [6, 7]. Sixty years after the discovery of SD [8], many mechanisms related to SD have still not fully been understood while recent research increasingly finds SDs to be a therapeutic target in injured brain [9, 10].

In order to increase understanding of SD, the morphologies of their wave fronts have been a subject of intense study [11–13]. In these, the gyrencephalic brain has been found to be capable of irregular SD propagation

patterns [13,14] not found in lissencephalic brain. It remains to be studied if and how these patterns occur and evolve in depth. A better classification of the morphologies of these wave fronts could lead to a clear definition of a therapeutic target beyond mere occurrence of SD. The methods used to study SD can be classified in electrophysiological and optical approaches. The current clinical state of the art for monitoring SD is electrocorticography (ECoG) using subdural electrodes placed directly on the cortex [15,16] to record electrical activity. Because SDs propagate far from their point of origin, placing ECoG electrodes allows for remote monitoring of various brain injury. Characteristic patterns usually appear delayed for adjacent electrodes, with an SD registering as a large near direct current (DC) shift in the electrodes signal, followed by persistent depression of spontaneous cortical activity registering as higher frequency alternating current (AC) signal components [15]. While ECoG is clinical practice for surface measurements, implanting electrodes deep into the brain is the prime method of investigating SD beyond the brain surface. Doing so, SDs have been shown to occur in deep structures of the lissencephalic brain and in the brainstem, where they have been associated with sudden unexpected death in epilepsy [17]. How an SD, which originates on the cortex spreads to deep structures without direct gray matter connection is unclear as the use of electrical monitoring does not yield sufficient spatial information.

While optical techniques are not in routine clinical use, a range of them are used to study SD. They can yield high spatiotemporal resolution information usually related to the hemodynamic response to SD. These techniques include two photon microscopy (TPM) [12,18–20], laser speckle (LS) imaging [11,21,22], intrinsic optical signal (IOS) imaging [13,23,24] and near infrared spectroscopy (NIRS) [25–27]. TPM has an exceptional, single cell spatial resolution using the fluorescence of reduced nicotinamide adenine dinucleotide (NADH) as contrast. It can achieve a temporal resolution in a seconds range for a sub-millimeter imaging field [12] and has a sub-millimeter penetration depth. TPM is therefore mostly used in small animal models. LS imaging or LS flowmetry images changes in cerebral blood flow in single vessels [22]. It is complementary to the larger field of view IOS imaging [21] which images reflectance changes of light in one [24] or two [23] narrow bands. IOS has approximately one second temporal resolution and micron spatial resolution, while again being diffusion limited to a sub-millimeter penetration depth and no depth resolution. NIRS, in contrast to the other optical techniques, is no imaging technique but employs point measurement probes [25] or optrode strips [26] to monitor millimeter scale areas similar to electrodes. Like IOS, it indirectly measures reflectances correlated to relative concentration changes of the chromophores oxyhemoglobin (HbO) and deoxyhemoglobin (Hb), but its signal response is integrated over the area under the probe, leading to single spot measurements and no spatial resolution.

Functional magnetic resonance imaging (fMRI) with blood oxygen level dependent (BOLD) or diffusion weighted contrasts is the only modality that has been used to image the hemodynamic response of SD deep in brain [7]. Substantial drawbacks besides the complex imaging setup are the poor spatiotemporal resolution [28,29] and low contrast [7] when compared to optical or electrical measurements.

Overall, it can be concluded that the imaging methods proposed to date either feature high spatiotemporal resolution (IOS, TPM, LS) or are capable to provide depth-resolved information on SD beyond the surface (fMRI, implanted electrodes), but cannot provide both. To address this bottleneck, we investigate photoacoustic (PA) imaging as a possible high-resolution imaging technique for measuring SD deep in the gyrencephalic

brain. Near infrared (NIR) light can penetrate deep into tissue, is scattered and gets diffused, thereby losing spatial information after a fraction of a millimeter. Photoacoustics [30] is capable of imaging beyond this sub-millimeter optical diffusion limit through the PA effect [31]; light is delivered as a nanosecond laser pulse and where it is absorbed, it causes sudden thermoelastic expansion which in turn gives rise to acoustic waves. The ultrasonic spectral component of these waves emitted by the PA effect scatter much less than NIR light in tissue and can be detected by ultrasound (US) probes. Reconstructing their origin yields PA images. A multispectral stack of such images can be processed to reconstruct images of estimated tissue oxygenation that feature the spatiotemporal resolution and imaging depth of US combined with the optical contrast of NIRS. Multispectral photoacoustic imaging has shown to image blood oxygenation and perfusion in a variety of applications [32–36]. In the context of brain imaging, however, the application of PA has been restricted to lissencephalic brains [29] and its potential for monitoring SD remains to be investigated.

Rapid neuronal depolarization and repolarization causes tissue hypoxia [12]. Therefore, our work is based on the assumption that the imaging of hemodynamic changes with photoacoustics enables the monitoring of SD deep inside the tissue. We hypothesize that multispectral PA imaging is able to image SD induced hemodynamic changes in the entirety of the cortical gray matter of a gyrencephalic brain. For the purposes of this study, we measure an estimation of blood oxygenation (sO_2) and total hemoglobin (THb). Our imaging concept, which is illustrated in Fig. 1, relies on a hybrid photoacoustic ultrasonic (PAUS) imaging system which combines (1) an US research system featuring a linear US transducer with a center frequency of $7.5\,\mathrm{MHz}$ and broad acoustic response [37] with (2) a near infrared (NIR) fast tuning optical parametric oscillator (OPO) laser [38] (see Methods). The system operates in an interleaved PAUS imaging mode, acquiring multispectral PA sequences with corresponding US images for each PA image. This concurrent US imaging is used as anatomical reference for the physician (e.g. as guidance for the stimulation) and for motion compensation of the PA data (see Methods). Each multispectral PA image stack is converted into an image of estimated sO_2 and by spectral unmixing.
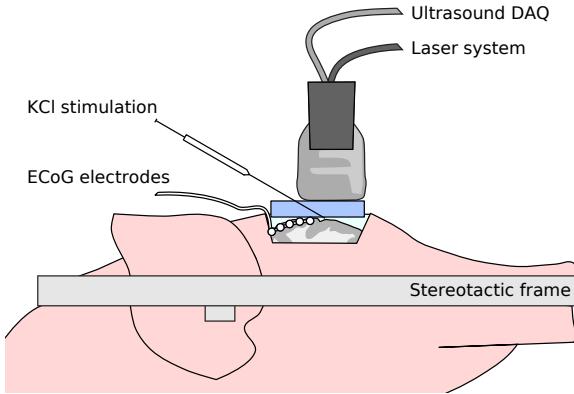

Figure 1. Setup for characterizing spreading depolarization (SD) deep inside the gyrencephalic brain with a hybrid photoacoustic ultrasonic (PAUS) imaging system. The PAUS probe is placed on a gel pad to allow for PAUS-guided potassium chloride (KCl) stimulation in the imaging plane. Electrocorticography (ECoG) recordings serve as a clinical reference.

Experiments & Results

Two experiments were performed with our PAUS system to investigate whether the monitoring of tissue oxygenation with PA enables the detection and monitoring of SDs in the entire depth of the cortical gray matter of a gyrencephalic brain. In both experiments, brain activity was monitored with ECoG using a standard subdural electrode strip (Fig. 1).

The aim of the *initial wave experiment* was to investigate if the hemodynamic response of the brain to an induced SD can be imaged with multispectral PA. We performed the experiment in an uninjured brain. To analyze tissue hemodynamics before, during and after the occurence of SD, we took continuous PAUS measurements starting 24 min before the the first potassium chloride (KCl) stimulation (see Fig. 1) and ending one hour after the stimulation. After the experiment we cut sagittal surgical slices from the extracted brain to relate the acquired PA and US images to the brain morphology as seen on the exposed tissue. As shown in Fig. 2 we were able to image PA signal up to a depth of approximately 1 cm, which allowed us to image the entire cortical gray matter in the field of view of the imaging plane.
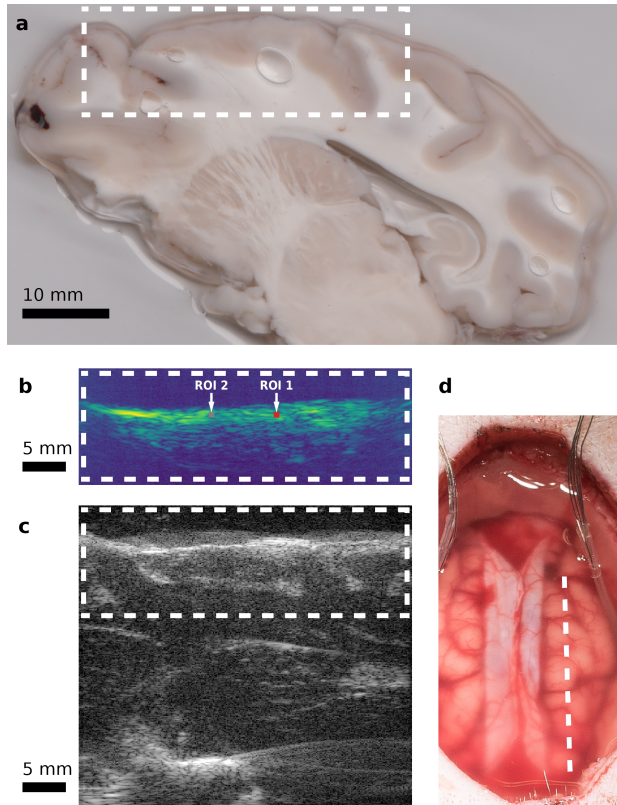
Figure 2. Hybrid photoacoustic ultrasonic (PAUS) imaging of a porcine brain. The dashed white line and boxes show corresponding sections of the swine cortex. **(a)** Photograph of a sagittal surgical slice segmented from the extracted brain, 1 cm from the midline. The shown segment is manually registered to **(b)** a representative photoacoustic (PA) image with two regions of interest (ROI), and **(c)** the corresponding ultrasound (US) B-Mode image. **(d)** Photograph of the exposed cortex after the craniotomy and dura mater retraction with the dashed line marking the PAUS imaging plane. The electrocorticography (ECoG) electrodes are positioned in the lateral margins.

By estimating sO_2 in each pixel of our reconstructed multispectral images we observed a single wave of hypoxia spreading from the point of KCl stimulation through the tissue at a speed of approximately 5 mm/min. The estimated sO_2 for two sub-surface regions of interest (ROI) is plotted in Fig. 3 a to illustrate this wave. sO_2 in a wide field of view during the same time frame is shown in Supplemental Video 1 played at a factor

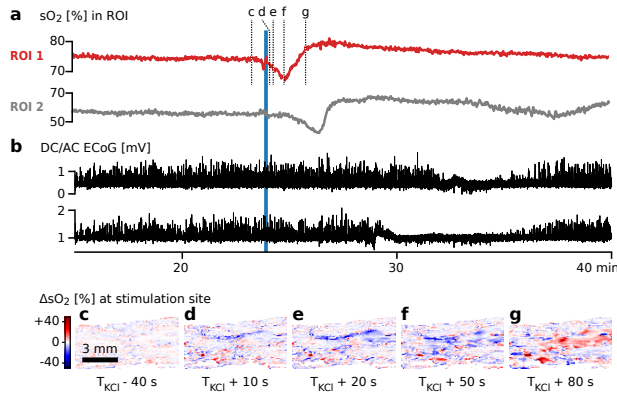**Figure 3.** Results of *initial wave experiment* showing spreading depolarization (SD) starting from an equilibrium state. **(a)** Estimated blood oxygenation (sO_2) of two regions of interest (ROI) in the left hemisphere (see Fig. 2 b). **(b)** Simultaneous electrocorticography (ECoG) monitoring. Data from two adjacent electrodes on the left hemisphere is shown – the other three channels on the left hemisphere and the five channels on the right hemisphere showed no change. The electrodes were placed on the lateral margins of the brain as to not interfere with hybrid photoacoustic ultrasonic (PAUS) imaging. **(c)**–**(g)** Absolute change in estimated sO_2 (ΔsO_2) in a region near the stimulation site (c) before potassium chloride (KCl) stimulation and (d)–(g) 10-80 s after stimulation. In (d)–(f) spreading, intensifying hypoxia is measured followed by (g) an overcompensation in sO_2.

100 timelapse. The wave of hypoxia coincides with the ECoG measurements on two electrodes in the proximity whose signals are plotted in Fig. 3 b; they clearly show a single SD wave moving through the cortex, while the other electrodes on both hemispheres showed no change in activity. Fig. 3 c–g shows the change in estimated sO_2 in the region around the stimulation as hypoxia propagating through the tissue followed by an increase in sO_2 over the baseline.

The purpose of the *cluster experiment* was to investigate the hemodynamic changes during SD clusters with PAUS. To this end, we repeatedly stimulated the brain with KCl until we observed the occurrence of
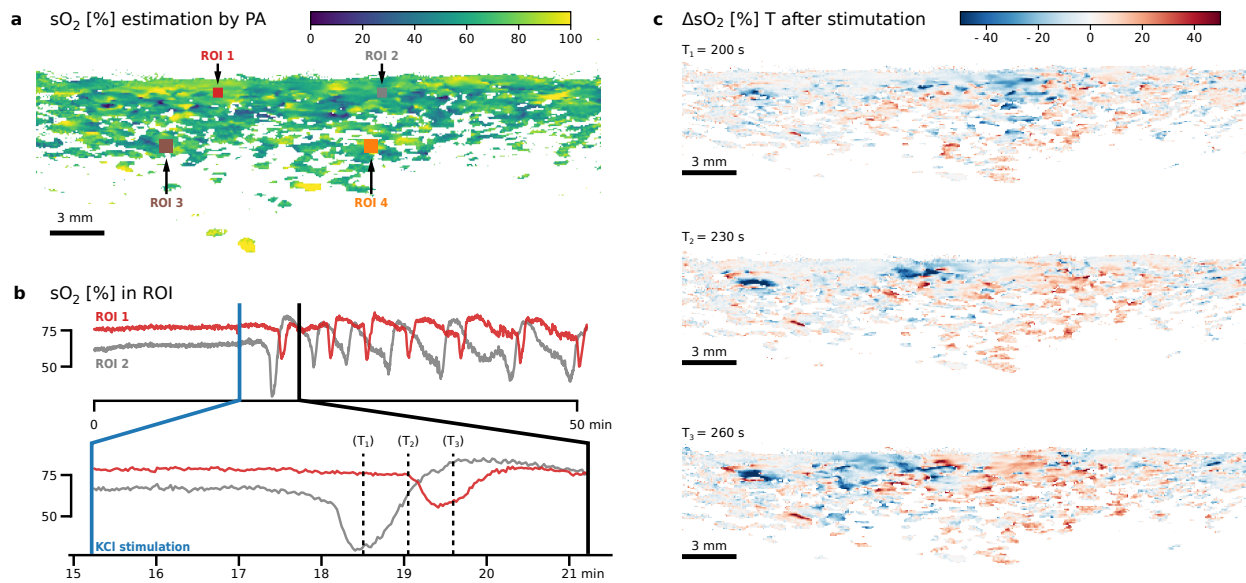
Figure 4. Multispectral photoacoustic (PA) imaging of blood oxygenation (sO_2) as part of the *cluster experiment*. After a 15 min baseline scan, spreading depolarization (SD) was induced by potassium chloride (KCl) stimulation in the left hemisphere of a porcine brain. The sagittal plane was continuously imaged for 51 min. **(a)** PA sO_2 estimation before stimulation with marked regions of interest (ROI). Refer to Supplemental Video 2 – a time lapse video of the change of sO_2 – for a complete view. The playback speed is 90 times the recording speed. **(b)** Time evolution of estimated sO_2 in the two ROI (top: whole recording period; bottom: first wave). **(c)** The change in blood oxygenation (ΔsO_2) relative to before KCl stimulation is shown for three example time steps 30 seconds apart (T_1, T_2 and T_3), corresponding to the dashed lines in (b).

clustered SDs both electrically with ECoG and optically with IOS as an additional state of the art reference for surface measurement of SD. Once the SDs had subsided, we started PAUS measurements with a new KCl stimulation after a baseline recording period of 15 min (details see Methods).

As shown in Fig. 4 a + b as well as Supplemental Video 2, there again was no change in the sO_2 estimation in the imaged sagittal plane in the left hemisphere during the baseline period. After KCl stimulation, we observed repetitive waves of hypoxia propagating through the imaging plane, followed by an overcompensation in sO_2 propagating through the cortex to up to a depth of approximately 2 to 5 mm below the brain surface. Fig. 4c illustrates one such wave propagating from left to right during one minute as a change in sO_2 estimation. The speed of the waves was measured as 3–9 mm/min between ROI 1 and 2. ECoG measurements on the left hemisphere shown in Fig. 5 b indicate a SD cluster with the same frequency and speed of the sO_2 changes (Fig. 5 a). As was the case in the *initial wave experiment* no change in ECoG activity in the right hemisphere was observed.

In addition to the sO_2 estimation from spectral unmixing we estimated the total hemoglobin (THb) for the *cluster experiment*; this is visualized in Supplemental Video 3. The changes of THb in the ROI are shown in Fig. 5 c, where ROIs 3 and 4 seem to exhibit low frequency vascular fluctuations (LF-VF) [39] which appear to be depressed after SD [11, 40].
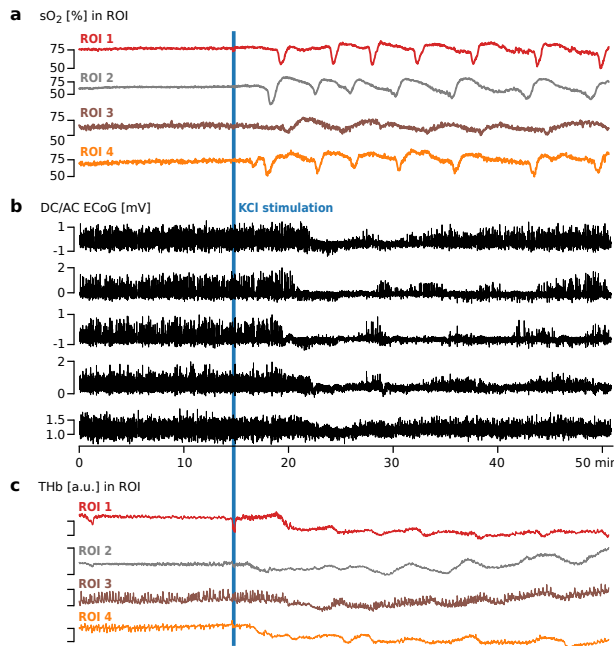
Figure 5. Monitoring of hemodynamic changes in four regions of interest (ROI) (see Fig. 4 a) as part of the *cluster experiment*. Spreading Depolarization (SD) was induced 15 min after start of recording by potassium chloride (KCl) stimulation on the left hemisphere of a porcine brain. (a) Blood oxygenation (sO_2) in four ROIs in the left hemisphere. (b) Simultaneous electrocorticography (ECoG) monitoring with five electrodes placed on the left hemisphere of the porcine brain. The occurrence of clustered SD is clearly visible as sudden direct current (DC) shifts spreading to neighboring channels, coinciding with spreading depression of the high frequency components. (c) Monitoring of total hemoglobin (THb) in four ROI. In ROI 3 and ROI 4 low frequency vascular fluctuations (LF-VF) can be observed which appear to be periodically depressed by SD.

Discussion

We investigated the imaging of SDs based on the concept of PA imaging. Our approach involves simultaneous US and multispectral PA imaging for time-resolved reconstruction of tissue oxygenation in sagittal image slices.

Two *in vivo* porcine experiments with our PAUS system provide the following evidence suggesting that our concept allows for the detection and monitoring of SD.

(1) *Hypoxia consistent with ECoG:* By estimation of sO_2, we observed pronounced drops in estimated sO_2 after KCl stimulation (cf. Fig. 3 a + 4 b). This local hypoxia lasted for around 30 seconds and was followed by an overcompensation or return to baseline sO_2. These changes were consistent with the occurrence of SD in ECoG. The indicators we used to identify SD in ECoG were based on consensus [15]: A characteristic abrupt DC shift followed by a longer lasting positivity, and a reduction in amplitudes of spontaneous AC activity. Both of which needed to spread with a speed of 1.5–9.5 mm/min between electrodes and not cross hemispheres.

(2) *Transient increase in blood volume:* By estimation of THb, we also observed a so-called *normal hemodynamic response* – a pronounced transient increase in blood volume (hyperemia) which was followed by a mild long-lasting oligemia (Fig. 5 c). Note that the results from THb estimation are less conclusive compared to the sO_2 based measurements as THb estimations are more susceptible to absolute changes in light fluence over all measured wavelengths. This is caused by the change in illumination geometry due to swelling which causes a slow shift in the absolute THb signal as shown in Fig. 4 c. Lower fluence, generally in higher depths also cause the signal to noise ratio to deteriorate, which can be observed when comparing ROI 1 with ROI 3 in Fig. 5 a.

(3) *Speed of wave propagation:* Both the changes in sO_2 and THb propagated through the gray matter at speeds of 3–9 mm/min. This is consistent with speed of SD reported in the literature as 1.7–9.2 mm/min [11] or 1.5–9.5 mm/min [15] in gyrencephalic brain (3–9 mm/min in porcine brain [13]).

(4) *Low-frequency vascular fluctuations:* We also observed changes in low-frequency vascular fluctuations (LF-VF) [40] (Fig. 5 c). The observed LF-VF "display[ed] a spreading suppression in a similar fashion to that of SDs" in ECoG (see [26]). Note that LF-VF were only visible in the vicinity of larger vessels, which was the rationale for placing ROIs 3 and 4 in such regions.

We conclude from these observations that our measurements clearly support our initial hypothesis and suggest that PAUS is able to image SD as a change in sO_2. In contrast to all other methods proposed to monitor SD to date, our approach has the unique advantage that it features both high resolution and high imaging depth. While it is not suitable for imaging the entire gyrencephalic brain, penetration depth is sufficient to image the entire thickness of the cortical grey matter. Furthermore, the simultaneous PA and US imaging proved to be useful for anatomical orientation during the intervention (i.e. for needle guidance for KCl stimulation). Given these advantages, we see a potential use of PA imaging for SD characterization i.e. during pharmacological trials on the gyrencephalic brain. As the thickness of the human cerebral cortex is comparable, usually averaging 2.5 mm and not exceeding 5 mm [41], PA imaging would be ideally suited for the study of SD in patients, as well. While, PA imaging cannot currently penetrate through an intact human skull [29], PA imaging could for example be used postoperative to study SD in stroke patients [42] with a hemicraniectomy [43].

Our pilot study strongly suggests that photoacoustics could become a valuable tool for detection, imaging, and monitoring SD. Due to its high spatiotemporal resolution this approach can be used to more precisely study where (i.e. which neuron layer) SDs originate and how they propagate, thus adding to our understanding of the nature of SD and its contribution to brain injuries and disease progression.

Methods

PAUS imaging system

The custom built hybrid photoacoustic ultrasonic (PAUS) imaging system is based on a 128 channel ultrasound data acquisition system (DiPhAs, Fraunhofer IBMT, St. Ingbert, Germany) with a 128-element linear US transducer operating on a center frequency of 7.5 MHz and broad acoustic response (L7-Xtech, Vermon, Tours, France). Due to its low level application programming interface (API) access, the system allows for raw data access and an interleaved PAUS imaging mode. This interleaved mode acquires US data from several shots after each PA data acquisition. The data acquisition (DAQ) module is combined with a fast tuning optical parametric oscillator (OPO) laser cart (Phocus Mobile, Opotek, Carlsbad, USA) which yields 690 nm – 950 nm, 5 ns long laser pulses with a pulse repetition rate of 20 Hz and a per laser pulse power of up to 50 mJ. The wavelength of each laser pulse can be tuned in between shots, allowing for real time multispectral acquisition sequences. Laser fiber bundles ending in two line arrays are attached to the transducer by a 3D-printed frame including acrylic windows for the laser output. For each experiment the entire probe was wrapped in a sterile ultrasound probe cover and gold leaf was placed between the US transducer and the probe cover to reduce artifacts created by light absorption in the US transducer. For live imaging and recording all APIs to the system were integrated in the Medical Imaging Interaction Toolkit (MITK) software framework and the MITK workbench application was used throughout the intervention to control the PAUS system, configure the image acquisition, and show live PA and US imaging streams. During our experiments we visualized both streams with 15–20 fps using delay and sum (DAS) beamforming for an imaging depth of 4 cm with 256 reconstructed lines. For the *initial wave experiment* we imaged the wavelength sequencence (735 nm, 756 nm, 850 nm, 900 nm) selected to distinguish Hb and HbO [44]. Because we added an estimation of THb in the *cluster experiment* we instead imaged the isosbestic point of Hb and HbO at 798 nm for further reference, leading to the wavelength sequencence (760 nm, 798 nm, 858 nm).

Image reconstruction

The raw radiofrequency (rf) PA data acquired during the experiments was matched with the laser pulse energies recorded by a pyroelectric sensor (Ophir PE25-C, Ophir Optronics, North Andover, USA) built in the laser system (Phocus Mobile, Opotek, Carlsbad, USA) and matched with the wavelengths of the laser pulses measured by a spectrometer (HR2000+, Ocean Optics, Dunedin, USA). The wavelengths of the pulses were measured independently of the imaging system to account for calibration errors. The rf PA slice was then corrected for the corresponding pulse energies. The recorded PAUS data was already beamformed live during the experiment to reduce the system load writing to disk. A single US slice was recorded after each PA slice. The US image was a compounded image averaged from US data acquired at five angles, equidistant from +10 deg to −10 deg and beamformed to 256 lines using a delay and sum (DAS) algorithm with boxcar apodization. To convert the acquired rf PA slices into meaningful images suitable for multispectral analysis, the slices were beamformed with a reference DAS implementation [45] using Hanning apodization to 512 lines. B-Mode images with isotropic pixel spacing of 0.075 mm were formed with a Hilbert transform based envelope

detection filter. US B-Mode images were formed in the same way, only adding a subsequent logarithmic compression.

Motion compensation

The PA images obtained after beamforming are corrected for inter-frame motion introduced by breathing, pulse or swelling (1) to enable a more stable spectral unmixing and (2) to assure that a given pixel location corresponds to the same physical regions of interest (ROI). To correct for the inter-frame motion an optical flow based method is employed. The optical flow of each US image relative to the first US image in the entire recording is estimated using an algorithm proposed by Farnebäck [46]. The flow estimated from the US B-mode image is then used to warp the corresponding PA B-mode image.

Experimental Data Analysis

Because of the slow propagation of SD wave fronts we averaged over ten motion corrected frames of the same wavelength and still have the 1 s temporal resolution of IOS. Spectral unmixing of those image sequences was then performed using a non-negative constrained linear least squares solver (`scipy.optimize.nnls`). In all figures and supplemental material plots and videos one PA datapoint is averaged over ten frames and then averaged over the ROIs. Speeds of SD wavefronts were obtained by measuring the time between the local minima of sO_2 ROI 1 and ROI 2. The positions of ROIs 1 and 2 in both experiments were chosen at 1 mm depth and 7.5 mm apart, in the center of the reconstructed image stream. ROIs 3 and 4 were chosen deeper and close to larger vessels to investigate the LF-VF effect which, as discussed, can only be observed there. ROIs are otherwise representative of the entire data set as can be seen in the supplemental videos.

Animals

Protocols for all experiments were approved by the institutional animal care and use committee in Karlsruhe, Baden-Wuerttemberg, Germany (Protocol No. 35-9185.81/G-174/16). Female German Landrace swines of 31 and 33 kg were premedicated with Midazolam (Dormicum 0.5–0.7 mg/kg) and Azaperone (Stresnil 4 mg/kg) intramuscularly. After premedication, two venous lines were placed in the ear veins, and propofol (Disoprivan 5–7 mg/kg) was administered intravenously to facilitate the intubation. The animals were then intubated and mechanically ventilated and the pressure controlled ventilation was adapted to a respiration rate of 12–20/min, a flow of 2.5 l O_2/min, 2.0 l air/min, FiO2 35 % and volume 7–10 ml per kg. The maintenance of anesthesia required inhalational anesthesia with isoflurane (Isosthesia 0.6—1.0 %) and intravenous midazolam at a continuous dose of 0.5–0.7 mg/kg/h via perfusion and maintained throughout the entire experiment. If a wakening reaction occurred, a bolus of propofol (Disoprivan 5–7 mg/kg) was administered. Temperature was monitored with a rectal probe. A 4-Fr catheter was placed in the right femoral artery for permanent monitoring of the mean arterial blood pressure (Raumedic AG, Helmbrechts, Germany). Capillary oxygen saturation (SpO_2) was monitored from one ear. Arterial blood gases were obtained in the animal used for the *initial wave experiment*. Ringer's solution was given intravenously over 8—12 h, to compensate for intraoperative bleeding,

urinary output and insensible losses. The two animals used in this study were used primarily for this project. After finishing the protocol the animal used for the *cluster experiment* was used for other unrelated studies.

Surgery

Animals were fixed in a stereotactic frame (Standard Stereotaxic Instruments, RWD Life Science, Shenzhen, China) and an extensive craniotomy with excision of the dura mater was performed, to view the subarachnoidal space bilaterally. Initially, the brain surface was immersed for 30 to 40 min in a standard lactated Ringer's solution with an elevated K+ concentration (7 mmol/l), as preconditioning for SD induction, as proposed by Bowyer et al. [47] for the KCl model of SD. EcoG was performed with two strips of 5 electrodes each (Ad-tech, Racine, Wisconsin, USA) that were placed at the lateral margins of the craniotomy below the dura mater and above the parietal cortex. A camera for IOS imaging and its corresponding light sources were mounted above the stereotactic frame. After preconditioning a 5–10 mm deep paraffin pool was filled over the exposed cortex, to reduce the diffusion of the KCl stimulation. When necessary, paraffin was withdrawn and new paraffin was added. The preparation time was 4–5 h before the KCl stimulations started. A gel pad (Aquaflex Ultrasound Gel Pad, Parker Laboratories, Fairfield, USA) was cut in shape of the exposed brain surface and placed in the paraffin pool. The custom designed PAUS probe (see Methods, PAUS Imaging system) was placed on top the gel pad and fixed relative to the frame. For the *initial wave experiment* the gel pad and PAUS imaging system was placed before the initial stimulation. For the *cluster experiment* the gel pad and system was placed after the initial KCl stimulations and the accompanying IOS imaging was performed. With the help of live US imaging, it was positioned to image a sagittal plane of the left hemisphere approximately 1 cm from the midline. For the *cluster experiment* we waited until any residual SD from prior stimulation subsided in the ECoG monitoring. Only then did we start recording PAUS data in a sagittal plane for 15 min as a baseline. After a sufficient baseline recording, spreading depolarization was triggered using 2–5 μl of 1 mol/l KCl solution with a Hamilton syringe. The stimulus needle was guided using the live PAUS image streams visualized in MITK.

Monitoring

All relevant physiological parameters, such as mean arterial pressure, rectal temperature, heart rate, and arterial oxygen saturation, were continuously monitored. A mean systolic arterial pressure of 60 to 80 mmHg, a temperature between 36 and 37 °C, $SaO_2 > 90\%$, pCO_2 between 35 and 45 mmHg, $pO_2 > 80$ mmHg were maintained.

Electrocorticography

Electrocorticography (ECoG) recording with the subdural electrodes was perfomed in 10 active channels, using the Powerlab 16/SP analogue/digital converter coupled with the LabChart-7 software (ADInstruments, New South Wales, Australia) at a sampling frequency of 400 Hz. For visualization, in all figures and supplemental material, ECoG data was post-processed in Python using a 45 Hz Butterworth low pass filter to filter alternating current (AC) noise.

Intrinsic optical signal imaging

intrinsic optical signal (IOS) imaging is a functional neuroimaging technique that measures cortical reflectance changes [24]. We imaged one band at a wavelength of 564 nm (14 nm FWHM) with a charge-coupled device (CCD) camera (Smartec GC1621M, MaxxVision GmbH, Stuttgart, Germany) which was mounted 25 cm above the exposed cortex. Images were acquired with static illumination and 2 s CCD integration time. Changes in tissue reflectance were registered using a method described in [24]. IOS was only used as an additional reference to the ECoG in the animal corresponding to the *cluster experiment* to ensure that preconditioning was sufficient and SDs were easily triggered.

References

1. Jens P. Dreier. The role of spreading depression, spreading depolarization and spreading ischemia in neurological disease. *Nat. Med.*, 17(4):439–447, April 2011.

2. Christian Dohmen, Oliver W. Sakowitz, Martin Fabricius, Bert Bosche, Thomas Reithmeier, Ralf-Ingo Ernestus, Gerrit Brinker, Jens P. Dreier, Johannes Woitzik, Anthony J. Strong, Rudolf Graf, and Co-Operative Study of Brain Injury Depolarisations (COSBID). Spreading depolarizations occur in human ischemic stroke with high incidence. *Ann. Neurol.*, 63(6):720–728, June 2008.

3. Jed A. Hartings, M. Ross Bullock, David O. Okonkwo, Lilian S. Murray, Gordon D. Murray, Martin Fabricius, Andrew Ir Maas, Johannes Woitzik, Oliver Sakowitz, Bruce Mathern, Bob Roozenbeek, Hester Lingsma, Jens P. Dreier, Ava M. Puccio, Lori A. Shutter, Clemens Pahl, Anthony J. Strong, and Co-Operative Study on Brain Injury Depolarisations. Spreading depolarisations and outcome after traumatic brain injury: a prospective observational study. *Lancet Neurol*, 10(12):1058–1064, December 2011.

4. Jens P. Dreier, Johannes Woitzik, Martin Fabricius, Robin Bhatia, Sebastian Major, Chistoph Drenckhahn, Thomas-Nicolas Lehmann, Asita Sarrafzadeh, Lisette Willumsen, Jed A. Hartings, Oliver W. Sakowitz, Jörg H. Seemann, Anja Thieme, Martin Lauritzen, and Anthony J. Strong. Delayed ischaemic neurological deficits after subarachnoid haemorrhage are associated with clusters of spreading depolarizations. *Brain*, 129(Pt 12):3224–3237, December 2006.

5. Raimund Helbok, Mario Kofler, Alois Josef Schiefecker, Maxime Gaasch, Verena Rass, Bettina Pfausler, Ronny Beer, and Erich Schmutzhard. Clinical Use of Cerebral Microdialysis in Patients with Aneurysmal Subarachnoid Hemorrhage—State of the Art. *Front Neurol*, 8, November 2017.

6. M. Lauritzen. Cerebral blood flow in migraine and cortical spreading depression. *Acta Neurol. Scand., Suppl.*, 113:1–40, 1987.

7. Nouchine Hadjikhani, Margarita Sanchez del Rio, Ona Wu, Denis Schwartz, Dick Bakker, Bruce Fischl, Kenneth K. Kwong, F. Michael Cutrer, Bruce R. Rosen, Roger B. H. Tootell, A. Gregory Sorensen,

and Michael A. Moskowitz. Mechanisms of migraine aura revealed by functional MRI in human visual cortex. *PNAS*, 98(8):4687–4692, April 2001.

8. Aristides A. P. Leao. Spreading depression of activity in the cerebral cortex. *Journal of Neurophysiology*, 7(6):359–390, November 1944.

9. Cenk Ayata and Martin Lauritzen. Spreading Depression, Spreading Depolarizations, and the Cerebral Vasculature. *Physiol. Rev.*, 95(3):953–993, July 2015.

10. David Y. Chung, Fumiaki Oka, and Cenk Ayata. Spreading Depolarizations: A Therapeutic Target Against Delayed Cerebral Ischemia After Subarachnoid Hemorrhage. *Journal of Clinical Neurophysiology*, 33(3):196–202, June 2016.

11. Johannes Woitzik, Nils Hecht, Alexandra Pinczolits, Nora Sandow, Sebastian Major, Maren K. L. Winkler, Steffen Weber-Carstens, Christian Dohmen, Rudolf Graf, Anthony J. Strong, Jens P. Dreier, Peter Vajkoczy, and COSBID study group. Propagation of cortical spreading depolarization in the human cortex after malignant stroke. *Neurology*, 80(12):1095–1102, March 2013.

12. Takahiro Takano, Guo-Feng Tian, Weiguo Peng, Nanhong Lou, Ditte Lovatt, Anker J. Hansen, Karl A. Kasischke, and Maiken Nedergaard. Cortical spreading depression causes and coincides with tissue hypoxia. *Nat. Neurosci.*, 10(6):754–762, June 2007.

13. Edgar Santos, Renán Sánchez-Porras, Oliver W. Sakowitz, Jens P. Dreier, and Markus A. Dahlem. Heterogeneous propagation of spreading depolarizations in the lissencephalic and gyrencephalic brain. *J. Cereb. Blood Flow Metab.*, 37(7):2639–2643, July 2017.

14. Edgar Santos, Michael Schöll, Renán Sánchez-Porras, Markus A. Dahlem, Humberto Silos, Andreas Unterberg, Hartmut Dickhaus, and Oliver W. Sakowitz. Radial, spiral and reverberating waves of spreading depolarization occur in the gyrencephalic brain. *Neuroimage*, 99:244–255, October 2014.

15. Jens P. Dreier, Martin Fabricius, Cenk Ayata, Oliver W. Sakowitz, C. William Shuttleworth, Christian Dohmen, Rudolf Graf, Peter Vajkoczy, Raimund Helbok, Michiyasu Suzuki, Alois J. Schiefecker, Sebastian Major, Maren Kl Winkler, Eun-Jeung Kang, Denny Milakara, Ana I. Oliveira-Ferreira, Clemens Reiffurth, Gajanan S. Revankar, Kazutaka Sugimoto, Nora F. Dengler, Nils Hecht, Brandon Foreman, Bart Feyen, Daniel Kondziella, Christian K. Friberg, Henning Piilgaard, Eric S. Rosenthal, M. Brandon Westover, Anna Maslarova, Edgar Santos, Daniel Hertle, Renán Sánchez-Porras, Sharon L. Jewell, Baptiste Balança, Johannes Platz, Jason M. Hinzman, Janos Lückl, Karl Schoknecht, Michael Schöll, Christoph Drenckhahn, Delphine Feuerstein, Nina Eriksen, Viktor Horst, Julia S. Bretz, Paul Jahnke, Michael Scheel, Georg Bohner, Egill Rostrup, Bente Pakkenberg, Uwe Heinemann, Jan Claassen, Andrew P. Carlson, Christina M. Kowoll, Svetlana Lublinsky, Yoash Chassidim, Ilan Shelef, Alon Friedman, Gerrit Brinker, Michael Reiner, Sergei A. Kirov, R. David Andrew, Eszter Farkas, Erdem Güresir, Hartmut Vatter, Lee S. Chung, K. C. Brennan, Thomas Lieutaud, Stephane Marinesco, Andrew Ir Maas,

Juan Sahuquillo, Markus A. Dahlem, Frank Richter, Oscar Herreras, Martyn G. Boutelle, David O. Okonkwo, M. Ross Bullock, Otto W. Witte, Peter Martus, Arn Mjm van den Maagdenberg, Michel D. Ferrari, Rick M. Dijkhuizen, Lori A. Shutter, Norberto Andaluz, André P. Schulte, Brian MacVicar, Tomas Watanabe, Johannes Woitzik, Martin Lauritzen, Anthony J. Strong, and Jed A. Hartings. Recording, analysis, and interpretation of spreading depolarizations in neurointensive care: Review and recommendations of the COSBID research group. *J. Cereb. Blood Flow Metab.*, 37(5):1595–1625, May 2017.

16. Jed A. Hartings, J. Adam Wilson, Jason M. Hinzman, Sebastian Pollandt, Jens P. Dreier, Vince DiNapoli, David M. Ficker, Lori A. Shutter, and Norberto Andaluz. Spreading depression in continuous electroencephalography of brain trauma. *Ann. Neurol.*, 76(5):681–694, November 2014.

17. Isamu Aiba and Jeffrey L. Noebels. Spreading depolarization in the brainstem mediates sudden cardiorespiratory arrest in mouse SUDEP models. *Science Translational Medicine*, 7(282):282ra46–282ra46, April 2015.

18. Julien Chuquet, Liad Hollender, and Esther A. Nimchinsky. High-Resolution In Vivo Imaging of the Neurovascular Unit during Spreading Depression. *J. Neurosci.*, 27(15):4036–4044, April 2007.

19. Timothy H. Murphy, Ping Li, Kellen E. Betts, and Richard Liu. Two-photon imaging of stroke onset in vivo reveals that NMDA-receptor independent ischemic depolarization is the major cause of rapid reversible damage to dendrites and spines., 2008.

20. W. Christopher Risher, Deborah Ard, Jianghe Yuan, and Sergei A. Kirov. Recurrent Spontaneous Spreading Depolarizations Facilitate Acute Dendritic Injury in the Ischemic Penumbra. *J Neurosci*, 30(29):9859–9868, July 2010.

21. Phill B. Jones, Hwa Kyuong Shin, David A. Boas, Bradley T. Hyman, Michael J. Moskowitz, Cenk Ayata, and Andrew K. Dunn. Simultaneous multispectral reflectance imaging and laser speckle flowmetry of cerebral blood flow and oxygen metabolism in focal cerebral ischemia. *JBO, JBOPFO*, 13(4):044007, July 2008.

22. Andrew K. Dunn, Hayrunnisa Bolay, Michael A. Moskowitz, and David A. Boas. Dynamic Imaging of Cerebral Blood Flow Using Laser Speckle. *J Cereb Blood Flow Metab*, 21(3):195–201, March 2001.

23. Alyssa M. Ba, Michael Guiou, Nader Pouratian, Arpitha Muthialu, David E. Rex, Andrew F. Cannestra, James W. Y. Chen, and Arthur W. Toga. Multiwavelength optical intrinsic signal imaging of cortical spreading depression. *J. Neurophysiol.*, 88(5):2726–2735, November 2002.

24. Edgar Santos, Michael Schöll, Renan Sanchez-Porras, Modar Kentar, Berk Orakcioglu, Andreas Unterberg, Hartmut Dickhaus, and Oliver W. Sakowitz. Cortical spreading depression dynamics can be studied using intrinsic optical signal imaging in gyrencephalic animal cortex. *Acta Neurochir. Suppl.*, 118:93–97, 2013.

25. Martin Seule, Emanuela Keller, Andreas Unterberg, and Oliver Sakowitz. The Hemodynamic Response of Spreading Depolarization Observed by Near Infrared Spectroscopy After Aneurysmal Subarachnoid Hemorrhage. *Neurocrit Care*, 23(1):108–112, August 2015.

26. Maren K. L. Winkler, Yoash Chassidim, Svetlana Lublinsky, Gajanan S. Revankar, Sebastian Major, Eun-Jeung Kang, Ana I. Oliveira-Ferreira, Johannes Woitzik, Nora Sandow, Michael Scheel, Alon Friedman, and Jens P. Dreier. Impaired neurovascular coupling to ictal epileptic activity and spreading depolarization in a patient with subarachnoid hemorrhage: Possible link to blood–brain barrier dysfunction. *Epilepsia*, 53(s6):22–30, 2012.

27. P. W. McCormick, M. Stewart, M. G. Goetting, M. Dujovny, G. Lewis, and J. I. Ausman. Noninvasive cerebral optical spectroscopy for monitoring cerebral oxygen delivery and hemodynamics. *Crit Care Med*, 19(1):89–97, January 1991.

28. S. Umesh Rudrapatna, Arend M. Hamming, Marieke J. H. Wermer, Annette van der Toorn, and Rick M. Dijkhuizen. Measurement of distinctive features of cortical spreading depolarizations with different MRI contrasts. *NMR Biomed*, 28(5):591–600, May 2015.

29. Junjie Yao and Lihong V. Wang. Photoacoustic brain imaging: from microscopic to macroscopic scales. *Neurophotonics*, 1(1), July 2014.

30. Lihong V Wang and Song Hu. Photoacoustic tomography: in vivo imaging from organelles to organs. *science*, 335(6075):1458–1462, 2012.

31. Alexander Graham Bell. Art. xxxiv.–on the production and reproduction of sound by light. *American Journal of Science (1880-1910)*, 20(118):305, 1880.

32. Jun Xia, Junjie Yao, and Lihong V. Wang. Photoacoustic tomography: principles and advances. *Electromagn Waves (Camb)*, 147:1–22, 2014.

33. Changhui Li and Lihong V. Wang. Photoacoustic tomography and sensing in biomedicine. *Phys Med Biol*, 54(19):R59–R97, October 2009.

34. Adrian Taruttis and Vasilis Ntziachristos. Advances in real-time multispectral optoacoustic imaging and its applications. *Nature Photonics*, 9(4):219–227, April 2015.

35. Stratis Tzoumas and Vasilis Ntziachristos. Spectral unmixing techniques for optoacoustic imaging of tissue pathophysiology. *Philos Trans A Math Phys Eng Sci*, 375(2107), November 2017.

36. Stratis Tzoumas, Antonio Nunes, Ivan Olefir, Stefan Stangl, Panagiotis Symvoulidis, Sarah Glasl, Christine Bayer, Gabriele Multhoff, and Vasilis Ntziachristos. Eigenspectra optoacoustic tomography achieves quantitative blood oxygenation imaging deep in tissues. *Nature Communications*, 7:12121, June 2016.

37. Thomas Kirchner, Esther Wild, Klaus H. Maier-Hein, and Lena Maier-Hein. Freehand photoacoustic tomography for 3d angiography using local gradient information. In *Photons Plus Ultrasound: Imaging and Sensing 2016*, volume 9708, page 97083G. International Society for Optics and Photonics, March 2016.

38. Jeesu Kim, Sara Park, Yuhan Jung, Sunyeob Chang, Jinyong Park, Yumiao Zhang, Jonathan F. Lovell, and Chulhong Kim. Programmable Real-time Clinical Photoacoustic and Ultrasound Imaging System. *Scientific Reports*, 6:35137, October 2016.

39. Hellmuth Obrig, Markus Neufang, Rüdiger Wenzel, Matthias Kohl, Jens Steinbrink, Karl Einhäupl, and Arno Villringer. Spontaneous Low Frequency Oscillations of Cerebral Hemodynamics and Metabolism in Human Adults. *NeuroImage*, 12(6):623–639, December 2000.

40. Jens P. Dreier, Sebastian Major, Andrew Manning, Johannes Woitzik, Chistoph Drenckhahn, Jens Steinbrink, Christos Tolias, Ana I. Oliveira-Ferreira, Martin Fabricius, Jed A. Hartings, Peter Vajkoczy, Martin Lauritzen, Ulrich Dirnagl, Georg Bohner, and Anthony J. Strong. Cortical spreading ischaemia is a novel process involved in ischaemic damage in patients with aneurysmal subarachnoid haemorrhage. *Brain*, 132(7):1866–1881, July 2009.

41. Bruce Fischl and Anders M Dale. Measuring the thickness of the human cerebral cortex from magnetic resonance images. *Proceedings of the National Academy of Sciences*, 97(20):11050–11055, 2000.

42. Martin Lauritzen, Jens Peter Dreier, Martin Fabricius, Jed A Hartings, Rudolf Graf, and Anthony John Strong. Clinical Relevance of Cortical Spreading Depression in Neurological Disorders: Migraine, Malignant Stroke, Subarachnoid and Intracranial Hemorrhage, and Traumatic Brain Injury. *J Cereb Blood Flow Metab*, 31(1):17–35, January 2011.

43. Eric Jüttler, Andreas Unterberg, Johannes Woitzik, Julian Bösel, Hemasse Amiri, Oliver W Sakowitz, Matthias Gondan, Petra Schiller, Ronald Limprecht, Steffen Luntz, et al. Hemicraniectomy in older patients with extensive middle-cerebral-artery stroke. *New England Journal of Medicine*, 370(12):1091–1100, 2014.

44. Geoffrey P Luke, Seung Yun Nam, and Stanislav Y Emelianov. Optical wavelength selection for improved spectroscopic photoacoustic imaging. *Photoacoustics*, 1(2):36–42, 2013.

45. Thomas Kirchner, Franz Sattler, Janek Gröhl, Lena Maier-Hein, Thomas Kirchner, Franz Sattler, Janek Gröhl, and Lena Maier-Hein. Signed Real-Time Delay Multiply and Sum Beamforming for Multispectral Photoacoustic Imaging. *Journal of Imaging*, 4(10):121, October 2018.

46. Gunnar Farnebäck. Two-Frame Motion Estimation Based on Polynomial Expansion. In Josef Bigun and Tomas Gustavsson, editors, *Image Analysis*, Lecture Notes in Computer Science, pages 363–370. Springer Berlin Heidelberg, 2003.

47. S. M. Bowyer, N. Tepley, N. Papuashvili, S. Kato, G. L. Barkley, K. M. A. Welch, and Y. C. Okada. Analysis of MEG signals of spreading cortical depression with propagation constrained to a rectangular cortical strip: II. Gyrencephalic swine model. *Brain Research*, 843(1):79–86, October 1999.

Acknowledgements

Author Contributions

T.K. conceived the study, implemented the system, designed the experiments, performed the experiments, analyzed the data, drafted the initial manuscript; J.G. designed the experiments, performed the experiments, analyzed the data, edited the entire manuscript; M.A.H. helped plan the experiments, performed the experiments, edited the entire manuscript; T.A. performed the experiments, helped analyze the data, edited the entire manuscript; A.H.-A. performed the experiments, edited the entire manuscript; E.S. conceived the study, designed the experiments, performed the experiments, supervised the neurosurgical aspects of the work, edited the entire manuscript; L.M.-H. conceived the study, designed the experiments, supervised the biomedical informatics and engineering aspects of the work, edited the entire manuscript.

Supplemental Material

Supplemental Video 1

Initial wave experiment. Blood oxygenation (sO$_2$): link to online video

Supplemental Video 2

Cluster experiment. Blood oxygenation (sO$_2$): link to online video

Supplemental Video 3

Cluster experiment. Total Hemoglobin (THb) and low frequency vascular fluctuations (LF-VF): link to online video

Part III

DISCUSSION

This thesis investigated blood oxygenation estimations with multispectral PAI in an interventional context. To this end, (1) an interventional real-time imaging system was designed and implemented based on a medical US research system. Furthermore, (2) real-time capable image processing methods were presented as well as approaches for quantification of tissue absorption and blood oxygenation. Finally, (3) in a series of experiments, both the system and methods were applied to brain imaging, performing the first high resolution tomography of spreading depolarization, and at the same time the first interventional photoacoustic imaging on any gyrencephalic brain. These three contributions and how they fit in the larger field will be discussed in the first three Chapters of this final Part, followed by a general Conclusion & Outlook.

IMAGING SYSTEM

The imaging system which was presented and used throughout this thesis is based on a medical US research system and combined with a fast-tunable OPO laser cart. Similar systems based on medical US hardware were developed by other groups independently from the work in this thesis [55]. In contrast to this work, our system was integrated in both real-time software and hardware, as it was designed for interventional use. A few hardware considerations are to be accounted for in order to make such a system usable in surgical interventions: the hardware needs to be mobile, the probe sterile and easily held or precisely positioned in place. For our system the handling and positioning hardware was either 3D printed or in the case of the attachment to the stereotaxic frame, specially machined. The probe was kept sterile by plastic US transducer covers. The arguably larger challenge is the software integration of laser system and US system into one real-time imaging platform. The system used in this thesis not only addresses this, but was developed open source within MITK to better disseminate this often overlooked aspect of a PAI system to the community.

The applicability of our specific imaging system to surgical interventions was shown and will be discussed in depth later. The presented system remains a useful research platform for such applications, given the full access to raw data and extensive configurability and extendablity of the platform – i. e. work is already in preparation to guide the PAI imaging system robotically, based on recent implementations of robotic US guidance in MITK [64]. For clinical translation, PA contrast is increasingly considered as an additional contrast during medical US imaging. The use of narrow-band linear US transducers for PAI therefore seems sensible, but severely limits the overall signal and image quality and even excludes applications like transcranial imaging entirely. Another drawback of linear arrays are the increased artifacts due to their limited view as described in Section 3.3.1. Cup or ring shaped arrays reduce the severity of the limited view by increasing the measurement angle. These systems are specially tailored to increase PA image quality and therefore usually have no US imaging capability or an associated cost in US image quality.

The continuous development of acoustic sensors as well as photonics and laser technology will further increase imaging depth and quality, and a move to more broadband acoustic sensors may enable PAI systems to produce images in currently prohibitive tissues and make the acquired signals more quantifiable.

SIGNAL PROCESSING

This thesis contained classic image processing works and machine learning-based quantification methods.

To be usable in an interventional setting, the classic image processing work in this thesis mostly aimed at real-time visualization of the acquired data. The beamforming and motion-correction contributions achieved this, and were consequently of use in several applications. These methods are all widely – and due to their open source implementation, easily – applicable.

The quantification work in this thesis is designed with real-time applicability in mind and the presented methods are dramatically less computationally expensive than state-of-the-art methods [65]. This is mostly achieved by using machine learning approaches which can rapidly infer estimations. The presented qPAI approaches to quantify absorption directly were the first to utilize machine learning to approach the optical inverse problem. Machine learning proved to be very effective *in silico* and even much more robust to simulated noise than previous approaches. How to modify and train a neural network to robustly estimate tissue parameters *in vivo* remains an open research question. Real labeled data is difficult to obtain in any quantity and training even with very involved simulation data will still leave a significant gap to reality. As closing this gap is unfeasible, other robust domain transfer solutions must be found. This will be the subject of future work.

A preliminary application of a quantitative method for learned spectral decoloring instead of direct absorption estimation is shown as part of C3. While these results look promising, they also highlight remaining challenges when training with simulated data and warrant further study and validation.

APPLICATION

An overarching objective, not only of this thesis, but really the field of translational photoacoustics is the search for specific clinical applications. PA contrast has proven to be exceptionally useful and specific in small animals but has yet to show such compelling results in clinical applications. Multispectral photoacoustics is able to image optical absorption contrast deeper than any other modality. Still, imaging depth remains the limiting factor for the clinical applicability of PAI. Translational research therefore tends to focus on superficial areas.

PA breast imaging is the most heavily investigated application [50, 59–61]. This is due to the easy accessibility of the site and the wide use of X-ray mammography screening. Without ionizing radiation, PAI mammography would have an immense impact on its own. The sensitivity for mammography screenings is already high, but PAI has an opportunity to improve on specificity and reduce avoidable biopsies. Currently, clinical PAI trials on already diagnosed tumors often have to exclude patients with deeper lesions, which makes standalone PAI mammography screenings unlikely to be sensitive.

This thesis approached a very different site and investigated interventional multispectral PAI of blood oxygenation for functional brain imaging. One of the first applications of PAI was imaging a hemodynamic contrast in a rat brain [6]. While skull already interferes with PA brain imaging in small animals, large animal or human skull not only causes stronger distortions and artifacts but attenuates the acoustic signal to a degree which makes any image reconstruction close to impossible. However, as was shown in manuscripts C3 and J4, with the skull removed during surgery, it is feasible to functionally image larger brains.

Transcranial imaging remains unfeasible with this approach, as a narrow clinical US transducer centered at around 7.5 MHz is not able to detect the lower acoustic frequency components which might be able to penetrate the skull bone [66]. This was confirmed on a porcine model before starting the craniotomy in an ongoing study.

Porcine brain is a medically more relevant stroke model [67] because it is – like the human brain – gyrencephalic, meaning it expresses a folded cortex. SD is a heavily studied phenomenon associated with a range of diseases including stroke. It tends to follow the gyri of such brains to a large extend. Using the system and methods developed in this thesis, we were able to show that interventional functional imaging of hemodynamics is possible throughout the cortex of a gyrencephalic brain.

4

CONCLUSION & OUTLOOK

The main objective of this thesis was to investigate the applicability of multispectral PAI for the interventional tomography of blood oxygenation in general, and the application to imaging of the gyrencephalic cortex in particular. To study the technique, a hybrid US and multispectral PAI system was designed, and implemented to be used in interventional settings for translational research. Methodological work on real-time capable algorithms for beamforming and motion correction was presented including proof-of-concept application of the methods on healthy human volunteers – imaging sO_2 in superficial vessels. Methods for qPAI were presented, and while direct quantification techniques could only be validated *in silico*, preliminary *in vivo* results for a novel spectral decoloring method are promising.

Both the developed system as well as some of the developed methods were applied interventionally imaging gyrencephalic brain to study SD in depth. Our approach was able to visualize hemodynamic information like sO_2 in the entire thickness of the gyrencephalic cortex with an unprecedented spatiotemporal resolution. This was the first application of PAI during a neurosurgical intervention on a gyrencephalic brain. The study of SD with PAI will continue as translational neurological research on a large bio-relevant model. While this is arguably closer to the clinic than small animal imaging, translation of PAI to human brain imaging remains unclear. SDs are an interesting field of study but are not yet understood well enough to be in themselves diagnostically relevant. Additionally, monitoring SD through skull using PAI is not feasible so far. However, PAI could be used to monitor SD in some stroke patients after a decompressive craniectomy – where part of the skull is removed to allow a swelling brain to expand. This may be an option to study the phenomenon in patients suffering from stroke.

For other organs, further technical advances and research with the aim of increasing imaging depth and quality is needed in order to apply photoacoustics to monitoring perfusion or sO_2. Possible applications may include monitoring organs after a transplant, or the reliable diagnosis or staging of inflammatory diseases like inflammatory bowel disease where hypoxia and a change of perfusion are disease markers [62].

If the transcranial obstacle can be overcome, non-invasive PA monitoring of sO_2 in the brain could be of great use in critical care. Increased imaging depth and quality, with improved quantification will further enable PAI in a wide range of applications.

LIST OF PUBLICATIONS

PEER-REVIEWED

Photoacoustics can image spreading depolarization deep in gyrencephalic brain
Thomas Kirchner, Janek Gröhl, Mildred Herrera, Tim Adler, Adrián
Hernández-Aguilera, Edgar Santos and Lena Maier-Hein
arXiv:1901.02786
Pre-print (2019) – in minor revision for Scientific Reports

*Uncertainty-aware performance assessment of optical imaging modalities with
invertible neural networks*
Tim J. Adler, Lynton Ardizzone, Anant Vemuri, Leonardo Ayala, Janek
Gröhl, Thomas Kirchner, Sebastian Wirkert, Jakob Kruse, Carsten Rother,
Ullrich Köthe and Lena Maier-Hein
doi:10.1007/s11548-019-01939-9
International Journal of Computer Assisted Radiology and Surgery (2019)

*Signed real-time delay multiply and sum beamforming for multispectral
photoacoustic imaging*
Thomas Kirchner, Franz Sattler, Janek Gröhl and Lena Maier-Hein
doi:10.3390/jimaging4100121
Journal of Imaging (2018)

Confidence estimation for machine learning-based quantitative photoacoustics
Janek Gröhl, Thomas Kirchner, Tim Adler and Lena Maier-Hein
doi:10.3390/jimaging4120147
Journal of Imaging (2018)

Context encoding enables machine learning-based quantitative photoacoustics
Thomas Kirchner, Janek Gröhl and Lena Maier-Hein
doi:10.1117/1.JBO.23.5.056008
Journal of Biomedical Optics (2017)

*MITK-OpenIGTLink for combining open-source toolkits in real-time
computer-assisted interventions*
Martin Klemm, Thomas Kirchner, Janek Gröhl, Dominik Cheray, Marco
Nolden, Alexander Seitel, Harald Hoppe, Lena Maier-Hein and Alfred Franz
doi:10.1007/s11548-016-1488-y
International Journal of Computer Assisted Radiology and Surgery (2016)

NON-PEER-REVIEWED

Photoacoustic monitoring of blood oxygenation during neurosurgical interventions
Thomas Kirchner, Janek Gröhl, Niklas Holzwarth, Mildred A. Herrera,
Adrián Hernández-Aguilera, Edgar Santos and Lena Maier-Hein
doi:10.1117/12.2509608
Proceedings of Photons Plus Ultrasound: Imaging and Sensing (2019)

International Photoacoustic Standardisation Consortium (IPASC): overview
Sarah Bohndiek, Joanna Brunker, Janek Gröhl, Lina Hacker, James Joseph, William C. Vogt, Paolo Armanetti, Hisham Assi, Jeffrey C. Bamber, Paul C. Beard, Thomas Berer, Richard Bouchard, Kimberly A. Briggman, Lucia Cavigli, Bryan Clingman, Ben T. Cox, Adrien E. Desjardins, Andrew Heinmiller, Jeesong Hwang, Eno Hysi, Aoife Ivory, Jithin Jose, Thomas Kirchner, Jan Klohs, Lena Maier-Hein, Efthymios Maneas, Julia Mannheim, Srirang Manohar, Lacey McNally, Luca Menichetti, Steven Miller, Stefan Morscher, Ruiqing Ni, Yoko Okamura, Malini C. Olivo, Marty Pagel, Geoff Parker, Anna Pelagotti, Antonio Pifferi, Srinath Rajagopal, Fulvio Ratto, Daniel Razansky, Lisa M. Richards, Avihai Ron, Mithun Kuniyil Ajith Singh, Maximillian Waldner, Kun Wang, Lihong V. Wang, Wenfeng Xia, Bajram Zeqiri
doi:10.1117/12.2506044
Proceedings of Photons Plus Ultrasound: Imaging and Sensing 2019

Estimation of blood oxygenation with learned spectral decoloring for quantitative photoacoustic imaging (LSD-qPAI)
Janek Gröhl, Thomas Kirchner, Tim Adler and Lena Maier-Hein
arxiv:1902.05839
arXiv (2019) follow-up to a Photons Plus Ultrasound: Imaging and Sensing (2019) abstract and poster

An open-source software platform for translational photoacoustic research and its application to motion-corrected blood oxygenation estimation
Thomas Kirchner, Janek Gröhl, Franz Sattler, Moritz S. Bischoff, Angelika Laha, Marco Nolden and Lena Maier-Hein
arxiv:1901.09781
arXiv (2019) follow-up to the Photons Plus Ultrasound: Imaging and Sensing (2018) abstract and talk *Real-time in vivo blood oxygenation measurements with an open-source software platform for translational photoacoustic research*
doi:10.1117/12.2288363

Reconstruction of initial pressure from limited view photoacoustic images using deep learning
Dominik Waibel, Janek Gröhl, Fabian Isensee, Thomas Kirchner, Klaus Maier-Hein, Lena Maier-Hein
doi:10.1117/12.2288353
Proceedings of Photons Plus Ultrasound: Imaging and Sensing (2018)

Confidence estimation for quantitative photoacoustic imaging
Janek Gröhl, Thomas Kirchner and Lena Maier-Hein
doi:10.1117/12.2288362
Proceedings of Photons Plus Ultrasound: Imaging and Sensing (2018)

Real-time delay multiply and sum beamforming for multispectral photoacoustics
Franz Sattler, Thomas Kirchner, Janek Gröhl and Lena Maier-Hein
doi:10.1117/12.2285862
Proceedings of Photons Plus Ultrasound: Imaging and Sensing (2018)

Freehand photoacoustic tomography for 3D angiography using local gradient information
Thomas Kirchner, Esther Wild, Klaus Maier-Hein, Lena Maier-Hein
doi:10.1117/12.2209368
Proceedings of Photons Plus Ultrasound: Imaging and Sensing (2016)

BIBLIOGRAPHY

[1] William R Mower, Carolyn Sachs, Emily L Nicklin, Larry J Baraff, et al. "Pulse oximetry as a fifth pediatric vital sign." In: *Pediatrics* 99.5 (1997), pp. 681–686.

[2] Christopher Nimsky, Oliver Ganslandt, Michael Buchfelder, and Rudolf Fahlbusch. "Intraoperative visualization for resection of gliomas: the role of functional neuronavigation and intraoperative 1.5 T MRI." In: *Neurological research* 28.5 (2006), pp. 482–487.

[3] Nouchine Hadjikhani et al. "Mechanisms of migraine aura revealed by functional MRI in human visual cortex." en. In: *PNAS* 98.8 (Apr. 2001), pp. 4687–4692. ISSN: 0027-8424, 1091-6490. DOI: 10.1073/pnas.071582498.

[4] Daniela Kuhnt, Miriam HA Bauer, Andreas Becker, Dorit Merhof, Amir Zolal, Mirco Richter, Peter Grummich, Oliver Ganslandt, Michael Buchfelder, and Christopher Nimsky. "Intraoperative visualization of fiber tracking based reconstruction of language pathways in glioma surgery." In: *Neurosurgery* 70.4 (2011), pp. 911–920.

[5] S. Umesh Rudrapatna, Arend M. Hamming, Marieke J. H. Wermer, Annette van der Toorn, and Rick M. Dijkhuizen. "Measurement of distinctive features of cortical spreading depolarizations with different MRI contrasts." eng. In: *NMR Biomed* 28.5 (May 2015), pp. 591–600. ISSN: 1099-1492. DOI: 10.1002/nbm.3288.

[6] Xueding Wang, Yongjiang Pang, Geng Ku, Xueyi Xie, George Stoica, and Lihong V Wang. "Noninvasive laser-induced photoacoustic tomography for structural and functional in vivo imaging of the brain." English. In: *Nature Biotechnology* 21.7 (2003), pp. 803–806. ISSN: 1087-0156 ; 1546-1696. DOI: 10.1038/nbt839.

[7] Da-Kang Yao, Konstantin Maslov, Kirk K Shung, Qifa Zhou, and Lihong V Wang. "In vivo label-free photoacoustic microscopy of cell nuclei by excitation of DNA and RNA." In: *Optics letters* 35.24 (2010), pp. 4139–4141.

[8] Antoine Laurent Lavoisier. *Essays Physical and Chemical: By M. Lavoisier,... Translated from the French, with Notes, and an Appendix, by Thomas Henry,...* Joseph Johnson, 1776.

[9] Adrian Taruttis, Gooitzen M van Dam, and Vasilis Ntziachristos. "Mesoscopic and macroscopic optoacoustic imaging of cancer." In: *Cancer research* 75.8 (2015), pp. 1548–1559.

[10]   WD Butt and David Keilin. "Absorption spectra and some other properties of cytochrome c and of its compounds with ligands." In: *Proceedings of the Royal Society of London. Series B. Biological Sciences* 156.965 (1962), pp. 429–458.

[11]   Lihong V Wang and Hsin-i Wu. *Biomedical optics: principles and imaging*. John Wiley & Sons, 2012.

[12]   Steven L. Jacques. "Optical properties of biological tissues: a review." English. In: *Physics in medicine and biology* 58.11 (2013), R37. ISSN: 1361-6560.

[13]   Alexander Graham Bell. "Production of sound by radiant energy." In: *Journal of the Franklin Institute* 111.6 (1881), pp. 401–428. ISSN: 0016-0032. DOI: 10.1016/0016-0032(81)90005-3.

[14]   Ben Cox. *Acoustics for Ultrasound Imaging*. University College London, 2013.

[15]   Ben Cox. *Optics in Medicine: Introduction to Laser-Tissue Interactions*. University College London, 2013.

[16]   Elena Petrova, Sergey Ermilov, Richard Su, Vyacheslav Nadvoretskiy, André Conjusteau, and Alexander Oraevsky. "Using optoacoustic imaging for measuring the temperature dependence of Grüneisen parameter in optically absorbing solutions." In: *Optics express* 21.21 (2013), pp. 25077–25090.

[17]   Inc. American National Standards Institute. *American National Standard for Safe Use of Lasers*. Ed. by Laser Institute of America. Laser Institute of America, 2007.

[18]   Stratis Tzoumas, Antonio Nunes, Ivan Olefir, Stefan Stangl, Panagiotis Symvoulidis, Sarah Glasl, Christine Bayer, Gabriele Multhoff, and Vasilis Ntziachristos. "Eigenspectra optoacoustic tomography achieves quantitative blood oxygenation imaging deep in tissues." In: *Nature communications* 7 (2016), p. 12121.

[19]   Jan Laufer. "Photoacoustic Imaging: Principles and Applications." In: *Quantification of Biophysical Parameters in Medical Imaging*. Springer, 2018, pp. 303–324.

[20]   Bradley E Treeby, Edward Z Zhang, and Benjamin T Cox. "Photoacoustic tomography in absorbing acoustic media using time reversal." In: *Inverse Problems* 26.11 (2010), p. 115003.

[21]   EZ Zhang, JG Laufer, RB Pedley, and PC Beard. "In vivo high-resolution 3D photoacoustic imaging of superficial vascular anatomy." In: *Physics in Medicine & Biology* 54.4 (2009), p. 1035.

[22]   BT Cox and BE Treeby. "Effect of sensor directionality on photoacoustic imaging: a study using the k-wave toolbox." In: *Photons Plus Ultrasound: Imaging and Sensing 2010*. Vol. 7564. International Society for Optics and Photonics. 2010, p. 75640I.

[23] Bin Huang, Jun Xia, Konstantin I Maslov, and Lihong V Wang. "Improving limited-view photoacoustic tomography with an acoustic reflector." In: *Journal of biomedical optics* 18.11 (2013), p. 110505.

[24] Dominik Waibel, Janek Gröhl, Fabian Isensee, Thomas Kirchner, Klaus Maier-Hein, and Lena Maier-Hein. "Reconstruction of initial pressure from limited view photoacoustic images using deep learning." In: *Photons Plus Ultrasound: Imaging and Sensing 2018*. Vol. 10494. International Society for Optics and Photonics. 2018, 104942S.

[25] Claude Elwood Shannon. "A mathematical theory of communication." In: *Bell system technical journal* 27.3 (1948), pp. 379–423.

[26] Robert A Kruger, Pingyu Liu, Yuncai "Richard" Fang, and C Robert Appledorn. "Photoacoustic ultrasound (PAUS) — reconstruction tomography." In: *Medical physics* 22.10 (1995), pp. 1605–1609.

[27] Habib Ammari, Elie Bretin, Vincent Jugnon, and Abdul Wahab. "Photoacoustic imaging for attenuating acoustic media." In: *Mathematical modeling in biomedical imaging II*. Springer, 2012, pp. 57–84.

[28] Benjamin T Cox, Simon R Arridge, Kornel P Köstli, and Paul C Beard. "Two-dimensional quantitative photoacoustic image reconstruction of absorption distributions in scattering media by use of a simple iterative method." In: *Applied Optics* 45.8 (2006), pp. 1866–1875.

[29] Jacques Curie and Pierre Curie. "Développement par compression de l'électricité polaire dans les cristaux hémièdres à faces inclinées." In: *Bulletin de minéralogie* 3.4 (1880), pp. 90–93.

[30] Shaul Katzir. "The discovery of the piezoelectric effect." In: *The Beginnings of Piezoelectricity*. Springer, 2006, pp. 15–64.

[31] Pierre Curie. "Dilatation électrique du quartz." In: *J. Phys. Theor. Appl.* 8.1 (1889), pp. 149–168.

[32] FJ McClung and RW Hellwarth. "Giant optical pulsations from ruby." In: *Journal of Applied Physics* 33.3 (1962), pp. 828–829.

[33] Mohsen Erfanzadeh, Patrick D Kumavor, and Quing Zhu. "Laser scanning laser diode photoacoustic microscopy system." In: *Photoacoustics* 9 (2018), pp. 1–9.

[34] Hongtao Zhong, Tingyang Duan, Hengrong Lan, Meng Zhou, and Fei Gao. "Review of low-cost photoacoustic sensing and imaging based on laser diode and light-emitting diode." In: *Sensors* 18.7 (2018), p. 2264.

[35] Ali Hariri, Jeanne Lemaster, Junxin Wang, AnanthaKrishnan S Jeevarathinam, Daniel L Chao, and Jesse V Jokerst. "The characterization of an economic and portable LED-based photoacoustic imaging system to facilitate molecular imaging." In: *Photoacoustics* 9 (2018), pp. 10–20.

[36] Yunhao Zhu, Guan Xu, Jie Yuan, Janggun Jo, Girish Gandikota, Hakan Demirci, Toshitaka Agano, Naoto Sato, Yusuke Shigeta, and Xueding Wang. "Light emitting diodes based photoacoustic imaging and potential clinical applications." In: *Scientific reports* 8.1 (2018), p. 9885.

[37] Junjie Yao and Lihong V Wang. "Photoacoustic microscopy." In: *Laser & photonics reviews* 7.5 (2013), pp. 758–778.

[38] Joanna Brunker and Paul Beard. "Velocity measurements in whole blood using acoustic resolution photoacoustic Doppler." In: *Biomedical optics express* 7.7 (2016), pp. 2789–2806.

[39] Hao F Zhang, Konstantin Maslov, George Stoica, and Lihong V Wang. "Functional photoacoustic microscopy for high-resolution and noninvasive in vivo imaging." In: *Nature biotechnology* 24.7 (2006), p. 848.

[40] Junjie Yao, Lidai Wang, Joon-Mo Yang, Liang S Gao, Konstantin I Maslov, Lihong V Wang, Chih-Hsien Huang, and Jun Zou. "Wide-field fast-scanning photoacoustic microscopy based on a water-immersible MEMS scanning mirror." In: *Journal of biomedical optics* 17.8 (2012), p. 080505.

[41] Murad Omar, Mathias Schwarz, Dominik Soliman, Panagiotis Symvoulidis, and Vasilis Ntziachristos. "Pushing the optical imaging limits of cancer with multi-frequency-band raster-scan optoacoustic mesoscopy (RSOM)." In: *Neoplasia* 17.2 (2015), pp. 208–214.

[42] Lihong V. Wang and Liang Gao. "Photoacoustic Microscopy and Computed Tomography: From Bench to Bedside." In: *Annual Review of Biomedical Engineering* 16.1 (2014). PMID: 24905877, pp. 155–185. DOI: 10.1146/annurev-bioeng-071813-104553.

[43] Vasilis Ntziachristos and Daniel Razansky. "Molecular imaging by means of multispectral optoacoustic tomography (MSOT)." In: *Chemical reviews* 110.5 (2010), pp. 2783–2794.

[44] Daniel Razansky, Martin Distel, Claudio Vinegoni, Rui Ma, Norbert Perrimon, Reinhard W Köster, and Vasilis Ntziachristos. "Multispectral opto-acoustic tomography of deep-seated fluorescent proteins in vivo." In: *Nature Photonics* 3.7 (2009), p. 412.

[45] Daniel Razansky, Nikolaos C Deliolanis, Claudio Vinegoni, and Vasilis Ntziachristos. "Deep tissue optical and optoacoustic molecular imaging technologies for pre-clinical research and drug discovery." In: *Current pharmaceutical biotechnology* 13.4 (2012), pp. 504–522.

[46] Yonggeng Goh, Ghayathri Balasundaram, Mohesh Moothanchery, Amalina Attia, Xiuting Li, Hann Qian Lim, Neal Burton, Yi Qiu, Thomas Choudary Putti, Ching Wan Chan, et al. "Multi-spectral optoacoustic tomography in assessment of breast tumor margins during breast-conserving surgery: A first-in-human case study." In: *Clinical breast cancer* 18.6 (2018), e1247–e1250.

[47] Robert A Kruger, Cherie M Kuzmiak, Richard B Lam, Daniel R Reinecke, Stephen P Del Rio, and Doreen Steed. "Dedicated 3D photoacoustic breast imaging." In: *Medical physics* 40.11 (2013).

[48] Wenfeng Xia, Ton G Leeuwen van, Wiendelt Steenbergen, Daniele Piras, and Srirang Manohar. "Photoacoustic Imaging of the Breast Using the Twente Photoacoustic Mammoscope: Present Status and Future Perspectives." English. In: *IEEE Journal on Selected topics in Quantum Electronics* 16.4 (2010), pp. 730–739. ISSN: 1077-260X ; 1558-4542. DOI: 10.1109/JSTQE.2009.2034870.

[49] Robert A Kruger, Richard B Lam, Daniel R Reinecke, Stephen P Del Rio, and Ryan P Doyle. "Photoacoustic angiography of the breast." In: *Medical physics* 37.11 (2010), pp. 6096–6100.

[50] Michelle Heijblom, D Piras, M Brinkhuis, Johannes CG van Hespen, FM Van den Engh, M Van der Schaaf, JM Klaase, TG Van Leeuwen, Wiendelt Steenbergen, and Srirang Manohar. "Photoacoustic image patterns of breast carcinoma and comparisons with Magnetic Resonance Imaging and vascular stained histopathology." In: *Scientific reports* 5 (2015), p. 11778.

[51] M. Heijblom, D. Piras, W. Xia, J.C.G. van Hespen, J.M. Klaase, F.M. van den Engh, T.G. van Leeuwen, W. Steenbergen, and S. Manohar. "Visualizing breast cancer using the Twente photoacoustic mammoscope: what do we learn from twelve new patient measurements?" English. In: *Optics express* 20.11 (2012), p. 11582. ISSN: 1094-4087.

[52] Srirang Manohar, Susanne E Vaartjes, Johan C G van Hespen, Joost M Klaase, Frank M van den Engh, Wiendelt Steenbergen, and Ton G van Leeuwen. "Initial results of in vivo non-invasive cancer imaging in the human breast using near-infrared photoacoustics." English. In: *Optics Express* 15.19 (2007), pp. 12277–12285. ISSN: 1094-4087 ; 1094-4087. DOI: 10.1364/OE.15.012277.

[53] Sven Gottschalk, Oleksiy Degtyaruk, Benedict Mc Larney, Johannes Rebling, Magdalena Anastasia Hutter, Xose Luis Dean-Ben, Shy Shoham, and Daniel Razansky. "Rapid volumetric op-

toacoustic imaging of neural dynamics across the mouse brain." In: *Nature Biomedical Engineering* (2019), p. 1.

[54]   Ivana Ivankovic, Elena Mercep, Claus-Georg Schmedt, Xose Luis Dean-Ben, and Daniel Razansky. "Real-time volumetric assessment of the human carotid artery: handheld multispectral optoacoustic tomography." In: *Radiology* 291.1 (2019), pp. 45–50.

[55]   Jeesu Kim, Sara Park, Yuhan Jung, Sunyeob Chang, Jinyong Park, Yumiao Zhang, Jonathan F Lovell, and Chulhong Kim. "Programmable real-time clinical photoacoustic and ultrasound imaging system." In: *Scientific reports* 6 (2016), p. 35137. DOI: 10.1038/srep35137.

[56]   Volker Neuschmelting, Neal C Burton, Hannah Lockau, Alexander Urich, Stefan Harmsen, Vasilis Ntziachristos, and Moritz F Kircher. "Performance of a multispectral optoacoustic tomography (MSOT) system equipped with 2D vs. 3D handheld probes for potential clinical translation." In: *Photoacoustics* 4.1 (2016), pp. 1–10.

[57]   Andreas Buehler, Marcin Kacprowicz, Adrian Taruttis, and Vasilis Ntziachristos. "Real-time handheld multispectral optoacoustic imaging." In: *Optics letters* 38.9 (2013), pp. 1404–1406.

[58]   Lacey R McNally, Megan Mezera, Desiree E Morgan, Peter J Frederick, Eddy S Yang, Isam-Eldin Eltoum, and William E Grizzle. "Current and emerging clinical applications of multispectral optoacoustic tomography (MSOT) in oncology." In: *Clinical cancer research* 22.14 (2016), pp. 3432–3439.

[59]   Reni Butler, Philip T Lavin, F Lee Tucker, Lora D Barke, Marcela Böhm-Vélez, Stamatia Destounis, Stephen R Grobmyer, Janine Katzen, Kenneth A Kist, Erini V Makariou, et al. "Optoacoustic breast imaging: Imaging-pathology correlation of optoacoustic features in benign and malignant breast masses." In: *American Journal of Roentgenology* (2018), pp. 1155–1170.

[60]   Gisela LG Menezes, Ruud M Pijnappel, Carla Meeuwis, Robertus Bisschops, Jeroen Veltman, Philip T Lavin, Marc J van de Vijver, and Ritse M Mann. "Downgrading of breast masses suspicious for cancer by using optoacoustic breast imaging." In: *Radiology* 288.2 (2018), pp. 355–365.

[61]   Gael Diot, Stephan Metz, Aurelia Noske, Evangelos Liapis, Barbara Schroeder, Saak V Ovsepian, Reinhard Meier, Ernst Rummeny, and Vasilis Ntziachristos. "Multispectral optoacoustic tomography (MSOT) of human breast cancer." In: *Clinical Cancer Research* 23.22 (2017), pp. 6912–6922.

[62] Ferdinand Knieling, Clemens Neufert, Arndt Hartmann, Jing Claussen, Alexander Urich, Cornelia Egger, Marcel Vetter, Sarah Fischer, Lukas Pfeifer, Alexander Hagel, et al. "Multispectral optoacoustic tomography for assessment of Crohn's disease activity." In: *New England Journal of Medicine* 376.13 (2017), pp. 1292–1294.

[63] Lihong V Wang and Song Hu. "Photoacoustic tomography: in vivo imaging from organelles to organs." In: *science* 335.6075 (2012), pp. 1458–1462.

[64] Peter Karl Seitz and Rolf Bendl. "Robotergestützte Ultraschall-bildgebung zur Lagekontrolle von Zielgewebe während der Strahlentherapie." In: *Bildverarbeitung für die Medizin*. Springer, 2017, pp. 287–292.

[65] Benjamin T Cox, Jan G Laufer, Paul C Beard, and Simon R Arridge. "Quantitative spectroscopic photoacoustic imaging: a review." In: *Journal of biomedical optics* 17.6 (2012), p. 061202.

[66] FJ Fry and JE Barger. "Acoustical properties of the human skull." In: *The Journal of the Acoustical Society of America* 63.5 (1978), pp. 1576–1590.

[67] Edgar Santos, Fiorella León, Humberto Silos, Renan Sanchez-Porras, C William Shuttleworth, Andreas Unterberg, and Oliver W Sakowitz. "Incidence, hemodynamic, and electrical characteristics of spreading depolarization in a swine model are affected by local but not by intravenous application of magnesium." In: *Journal of Cerebral Blood Flow & Metabolism* 36.12 (2016), pp. 2051–2057.

DECLARATION

Das Folgende versichere ich an Eides statt.

Ich habe nur angegebene Quellen und Hilfsmittel benutzt und mich keiner unzulässigen Hilfe Dritter bedient. Insbesondere habe ich wörtlich oder sinngemäß aus anderen Werken übernommene Inhalte als solche kenntlich gemacht.

Die Arbeit oder Teile davon habe ich bislang nicht an einer Hochschule des In- oder Auslands als Bestandteil einer Prüfungs- oder Qualifikationsleistung vorgelegt.

Die Bedeutung der eidesstattlichen Versicherung und die strafrechtlichen Folgen einer unrichtigen oder unvollständigen eidesstattlichen Versicherung sind mir bekannt.

Ich versichere dass ich nach bestem Wissen und Gewissen die reine Wahrheit erklärt und nichts verschwiegen habe.

Heidelberg, April 2019

Thomas Kirchner